



저작자표시-비영리-변경금지 2.0 대한민국

이용자는 아래의 조건을 따르는 경우에 한하여 자유롭게

- 이 저작물을 복제, 배포, 전송, 전시, 공연 및 방송할 수 있습니다.

다음과 같은 조건을 따라야 합니다:



저작자표시. 귀하는 원저작자를 표시하여야 합니다.



비영리. 귀하는 이 저작물을 영리 목적으로 이용할 수 없습니다.



변경금지. 귀하는 이 저작물을 개작, 변형 또는 가공할 수 없습니다.

- 귀하는, 이 저작물의 재이용이나 배포의 경우, 이 저작물에 적용된 이용허락조건을 명확하게 나타내어야 합니다.
- 저작권자로부터 별도의 허가를 받으면 이러한 조건들은 적용되지 않습니다.

저작권법에 따른 이용자의 권리는 위의 내용에 의하여 영향을 받지 않습니다.

이것은 [이용허락규약\(Legal Code\)](#)을 이해하기 쉽게 요약한 것입니다.

[Disclaimer](#)

공학박사학위논문

펼럭이는 날개와 깃발의 유체역학:  
스케일링 분석과 실험

Hydrodynamics of flapping foils  
and flags: scaling analysis and  
experiments

2016 년 2 월

서울대학교 대학원  
기계항공공학부  
이 정 수

펼럭이는 날개와 깃발의 유체역학:  
스케일링 분석과 실험

Hydrodynamics of flapping foils and flags:  
scaling analysis and experiments

지도교수 김 호 영

이 논문을 공학박사 학위논문으로 제출함

2015 년 4 월

서울대학교 대학원  
기계항공공학부  
이 정 수

이정수의 공학박사 학위논문을 인준함  
2015 년 6 월

위 원 장           최 해 천           (인)  
부 위 원 장           김 호 영           (인)  
위 원           조 규 진           (인)  
위 원           박 형 민           (인)  
위 원           김 원 정           (인)

# Hydrodynamics of flapping foils and flags: scaling analysis and experiments

Jeongsu Lee

Department of Mechanical and Aerospace Engineering  
Seoul National University

A thesis submitted for the degree of

*Doctor of Philosophy*

February 2016

# Abstract

Hydrodynamics of flapping foils and flags: scaling analysis  
and experiments

Jeongsu Lee

Department of Mechanical and Aerospace Engineering

The Graduate School

Seoul National University

In the present research, we conducted the fluid dynamic study of flapping foils for bio locomotion of swimming and flying animals and the fluttering flags adjacent to rigid plate. The scaling laws for the force produced by the flapping foils are constructed by considering the momentum imparted to the vortical structures generated by the foil motion. The novel concept of the wind energy generator is developed using the contact electrification of the fluttering flag and the plate.

We first studied the hydrodynamics of the angularly reciprocating plate without a free stream velocity as an elementary mode of the flapping locomotion. We visualize the flow field around the flat plate to find that two independent vortical structures are formed per half-cycle, resulting in the separation of two distinct vortex pairs at sharp edges. Based on our observations, we derive a scaling law to predict the thrust of the flapping plate

considering the momentum imparted to the vortical structures. The scaling law is in good agreement with the experimental observations.

The study on the angularly reciprocating plate is extended to find a physical explanation for the relatively stubby fins of small aquatic animals. The thrust and flow field around the angularly reciprocating plate is examined varying the tail shapes and aspect ratio over two order of magnitudes. The thrust of a flapping tail can be predicted based on a universal scaling law regardless of the tail shapes, which considers the momentum imparted to the surrounding flows. The thrust in the given tail area and kinematics is maximized at the low aspect ratio of 0.7, whereas the efficiency continuously increases along with the aspect ratio. Combination of the current mathematical modeling and biological observations suggests that small aquatic animals selected a caudal fin with a low aspect ratio for the purpose of added thrust but at the expense of efficiency.

We next construct a scaling law for the lift of hovering insects that elucidates a unified mechanism enabling the insects to be airborne through relatively simple scaling arguments of the strength of the leading edge vortex and the momentum induced by the vortical structure. Comparison of our theory with the measurement data of 33 species of insects confirms that the scaling law captures the essential physics of lift generation of hovering insects. Our results offer a simple yet powerful guideline for biologists who seek the evolutionary direction of the shape and kinematics of insect wings, and for engineers who design flapping-based micro air vehicles.

Next, the dynamics and energy transfer of fluttering motions of flags placed adjacent to a plate are investigated systematically

by varying the inter-space distance, material, and dimensions of the flag, and incoming velocity. The stability condition of the flag adjacent to the plate is almost identical to that in the case of when the flag is not placed adjacent to a plate. However, when flutter occurs, it exhibits asymmetric dynamic behavior with respect to the centreline because of the influence of the plate, even when no contact is made. The energy transfer process is characterized by three distinct stages for each half cycle: energy absorption at the middle of the flag, transition, and energy release at the end part. Flag-plate contact modes, which can be classified as single contact, double contact, contact-propagation, and chaotic contact, are illustrated in their regime plot based on the mass ratio and non-dimensional velocity. Furthermore, the reduced frequency and the Strouhal number of the flag flutter adjacent to the plate are examined by varying the flag length and incoming velocity. Reduced frequency is confined in the narrow range from 0.3 to 0.6, which corresponds to the single flag flutter. The Strouhal number is shown to converge to the optimal value of 0.3 as the incoming velocity increases, implying self-optimization.

Based on the study of the fluttering dynamics of the fluttering flag adjacent to the plate, we developed a novel and powerful wind energy harvesting system, namely, flutter-driven triboelectric generator (FTEG) using the self-sustained oscillation of flags as a mechanical energy, which has the potential use for wireless electronics. The flutter-driven triboelectric generator having dual plate configuration with dimensions of 7.5 cm  $\times$  5 cm under the incident air flow velocity of 15 m/s can produce outstanding power performances such as the instantaneous output voltage and current of 200 V and 60  $\mu$ A, respectively, espe-

cially with the extremely high frequency of 158 Hz. Our novel system can fully charge a 100  $\mu\text{F}$  capacitor within 245 seconds, corresponding to an average power density of approximately 0.86 mW. In addition, the flutter-driven triboelectric generator can be easily scaled up toward large energy generating system by employing the parallel devices in wind-rich place. We expect that the flutter-driven triboelectric generator can not only be an ideal source for the small scale energy harvesting system for wireless electronics, but also it can provide a novel pathway to the electrical energy generation using wind.

Keywords : Flapping locomotion, Vortex flows, Flag flutter,  
Energy harvesting

Student Number : 2009 - 23077

# Contents

<b>Abstract</b>	<b>i</b>
<b>Contents</b>	<b>v</b>
<b>List of Figures</b>	<b>viii</b>
<b>List of Tables</b>	<b>xvii</b>
<b>1 Introduction</b>	<b>1</b>
1.1 Outline . . . . .	1
1.2 Background for the study on the flapping foils . . . . .	2
1.3 Background for the study on the fluttering flags . . . . .	7
<b>2 Wake and thrust of an angularly reciprocating plate</b>	<b>11</b>
2.1 Introduction . . . . .	11
2.2 Experimental apparatus . . . . .	13
2.3 Flow visualisation results . . . . .	14
2.4 Scaling laws . . . . .	19
2.5 Conclusions . . . . .	24
<b>3 Hydrodynamic principles of the evolutionary selection of fish caudal fin shapes</b>	<b>26</b>
3.1 Introduction . . . . .	26
3.2 Experimental apparatus . . . . .	27
3.3 Results . . . . .	30

## CONTENTS

---

3.3.1	Flow measurements . . . . .	30
3.3.2	Scaling laws . . . . .	30
3.3.3	Optimal aspect-ratio . . . . .	34
3.4	Discussion . . . . .	37
<b>4</b>	<b>A scaling law for the lift of hovering insects</b>	<b>41</b>
4.1	Introduction . . . . .	41
4.2	Experimental apparatus . . . . .	43
4.3	Results and discussion . . . . .	44
4.3.1	Estimation of leading edge vortex strength . . . . .	44
4.3.2	A model for lift . . . . .	45
4.3.3	Scaling law based on the conventional steady potential- flow theory . . . . .	49
4.4	Conclusions . . . . .	50
<b>5</b>	<b>Experimental study on the fluttering flag-plate interaction</b>	<b>53</b>
5.1	Introduction . . . . .	53
5.2	Materials and methods . . . . .	55
5.2.1	Experimental apparatus . . . . .	55
5.2.2	Hydrodynamic modelling . . . . .	56
5.2.3	Proper orthogonal decomposition . . . . .	58
5.3	Results and discussion . . . . .	58
5.3.1	Stability condition . . . . .	58
5.3.2	Dynamics and energy transfer process . . . . .	61
5.3.3	Flag-plate contact modes . . . . .	65
5.4	Conclusions . . . . .	70
<b>6</b>	<b>Flutter-driven triboelectrification for harvesting wind en- ergy</b>	<b>71</b>
6.1	Introduction . . . . .	71
6.2	Materials and methods . . . . .	74
6.2.1	Experimental set-up for characterization . . . . .	74

## CONTENTS

---

6.2.2	Fabrication of a FTEG . . . . .	74
6.3	Results . . . . .	76
6.3.1	Flutter-driven Triboelectric generator (FTEG) set-up	76
6.3.2	Analysis of fluttering behavior . . . . .	76
6.3.3	Working principle . . . . .	80
6.3.4	Electrical characterization of FTEG . . . . .	81
6.3.5	Performance of a FTEG as a function of flow velocity	83
6.3.6	Durability and Efficiency . . . . .	85
6.3.7	Application of multiple arrays of FTEGs . . . . .	86
6.3.8	Demonstration in an open environment . . . . .	88
6.4	Discussion . . . . .	89
<b>7</b>	<b>Conclusions</b>	<b>91</b>
<b>A</b>	<b>Comparison of the scaling law with high-<math>St</math> computational results</b>	<b>93</b>
<b>B</b>	<b>Influence of the chordwise vortices on the thrust of an angularly reciprocating plate</b>	<b>96</b>
	<b>References</b>	<b>98</b>
	<b>Abstract (in Korean)</b>	<b>111</b>

# List of Figures

2.1	Experimental apparatus consisting of a flat plate oscillated about the $z$ -axis immersed in a water tank, load cells, a hydrogen bubble generator, a laser and a high-speed camera. The front view of the flat plate shows a blade element in dashed lines, which is used in our modelling. . . . .	14
2.2	Visualisation of flows via hydrogen bubbles around a flat-plate with $[h, w] = [4, 12]$ cm, oscillating at $f = 1.5$ Hz. (a) Acceleration-phase vortex (APV) at $\theta = 10^\circ$ ; (b) emergence of stroke reversal vortex (SRV) at $\theta = 17^\circ$ ; (c) emergence of APV at $\theta = 12^\circ$ ; (d) reattachment of APV at $\theta = 5^\circ$ . The round arrow indicates the instantaneous direction of flat-plate rotation. Scale bar, 20 mm. . . . .	16
2.3	Vorticity contour around a flat-plate with $[h, w] = [4, 12]$ cm, oscillating at $f = 0.2$ Hz. (a) Acceleration-phase vortex (APV) at $\theta = 10^\circ$ ; (b) coexisting APV and SRV during stroke reversal at $\theta = 17^\circ$ ; (c) shedding of two distinct vortex pairs around the top and bottom edges at $\theta = 15.5^\circ$ ; (d) a newly generated APV during acceleration at $\theta = 14^\circ$ . The round arrow indicates the instantaneous direction of flat-plate rotation. . . . .	17
2.4	Experimentally measured thrust generated by a flat plate with $[h, w] = [4, 12]$ cm, oscillating at $f = 1$ Hz versus time. . . . .	18

## LIST OF FIGURES

---

2.5	Measurement results of circulation plotted according to the scaling law, (2.7). The slope of the best-fitting line is 2.6. . . . .	22
2.6	The mean value of period-averaged thrust, $\langle F_t \rangle$ . (a) $\langle F_t \rangle$ versus $f^2$ for different plate geometries. The circles, triangles and squares correspond to the plates of $w = 6, 9$ and $12$ cm, respectively. The empty, half-filled and filled symbols correspond to the plates of $h = 4, 6$ and $8$ cm, respectively; (b) $\langle F_t \rangle$ plotted according to the scaling law (2.8). The straight line is drawn by the least-square method. The slope of the best-fitting line is 4.7. . . . .	23
2.7	Dimensionless mean thrust, $\langle F_t \rangle / \rho h^4 f^2$ , versus $\beta^{1/2} \eta^{3/2}$ for different plate geometries. The circles, triangles and squares correspond to the plates of $w = 6, 9$ and $12$ cm, respectively. The empty, half-filled and filled symbols correspond to the plates of $h = 4, 6$ and $8$ cm, respectively. Regardless of the Reynolds number varying between $2.7 \times 10^3$ and $2.9 \times 10^4$ , the experimental data follow the scaling law (2.9). The slope of the best-fitting line is 3.3. . . . .	24
3.1	Experimental apparatus and measurements of flow fields and thrusts. (a) Schematic diagram of the experimental apparatus. (b, c) Flow fields and vorticity contour around rectangular and trapezoidal flapping tail, respectively, with $[h, w] = [4, 12]$ cm, oscillating at $0.2$ Hz. The round arrow indicates the instantaneous direction of the tail motion. (d, e) Measured thrust of the rectangular and trapezoidal flapping tail, respectively, with $[h, w] = [4, 12]$ cm, oscillating at $0.5$ Hz. . . . .	29

**LIST OF FIGURES**

---

3.2 Comparison of period-averaged thrust using the scaling law. (a, b) Plots of period-averaged thrust versus  $f_2$  and the scaling law in equation (2), respectively, for differing the tail dimensions and shapes. The black, red, and blue colors correspond to the rectangular, trapezoidal, and delta shapes, respectively. The circles, triangles, and squares correspond to plates of  $w = 6, 9,$  and  $12$  cm, respectively. The empty, half-filled, and filled symbols correspond to plates of  $h = 4, 6,$  and  $8$  cm, respectively. (c) Dimensionless thrust,  $T/(\rho h^4 f^2)$ , versus  $\eta^{5/2} \beta^{1/2} / \text{AR}$  for the different tail dimensions and shapes. The circles, triangles, and squares correspond to a delta, trapezoidal, and rectangular shaped tail, respectively. . . . . 33

3.3 Effects of the aspect-ratio on the thrust and efficiency. (a) The scaled thrust,  $\tilde{T}$ , versus the aspect ratio. The circles, triangles, squares, diamonds, down-pointing triangles, and left- and right-pointing triangles correspond to rectangular tails with an area of 30, 36, 24, 96, 54, 72, and 48 cm<sup>2</sup>, respectively. (b) The thrust data before the slenderness limit versus the scaling law based on the added-mass force. (c) The ratio of hydrodynamic cost of endurance and non-dimensional stroke amplitude versus the aspect ratio. . . . . 36

3.4 Distribution of the aspect ratio of highly migratory aquatic animals (red) and non-migratory freshwater fish (blue). . . . . 38

4.1 Experimental apparatus to visualize the flow field. . . . . 43

4.2 (a) Velocity field and vorticity contour around a translating wing with  $\text{Re}=2500, \alpha=45, \Lambda=1.7$  at  $t=T/2$ . (b) Isolated leading edge vortex around the identical wing. (c) Instantaneous circulation of leading edge vortex at  $t=T/2$  versus the scaling parameter  $U_0 \bar{c} \Lambda \sin \alpha / (\Lambda + 2)$ . . . . . 46

## LIST OF FIGURES

---

4.3	(a) Illustration to define morphological and kinematical parameters of hovering insects. Weight of the insect versus (b) frequency, and (c) the scaling parameter $\rho\Phi R^2\bar{c}^2n^2\cos\beta$ . We compare our theory with experimental observations (81 data points) for 33 species of hovering insects (Ellington, 1984c,d; Ennos, 1989; Fry <i>et al.</i> , 2005; Liu & Sun, 2008; Mou <i>et al.</i> , 2011; Walker <i>et al.</i> , 2010; Weis-Fogh, 1973; Willmott & Ellington, 1997a,b). . . . .	48
4.4	Experimental validation of the normalized scaling law (5.6). We compare our theory with experimental observations (32 data points) for six species of hovering insects (Ellington, 1984c,d; Fry <i>et al.</i> , 2005; Liu & Sun, 2008; Mou <i>et al.</i> , 2011; Walker <i>et al.</i> , 2010; Willmott & Ellington, 1997a,b). . . . .	49
4.5	The experimentally measured weight of hovering insects plotted according to the scaling law (5.7) based on the conventional steady potential-flow theory. The symbols are from figure 6.5. . . . .	50
5.1	Schematic diagrams of the experimental setup. . . . .	56

## LIST OF FIGURES

---

5.2	(a) Ratio of flapping amplitude and flag length, $A/L$ versus non-dimensional velocity $U_R$ for the $[L, w] = [7.5, 5]$ cm sized of woven flag. (b) Plot of critical velocity for flag flutter according to the scaling law (5.11). (c) Plot of critical conditions for flag flutter depending on the mass ratio, $\mu$ and the non-dimensional velocity to mass ratio, $U_R/\mu$ : solid line, present scaling law; dashed line, theory of Tang & Païdoussis (2007); dash-dot line, theory of Argentina & Mahadevan (2005); dash-dot-dot line, theory of Yamaguchi <i>et al.</i> (2000b); cross, experimental data of Huang (1995); x-marker, experimental data of Yamaguchi <i>et al.</i> (2000a); asterisk, experimental data of Watanabe <i>et al.</i> (2002). In here, black, red, blue, and magenta triangles correspond to flags made from polyimide with 140 $\mu\text{m}$ thickness, polycarbonate with 130 $\mu\text{m}$ and 100 $\mu\text{m}$ thickness and woven fabric of 80 $\mu\text{m}$ thickness, respectively. . . . .	60
5.3	Sequential images of fluttering motions for $[L, w] = [7.55]$ cm-sized woven flags at a wind velocity of 5.2 m/s. In here, inter-space distances are (a) infinity (b) 2.5 cm (c) 1.5 cm. .	62
5.4	Analysis on dynamics and energy transfer for $[L, w] = [7.5, 5]$ cm sized of woven flag at wind velocity of 4.9 m/s. (a) Sequential images of fluttering motion. (b) First-to-third mode shapes obtained by proper orthogonal decomposition. (c) Energy captured by bending modes. (d-e) Plots of power delivered from the fluid flow to the lengthwise flag element versus the dimensionless length. In here, the inset shows the posture of the flag when corresponding time. . . . .	63

## LIST OF FIGURES

---

5.5	Energy transfer process of flag flutter adjacent to the plate. Here, $[L, w] = [7.55]$ cm, $U = 5.2$ m/s and inter-space distance is 2.5 cm. (a-f) Plots of power delivered from the fluid flow to the lengthwise element versus the dimensionless length. Here, the inset shows the posture of the flag when corresponding time. . . . .	64
5.6	Energy transfer process of flag flutter adjacent to the plate. Here, $[L, w] = [7.55]$ cm, $U = 5.2$ m/s and inter-space distance is 1s.5 cm. (a-f) Plots of power delivered from the fluid flow to the lengthwise element versus the dimensionless length. Here, the inset shows the posture of the flag when corresponding time. . . . .	65
5.7	Sequential images of fluttering motion (a, d, g, j), contact frequency calculated from the FFT analysis (b, e, h, k), energy fraction captured by each bending modes (c, f, i, l). (a-c) $[L, w] = [7.5, 5]$ cm sized woven flag at a wind velocity of 5.2 m/s. (d-f) $[L, w] = [12, 3]$ cm sized woven flag at a wind velocity of 5.2 m/s. (g-i) $[L, w] = [16, 8]$ cm sized woven flag at a wind velocity of 7.3 m/s. (j-l) $[L, w] = [16, 8]$ cm sized woven flag at a wind velocity of 10.8 m/s. . . . .	67
5.8	(a) Regime plot of contact modes (b, c) Reduced frequency and Strouhal number of flag flutter adjacent to the rigid plate as functions of non-dimensional velocity, where rectangles, circles, and triangles correspond to the 7.5, 12, and 16 cm length of flag, respectively. . . . .	68

## LIST OF FIGURES

---

6.1	Experimental set-up and characterization of fluttering behavior. (a) Schematic diagram of a wind tunnel and the structural design of a FTEG including surface characteristics of (i) a highly flexible flag and (ii) a counter plate, and (iii) the fabrication of the counter plate. (b) Fluttering images of a stand-alone configuration of dimensions $7.5 \text{ cm} \times 5 \text{ cm}$ as captured with a high speed camera. (c) The regime map of the dynamic interaction between a flag and a plate.	75
6.2	Sequential images of contact-separation behavior. (a) Single contact mode: fluttering behavior of a flexible structure with dimensions $7.5 \text{ cm} \times 5 \text{ cm}$ . For (b) double contact mode and (c) chaotic modes, fluttering behavior of a flexible structure with dimensions $12 \text{ cm} (L) \times 3 \text{ cm} (W)$ was captured by a high speed camera under a flow velocity of $9.2 \text{ m/s}$ .	79
6.3	Analysis of the electrical signal for each mode. (a-d) Electrical signal of the FTEG under a flow velocity of $7.5 \text{ m/s}$ with dimensions $7.5 \text{ cm} \times 5 \text{ cm}$ . (a) Short circuit current. (b) Open circuit voltage. (c) Peak in the profile of short circuit current. (d) Peak in the open circuit voltage. (e-h) Electrical signal of the FTEG under a flow velocity of $7.5 \text{ m/s}$ with dimensions $12 \text{ cm} \times 3 \text{ cm}$ . (e) Short circuit current. (f) Open circuit voltage. (g) Peak in the short circuit current. (h) Peak in the open circuit voltage.	82

## LIST OF FIGURES

---

6.4	Influence of flow velocity on electrical output. (a-d) Electrical output performance of a FTEG with a single contact configuration. (a) Open circuit voltage, (b) short circuit current, (c) frequency of electrical output for single contact mode, and (d) charging rate for a 10 $\mu$ F capacitor with flow velocities from 7.5 m/s to 22 m/s. (e-h) Electrical output performance of the FTEG with a double contact configuration. (e) Open circuit voltage, (f) short circuit current, (g) frequency of electrical output for double contact mode, and (h) charging rate for a 10 $\mu$ F capacitor with for flow velocities from 7.5 m/s to 22 m/s. . . . .	84
6.5	Electrical output performance of the dual plate configuration for a FTEG with dimensions 7.5 cm $\times$ 5 cm at a flow velocity of 15 m/s and charging performance for different configurations. (a) Short circuit current for a dual plate configuration. (b) Open circuit voltage of a dual plate configuration. (c) Charging time of a 100 $\mu$ F capacitor to 10 V with a single plate, a dual plate, and a parallel connection between two dual units. (d) The charging rate increasing with the number of units connected side-by-side and in 2 by 2 arrays.	87
6.6	The demonstrations for an open environment. Electrical output performance of the rotatable FTEG. (a) Open circuit voltage. (b) Short circuit current. (c) Charging time of a 10 $\mu$ F capacitor to 0.5 V by charging with the rotatable FTEG (inset: image of the rotatable FTEG). (d) Schematic of the FTEG packaging module. (e) Comparison of the charging time between charging in the open environment and wind tunnel system. . . . .	88

## LIST OF FIGURES

---

A.1	(a) Computational results of Dong et al. (2006) plotted according to the scaling law (2.9). The squares, circles, upright triangles and upside-down triangles correspond to $St = 0.6$ , 0.8, 1.0 and 1.2, respectively. (b) The slope of best-fitting straight lines of (a) as a function of $St$ . . . . .	94
B.1	Schematic illustrations of the vortical structure of (a) lift-based locomotion (b) drag-based locomotion . . . . .	97

# List of Tables

A.1	Raw data of Dong <i>et al.</i> (2006) and their converted values. Here $St = 2Af/U$ and $AR$ is the aspect ratio. . . . .	95
-----	--	----

# Chapter 1

## Introduction

### 1.1 Outline

The present research is largely decomposed into two parts. The first part is the study on the fluid dynamics of the flapping foils for bio locomotion. The results of the first part are described in the following chapters 2-4. The second part is the study on the fluttering flags adjacent to the rigid plate for wind energy harvesting. The results of the second part are described in the following chapters 5-6. The conclusions are followed in the chapter 7.

The main interest of the first part is to provide the simple scaling law to predict the force produced by the flapping foils. In chapter 2, we first examined the fluid dynamics of an angularly reciprocating plate as an elementary model of the flapping locomotion. The results of the chapter 2 are extended to reveal the hydrodynamic principle for the caudal fin shape of small aquatic animals in the following chapter 3. In chapter 3, the fluid dynamics of an angularly reciprocating plate is investigated by varying the shape and the aspect-ratio of the flapping plate and the results are interpreted in comparison with biological data. In chapter 4, the simple scaling law for the lift of hovering insects is developed and validated with the previously reported experimental observations of hovering insects. The

## 1.2 Background for the study on the flapping foils

---

theoretical background and the motivation of the first part is described in the following subchapter 1.2.

The main interest of the second part is to examine the dynamics and energy transfer process of the flag fluttering adjacent to the plate and to develop the novel wind energy harvesting mechanism using the flag-plate interaction. In chapter 5, the fluid dynamics of the flag fluttering adjacent to the rigid plate is examined systematically by varying the flag materials, dimensions, flag-plate distances and incoming velocity. In chapter 6, the novel wind energy harvesting mechanism is developed using the contact between the flag and the plate driven by the flutter of the flag in incoming wind flow. The triboelectric mechanism is employed to convert the mechanical energy of the fluttering flag into the electric energy. The background and the motivation of the second part is described in the following subsection 1.3.

## 1.2 Background for the study on the flapping foils

Flapping is one of the most essential force production mechanisms of animal locomotion, especially for flying and swimming animals. The flapping locomotion can be easily found in our daily life, for example, the wing flaps of hovering insects and free-flying birds and the caudal fin oscillation of aquatic animals. Fluid dynamics of flapping locomotion has been extensively studied thus far by a great number of scientists from diverse fields: physicists, biologists and robot engineers who aim to discover the fundamental physics underlying the force production (Birch & Dickinson, 2003; Dickinson *et al.*, 1999; Ellington *et al.*, 1996; Gazzola *et al.*, 2014), the evolutionary principle of flapping locomotion (Motani, 2002; Taylor *et al.*, 2003) and design rules for bio-mimetic robots (Boyer *et al.*, 2008; Park *et al.*, 2012), respectively. Recent progress in computational and experimental equipment and techniques has greatly elaborated understanding on the flow structures and resulting hydrodynamic forces of flapping

## 1.2 Background for the study on the flapping foils

---

foils. Three-dimensional flow structures around the flying insects (Srygley & Thomas, 2002) and birds (Videler *et al.*, 2004) and swimming fish (Drucker & Lauder, 1999) are discovered based on the smoke visualization or DPIV techniques including the flow fields around the dynamically scaled flapping wings (Jardin *et al.*, 2009; Kim & Gharib, 2011; Poelma *et al.*, 2006; van den Berg & Ellington, 1997). Computational simulations are shown to successfully capture the fluid dynamic forces and flow fields of the flapping foil (Bos *et al.*, 2008; Kweon & Choi, 2010; Liu & Aono, 2009).

Theoretical approaches for the flapping locomotion have been developed on the basis of the conventional steady aerodynamics. In the conventional steady aerodynamics, the wing is reconstructed by the infinitesimal vortex sheet based on the potential flow assumption, and the strength of the vortex sheet is determined by the kinematic boundary condition and smooth flow-off requirement at the trailing edge. The pressure difference induced by the vortex sheet is calculated from the linearized Bernoulli equation under the small disturbance assumption (Newman, 1977; Wu *et al.*, 2006), which results in the aerodynamic lift is expressed by the product of the fluid density, incoming velocity and the circulation bound to the wing corresponding to the Kutta-Joukowski theorem (Newman, 1977). The quasi-steady approximation based on the conventional aerodynamics is intensively tested for hovering insect by Ellington (1984b). It is turned out that the steady aerodynamics is inappropriate to explain the unusual large lift during unsteady motion.

The conventional steady aerodynamics is extended to explain the unsteady dynamics of wing flutter (Newman, 1977; Theodorsen, 1935) taking into account the change in the strength of the bound vortex sheet and the vortex sheet separation at the trailing edge. Unsteady Kutta condition is adopted to determine the strength of the bound vortex sheet, where the pressure difference at the trailing edge is suppressed by the counter balance of the effects of the acceleration and the bound circulation (Newman, 1977;

## 1.2 Background for the study on the flapping foils

---

Theodorsen, 1935; Wu *et al.*, 2006). The unsteady aerodynamics is adopted to explain the caudal fin oscillation of the large cruising fish (Chopra, 1976; Chopra & Kambe, 1977; Lighthill, 1970), which reveals that the stereotypical lunate tail of large cruising fish provides an advantage in efficiency. The unsteady aerodynamic theory is further elaborated considering the spiral motion of the separated vortex sheet induced by the mutual interaction, and it is applied to interpret the paradigmatic wing kinematics such as linear acceleration, reciprocation and wing rotation (Jones, 2003). In addition, non-linear unsteady aerodynamic model is developed to interpret the insect-like flapping wings in hover, and it shows considerable agreement with the dynamically scaled robot wing experiments (Ansari *et al.*, 2006a,b).

Despite enormous studies on the flapping locomotion, the unified theory for the force production, which enables a simple estimation for the produced force with morphological and kinematic parameters of flapping foils, is still unavailable so far. This is mainly because the separating flows and unsteady characteristics make the conventional theory invalid for flapping locomotion. The additional numerical schemes demanding large computational resources and time should be accompanied to analyze the unsteady flapping locomotion in current analytical approaches. The main interest of the first part of the study is to provide the simple scaling laws describing the force production of the flapping foils and to elucidate an essential physical picture underpinning the flapping locomotion. The theoretical approaches developed in this study is summarized in the following.

The force produced by the flapping foils is calculated based on the Kutta-Joukowski theorem in the conventional aerodynamics. However, it is far from valid for flapping locomotion, which flaps in a cyclic manner only after several chord lengths of travel. The separated vorticity of the leading and trailing edges remains in the vicinity of the foils during most of stroke cycle. Instead of Kutta-Joukowski theorem, we need to consider

## 1.2 Background for the study on the flapping foils

---

the momentum of the flow fields induced by the vortical structures around the foils directly so as to model the produced force. It can be shown that, by derivative moment transformation, the momentum of a fluid volume can be written (Wu *et al.*, 2006)

$$\rho \int_V \bar{u} dV = -\frac{1}{2}\rho \int_S \bar{x} \times (\bar{n} \times \bar{u}) dS + \frac{1}{2}\rho \int_V \bar{x} \times \bar{\omega} dV \quad (1.1)$$

where  $\bar{u}$ ,  $\bar{x}$ ,  $\bar{n}$  and  $\bar{\omega}$  are velocity, position, unit outward normal vectors and vorticity, respectively, and S and V denote the bounding surface and volume of the flow field, respectively. Since the diffusive length scale is much smaller than the convective length scale for high Reynolds numbers of flapping locomotion, the attached boundary layer on the wing surface can be approximated as a vortex sheet while the separated vorticities are convected with the flows with negligible diffusion. Modeling the flapping foil as a thin plate, the first term in the right-hand side (RHS) of equation (1.1) corresponds to the vector moment of the tangential velocity discontinuity across the wing surface:  $\int_{S_u} \bar{x} \times (\bar{n} \times [[\bar{u}]]) dS$ , where  $[[\bar{u}]] = \bar{u}_u - \bar{u}_l$  with subscripts  $u$  and  $l$  denoting the upper and lower surface values, respectively. Thus, the time derivative of the first term in the RHS of equation (1.1) can be written as

$$\rho \frac{d}{dt} \int_{S_u} \bar{x} \times (\bar{n} \times [[\bar{u}]]) dS = \rho \frac{d}{dt} \int_{S_u} \bar{x} \times \bar{\gamma} dS \quad (1.2)$$

where  $\bar{\gamma}$  is the strength of the vortex sheet causing velocity discontinuity across the wing surface. The time derivative of the second term in the RHS of equation (1.1) gives

$$\begin{aligned} \rho \frac{d}{dt} \left( \int_V \bar{x} \times \bar{\omega} dV \right) &= \rho \int_V \frac{d\bar{x}}{dt} \times \bar{\omega} dV + \rho \int_V \bar{x} \times \frac{d\bar{\omega}}{dt} dV \\ &= \rho \int_V \bar{u} \times \bar{\omega} dV + \rho \int_V \bar{x} \times (\bar{\omega} \cdot \nabla) \bar{u} dV. \end{aligned} \quad (1.3)$$

Here we assumed  $d\bar{\omega}/dt = (\bar{\omega} \cdot \nabla)\bar{u}$ , that is, the time derivative of vorticity corresponds to the rate of deformation of vortex lines, because viscous

## 1.2 Background for the study on the flapping foils

---

diffusion is negligible compared to the convection for the entire flow field except for the vortex sheet.

Assuming that the vorticity generation on the flapping foils as a vortex loop around the foil on the basis of the observation that the separating flow around the flapping foil is confined around the foil edges, the equation (1.2) can be written as (Wu *et al.*, 2006)

$$\rho \frac{d}{dt} \int_{S_u} \bar{x} \times \bar{\gamma} dS \sim \rho \frac{d\Gamma}{dt} A \quad (1.4)$$

where  $\Gamma$  is the effective circulation of the vortex loop and  $A$  is the area of the foil. The equation (1.4) is the time derivative of the momentum induced by the vortex loop, which corresponds to the momentum departed to the flow field by the generation of the vortical structure. Meanwhile, when the foil is advancing steadily with a velocity,  $U$ , after a considerable time of the departure, the first term in the RHS of equation (1.3) can be written as

$$\rho \int_V \bar{u} \times \bar{\omega} dV \sim \rho U R \Gamma \quad (1.5)$$

where  $R$  is the span of the foil and the evolution of the vortical structure is approximated as the vortex loop consists of the bound vortex on the foil, trailing vortices separated at the foil tip and freely convecting starting vortex. Then, the first term in the RHS of equation (1.3) corresponds to the steady lift of conventional aerodynamics. The last term in the RHS of equation (1.3) is small compared to the terms in the equation (1.4) and (1.5), because it originates from the distortion of the vortex line which is very small compared to the convective expansion of the vortex line in flapping locomotion. Actually, the force produced by the wing-wake interaction, which corresponds to the distortion of the vortex line of the previously separated vortical structure due to the flapping wing, is shown to be very small compared to the force produced by the leading edge vortex (Birch & Dickinson, 2003; Dickinson *et al.*, 1999) for hovering insects. Furthermore, the development of the steady lift is suppressed for the first several chords

### 1.3 Background for the study on the fluttering flags

---

of travel (Newman, 1977) which is the most critical range of flapping locomotion. The vortical structures separated from the trailing edge remains vicinity during the entire stroke in the flapping locomotion, implying the suppression of the steady lift in the flapping locomotion. We then approximated the force production by the momentum transfer to the flow field in flapping locomotion using the equation (1.4) in the derivation of the scaling laws in following chapters 2-4.

### 1.3 Background for the study on the fluttering flags

The fluid induced flutter of a flag is a canonical problem of fluid-structure interaction, and it has been extensively studied thus far by both experimental and analytical approaches. The critical condition for the flag flutter is one of the major issues in the study of the flag flutter. A several of experiments reported that the flag in fluid flow has bi-stable nature in a certain range of flow velocity around the critical condition (Bae *et al.*, 2014; Eloy *et al.*, 2008, 2012; Huang, 1995; Shelley *et al.*, 2005; Taneda, 1968; Virost *et al.*, 2013; Watanabe *et al.*, 2002; Yamaguchi *et al.*, 2000a; Zhang *et al.*, 2000). In a bi-stable range, a small external excitation can make the transition from the stable state to the fluttering state, or vice versa. The considerable bi-stable range is clearly observed for the flags with relatively high aspect ratios, whereas for the flags with the aspect ratio much smaller than unity such as long ribbon in hanging condition the bi-stable range is shown to be disappeared (Eloy *et al.*, 2008, 2012). Numerical simulations based on non-linear hydrodynamic equations also predicted the bi-stable behavior of the fluttering flag, although the bi-stable ranges predicted by the numerical simulations are much smaller than that observed in experiments (Alben & Shelley, 2008; Connell & Yue, 2007; Michelin *et al.*, 2008; Zhu & Peskin, 2002). However, the simulation based on the linearized hydro-

### 1.3 Background for the study on the fluttering flags

---

dynamic equations cannot capture the bi-stable behavior of the flag flutter (Tang *et al.*, 2003; Tang & Païdoussis, 2007), implying that the bi-stability originates from the non-linear effects in fluid dynamics.

Another major issue in the study of the flag flutter is to examine the dynamics of the fluttering flag. The characteristics in dynamic behavior of the fluttering flag are governed by two non-dimensional parameters (Alben & Shelley, 2008; Argentina & Mahadevan, 2005; Tang & Païdoussis, 2007), the mass ratio,  $\mu = \rho L / \rho_p h$ , and the non-dimensional velocity,  $U_R = UL(\rho_p h / D)^{1/2}$ , which describe the relative mass of the flag materials to the interacting fluid and the ratio of the bending wave velocity along the flag and the fluid velocity, respectively. Here,  $\rho$  is the fluid density,  $L$  and  $h$  are the length and thickness of the flag, and  $D$  is the flexural rigidity of the flag. The dynamic states of the flag in fluid flow are characterized as stable-state, periodic flutter and the chaotic flutter, the transition of which occurs subsequently by increasing the incoming velocity (Alben & Shelley, 2008; Connell & Yue, 2007; Tang & Païdoussis, 2007; Zhang *et al.*, 2000). In addition, the deformed shapes of the fluttering flag changed by varying the mass-ratio, and it can be classified as node-less, one-node, imperfect-node and multiple nodes of flutter (Taneda, 1968; Tang & Jiang, 2009; Virost *et al.*, 2013). The deformed shapes of the fluttering flag are determined by what bending modes are excited by the interaction characteristics of the flag and the fluid.

In theoretical approaches, the flow field around the fluttering flag is analyzed based on the unsteady aerodynamic theory or slender body theory. The former model is adopted for the high aspect ratio flags (Tang *et al.*, 2003; Tang & Païdoussis, 2007), in which the hydrodynamic force can be decomposed into the steady lift, lift produced by the vorticity generation and the interaction with the flag and the previously existing wake structure as shown in 1.2. The latter model is employed for the small aspect ratio flags (Eloy *et al.*, 2008; Michelin & Doaré, 2013), in which the hydrody-

### 1.3 Background for the study on the fluttering flags

---

dynamic force is decomposed into the reactive and resistive components. The reactive force is determined by the added mass of the flag elements, while the resistive force is approximated with the drag coefficient of the plate. In present research, the flow field around the fluttering flag is modeled based on the vortex lattice method based on the unsteady aerodynamics, and the mathematical details of model used in this study is described in the chapter 5.

Meanwhile, the fluid induced flutter of a flag has been suggested as an novel mechanism for harvesting wind energy owing to its self-sustainable nature and absolute abundance. One representative example is a piezo-electric flag placed behind the bluff body to exploit the kinetic energy of the periodic wake separated from the body (Akaydin *et al.*, 2010; Allen & Smits, 2001). The another mechanism based on the electromagnetic effect is developed by Tang & Jiang (2009), where the conductive flag is placed between the parallel magnetic panels, and then, the motion of the flag induces the oscillating currents as a response to the variation of the magnetic flux pass through the flag. Furthermore, several of configurations are proposed to improve the energy conversion efficiency of the flutter based wind energy harvester. The inverted configuration of the flag is reported to provides the improved energy conversion of fluid kinetic energy to elastic strain energy of the flag over wide range of the wind velocity (Kim *et al.*, 2013). The flag installed with the destabilizing massive cylinder at the flag edge is shown to provide overwhelming performance than the flag without the destabilizer, especially at the resonance condition the efficiency was improved nearly a two order of magnitudes (Akaydin *et al.*, 2012).

In the present research, we develop the novel concept of the flutter based wind energy harvester which exploits the contact of the flag and the plate driven by the fluttering motion. For this purpose, the flag is placed adjacent to the rigid plate to induce the contact. The materials having different electron affinity is used to fabricate the flag and the plate surface, and

### **1.3 Background for the study on the fluttering flags**

---

then, the instantaneous voltage difference is induced by the triboelectric effect whenever contact occurs. We first studied the dynamics and the energy transfer of the flag adjacent to the rigid plate in the following chapter 5, where the stability condition, contact modes and flag-plate interaction characteristics are examined systematically by varying the wind velocity, inter-space distance, flag materials and dimensions. Based on these fluid dynamic study on the flag-plate interaction, the electric performance of the flutter driven triboelectric generator (FTEG) is studied and the application of the FTEG in real environment is suggested in the following chapter 6.

## Chapter 2

# Wake and thrust of an angularly reciprocating plate

### 2.1 Introduction

Flapping is an essential mechanism for swimming and flying animals to produce lift and thrust. Thus, the force generation mechanisms of various animals employing flapping, such as flying birds (Videler *et al.*, 2004; Wu, 2006, 2007), swimming fish (Chopra, 1976; Drucker & Lauder, 1999; Lighthill, 1970) and hovering insects (Dickinson *et al.*, 1999; Ellington *et al.*, 1996) have been intensely studied. An understanding of flapping also benefits the development of biorobots inspired by animal movement, such as flapping-based micro air vehicles (Zdunich *et al.*, 2007) and robot fish (Yu *et al.*, 2009). In general, such studies have focused on the cases where the animal is moving forward or the locomotive appendages translate linearly during flapping; the existence of a freestream plays an important role in these scenarios. The dynamics of vortices attached or bound to advancing foils are crucial in understanding the force generation mechanism of lift-based propulsion systems, and thus a number of experimental (Birch & Dickinson, 2003; Buchholz & Smitz, 2006, 2008; Jardin *et al.*, 2009; Poelma *et al.*, 2006) and computational (Dong *et al.*, 2006; Jones, 2003; Taira &

Colonius, 2009) studies have addressed the structure and temporal evolution of the vortices generated by flapping foils. However, the foregoing studies do not examine flapping foils without forward propulsion properties and virtually non-existent freestreams. This situation corresponds to the bollard pull condition of flapping (Newman, 1977), which has been rarely considered, unlike its propeller-type propulsion counterpart (Kim & Chung, 2006). Therefore, we seek to complement the existing knowledge of the flapping mechanism by studying angularly reciprocating flat plates in the absence of a freestream.

Investigations of flapping foils with virtually no freestream can also benefit the understanding of some biological movements such as the starting tail-fin motion of fish (Ahlborn *et al.*, 1997), the drag-based propulsion of ducks (Kim & Gharib, 2011) and the standing acrobatics of dolphins (Lang, 1966). The flow field around a submerged plate that rotates from rest about a fixed axis has been visualised in previous studies (Ahlborn *et al.*, 1997; DeVoria & Ringuette, 2012; Kim & Gharib, 2011). However, the thrust generation mechanism of angular reciprocation of a fully immersed flat plate has not been treated thus far. The conventional theories for advancing foils cannot be directly applied to this case because flow separation behind the reciprocating plate is much more significant. In the following, we first describe an experimental apparatus that realizes the angular reciprocation of a rectangular flat plate and measures the thrust. We then present flow visualisation results that unveil a hitherto unknown vortical structure that leads to a novel thrust generation mechanism. On the basis of our observations, we derive a scaling law to predict the thrust of the angularly reciprocating flat plate as a function of the plate dimensions, stroke amplitude and frequency.

## 2.2 Experimental apparatus

Figure 2.1 shows an apparatus that visualises the fluid flow and measures the resultant thrust simultaneously. A rectangular, rigid acrylic flat plate of 3 mm thickness is attached to a metallic rod of length  $l = 12$  cm, which oscillates only about the  $z$ -axis. This single degree of freedom motion is driven by a DC motor and a scotch-yoke mechanism. The stroke angle of the sinusoidal rotation  $2\theta_m$  is fixed to  $35^\circ$ , and the frequency  $f$  ranges from 0.1 to 2.5 Hz. The width of the plate,  $w$ , was varied as 6, 8 and 12 cm, and its height,  $h$ , was varied as 4, 6 and 8 cm. The flat plate and rod assembly is immersed in a transparent water tank measuring 75, 55 and 33 cm in the  $x$ -,  $y$ - and  $z$ -directions, respectively, so that the free surface is 10 cm above the top of the flat plate. The Reynolds number,  $Re = Uh/\nu$ , defined based on the period-averaged, 0.7 radius length speed (Techet, 2008),  $U = 4(0.7R)\theta_m f$ , ranges from  $2.7 \times 10^3$  to  $2.9 \times 10^4$ . Here  $R$  is the radius of rotation of the plate tip,  $R = h + l$ , and  $\nu$  is the kinematic viscosity of water. The normalized stroke amplitude  $\beta = 2R\theta_m/h$  ranges from 1.5 to 4.6 and the aspect ratio  $\eta = w/h$  ranges from 0.75 to 6.0. Platinum wires of 50  $\mu\text{m}$  diameter are attached to the plate and connected to a power supply setup (Kenex HV-401) to generate hydrogen bubbles by the electrolysis of water. The central plane perpendicular to the plate is illuminated to visualise the bubbles with a 2 W continuous laser of 532 nm wavelength through a slit.

We employ two different techniques to visualise the flow using bubbles. First, by imaging bubbles with a high-speed camera (Photron APX-RS) at 60 frames per second (fps), the pathlines of the bubbles during the exposure time of 1/60 s are obtained. Second, the velocity field and vorticity contours are obtained by two-dimensional digital particle image velocimetry (DPIV). We use images of bubbles consisting of  $600 \times 673$  pixels, captured at 125 fps. The movie is analysed by a DPIV software to generate a velocity field with  $32 \times 32$  interrogation size and 50% overlap. Derived velocity vectors are validated by dynamic mean value operator. Error vectors are interpolated

## 2.3 Flow visualisation results

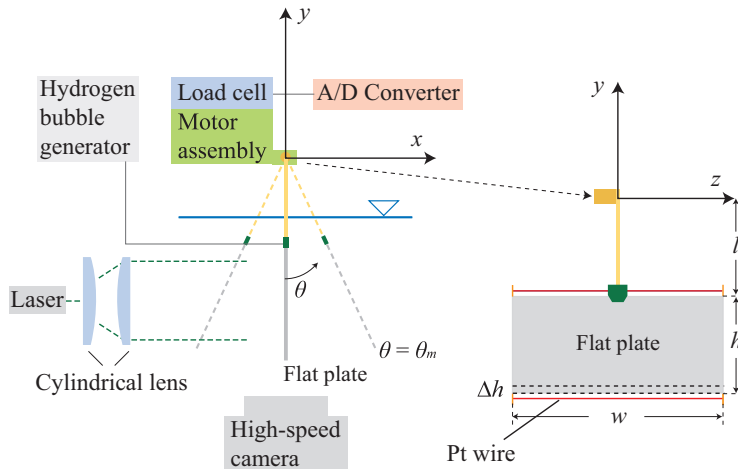


Figure 2.1: Experimental apparatus consisting of a flat plate oscillated about the  $z$ -axis immersed in a water tank, load cells, a hydrogen bubble generator, a laser and a high-speed camera. The front view of the flat plate shows a blade element in dashed lines, which is used in our modelling.

using a kriging interpolation. The number of error vectors is within 2% of the total number of velocity vectors.

The thrust in the  $y$ -direction is measured by two force transducers (Ktoyo 333FB) at 2 kHz. The period-averaged thrust is obtained by averaging the sum of the measurement data of the force transducers over 10 periods of plate oscillation. We repeat the experiments three times and take the mean value of the period-averaged thrust results. All of the experiments were conducted after making sure that the oscillatory movement of the free surface had stopped to minimize the influence of the residual flow from previous experiments.

## 2.3 Flow visualisation results

Figures 2.2 and 2.3 show the pathlines and vorticity contours, respectively, which visualise the fluid flows around the flat plate. While the

## 2.3 Flow visualisation results

---

pathlines of the bubbles visualise the newly generated vortices directly, the vorticity contours show the vortical structures shed away from the plate. These figures indicate that two distinct vortical structures arise per half cycle, hereafter termed as an acceleration-phase vortex (APV) and a stroke-reversal vortex (SRV). Figures 2.2(a) and 2.3(a) show the first vortical structure on the back face of the plate rotating counterclockwise toward the maximum stroke angle,  $\theta_m$ . This vortex results from the plate acceleration occurring since the previous maximum stroke angle,  $-\theta_m$ , and thus is termed the APV. At  $\theta_m$ , the second vortex rotating in the opposite sense to the existing APV is generated on the other side of the plate, as shown in figures 2.2(b) and 2.3(b), corresponding to the SRV. At this moment, the APV and SRV coexist on the top and bottom edges of the plate, as clearly seen in figures 2.3(b-c). As the plate re-accelerates, figures 2.2(c) and 2.3(c-d), the APV and SRV are shed from the plate, forming vortex pairs. Figure 2.3 shows that the vortex pairs are shed at both the top and bottom edges. Also, another vortical structure emerges with the same rotational direction as the previous SRV: the APV of the clockwise half-cycle of plate oscillation (denoted as APV2 in figures 2.2 and 2.3). This vortex structure reattaches to the plate while the foregoing vortex pairs keep drifting away following self-induced currents, figure 2.2(d). Then, the flow pattern symmetrical to that of figure 2.3(b) is repeated at  $-\theta_m$ .

The observed flow characteristics are in stark contrast to those of the starting-stopping vortex in conventional aerodynamics (Dickinson, 1996; Newman, 1977). In the starting-stopping vortex paradigm, the starting vortex develops as the wing translation begins whereas the vorticity of equal strength but opposite sense is distributed along the wing surface. The resulting lift increases monotonically to the steady-state value from precisely half of the steady-state value (Newman, 1977), which is referred to as the Wagner effect. The distributed vorticity separates as a stopping vortex at the end of the stroke, causing the loss of lift. The flow struc-

## 2.3 Flow visualisation results

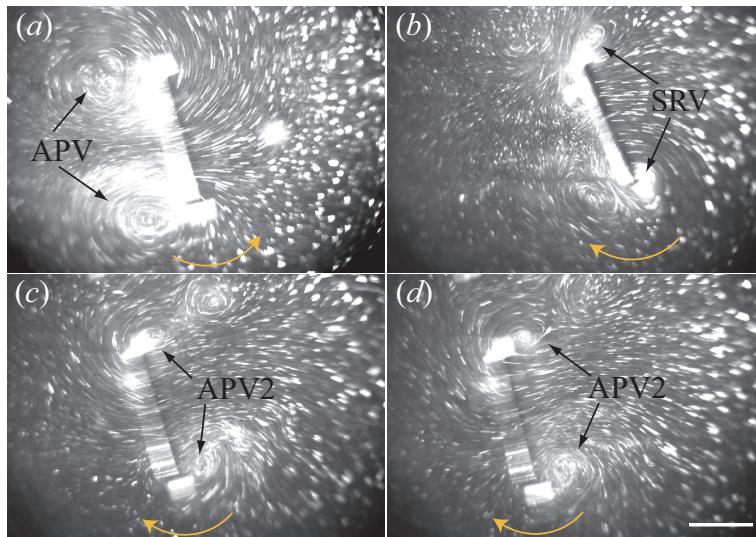


Figure 2.2: Visualisation of flows via hydrogen bubbles around a flat-plate with  $[h, w] = [4, 12]$  cm, oscillating at  $f = 1.5$  Hz. (a) Acceleration-phase vortex (APV) at  $\theta = 10^\circ$ ; (b) emergence of stroke reversal vortex (SRV) at  $\theta = 17^\circ$ ; (c) emergence of APV at  $\theta = 12^\circ$ ; (d) reattachment of APV at  $\theta = 5^\circ$ . The round arrow indicates the instantaneous direction of flat-plate rotation. Scale bar, 20 mm.

ture around flapping foils in natural situations can be explained by using the starting-stopping vortex paradigm (Birch & Dickinson, 2003; Buchholz & Smitz, 2006, 2008; Dong *et al.*, 2006; Drucker & Lauder, 1999; Poelma *et al.*, 2006). We emphasise that while these starting and stopping vortices stem from a single vortex loop (Dickinson, 1996), the angular reciprocation without a freestream forms two distinct vortical structures. As will be discussed below, the two force peaks occurring per half cycle, shown in figure 2.4, are then naturally correlated with the formation of the two vortical structures, APV and SRV.

This marked change in vortex dynamics is mainly due to the difference in the angle of incidence of the fluid flow relative to the foil or plate motion. When a foil either moves forward or translates linearly between stroke re-

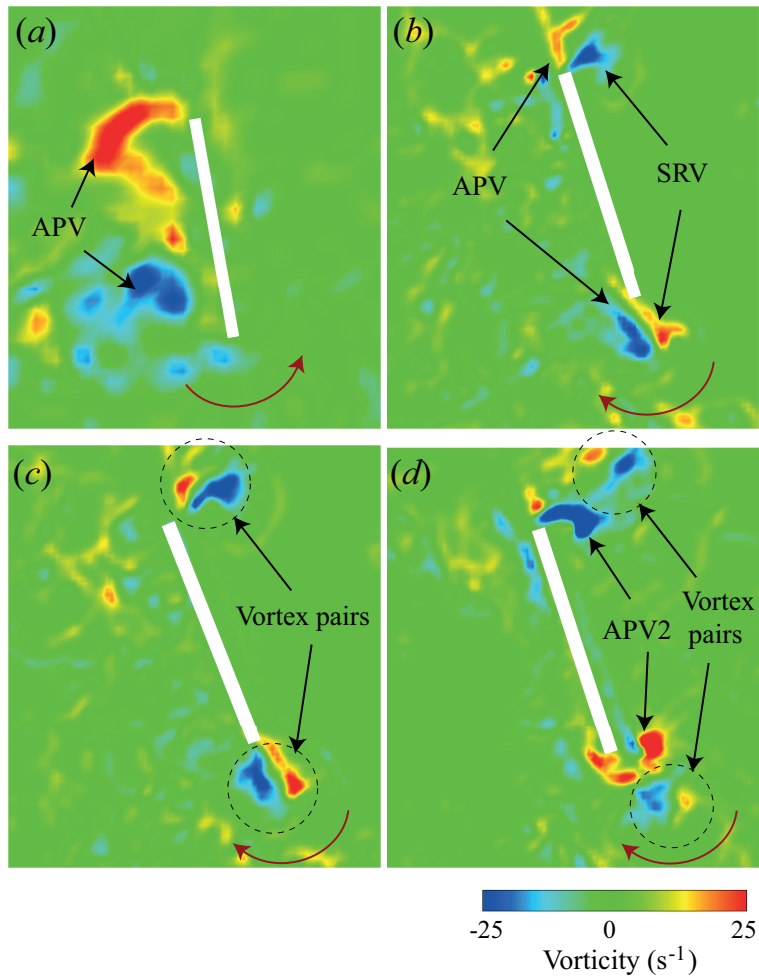


Figure 2.3: Vorticity contour around a flat-plate with  $[h, w] = [4, 12]$  cm, oscillating at  $f = 0.2$  Hz. (a) Acceleration-phase vortex (APV) at  $\theta = 10^\circ$ ; (b) coexisting APV and SRV during stroke reversal at  $\theta = 17^\circ$ ; (c) shedding of two distinct vortex pairs around the top and bottom edges at  $\theta = 15.5^\circ$ ; (d) a newly generated APV during acceleration at  $\theta = 14^\circ$ . The round arrow indicates the instantaneous direction of flat-plate rotation.

## 2.3 Flow visualisation results

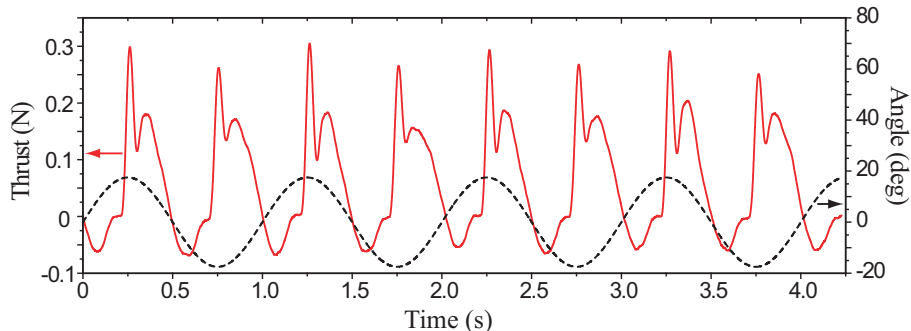


Figure 2.4: Experimentally measured thrust generated by a flat plate with  $[h, w] = [4, 12]$  cm, oscillating at  $f = 1$  Hz versus time.

versals, the incident flow angle during flapping can be significantly reduced due to effective freestream velocities. However, the angularly reciprocating plate without a freestream faces the induced flow at an extremely high incident angle, near  $90^\circ$ . When the reciprocating plate reverses its direction, the flow following the plate cannot adjust itself smoothly to go around the plate. Instead, the flow separates at sharp edges due to the high incident angle, resulting in SRV. Previously reported flow fields around flapping foils with high angles of incidence are consistent with our observation. For the linearly reciprocating foils corresponding to the angular reciprocation with an infinite radius, the shedding of vortex pairs at the top and bottom edges of a plate was clearly identified by the numerical computation of Jones (2003). Through experimental investigation of wake dynamics of a flapping foil imitating the wing motion of hovering insects, Jardin *et al.* (2009) found that two distinct vortex pairs, similar to the vortical structures reported in this work, arise at stroke reversal around both the leading and trailing edges when the angle of attack is higher than  $45^\circ$ . As the angle of attack decreases, the starting-stopping vortex behaviour was reported to occur at the stroke reversal. Similar tendency can be found in the computational results of Wang (2004) (figure 3 therein).

## 2.4 Scaling laws

On the basis of the flow visualisation results, we construct a simple model to estimate the thrust. We start with dimensional analysis. The period-averaged thrust,  $\langle F_t \rangle$ , must be a function of fluid properties, plate dimensions, stroke frequency and amplitude, thus we write as

$$\langle F_t \rangle = f(\rho, \mu, R, h, w, f, \theta_m). \quad (2.1)$$

The Buckingham II theorem (Buckingham, 1914; Sonin, 2004) allows us to write the following dimensionless relationship:

$$\frac{\langle F_t \rangle}{\rho h^4 f^2} = f(\text{Re}, \eta, \frac{R}{h}, \theta_m). \quad (2.2)$$

To go beyond this dimensional analysis, which lists only the dimensionless parameters determining the scaled thrust, and understand the force production mechanism, we model the hydrodynamic forces acting on the angularly reciprocating plate. Two kinds of forces act on a flapping plate in general, one due to added mass and the other due to circulation. The force  $F_a$  due to added mass is generated as the plate velocity changes. For an angularly reciprocating plate whose angle is a sinusoidal function of time, the time mean of  $F_a$  over a period is zero because the added mass of a flapping plate in the rigid body motion can be assumed to be constant (Newman, 1977). The vortical force,  $\mathbf{F}_c$ , is the time derivative of the vortical impulse,  $\mathbf{I}$ :  $\mathbf{F}_c = \dot{\mathbf{I}}$ . The mean force,  $\langle \mathbf{F}_c \rangle$ , which is of interest here, is scaled as

$$\langle \mathbf{F}_c \rangle = \frac{1}{T} \int_0^T \dot{\mathbf{I}} dt \sim \frac{1}{T} \Delta \mathbf{I}, \quad (2.3)$$

where  $T$  is the period of flapping and  $\Delta \mathbf{I}$  accounts for  $\mathbf{I}$ 's produced by every new vortex structure within a cycle. In each cycle, two kinds of vortical structures are produced twice, i.e. two APV's and two SRV's are formed. Hence, we write

$$\Delta \mathbf{I} \sim 2(\mathbf{I}_A + \mathbf{I}_S), \quad (2.4)$$

## 2.4 Scaling laws

---

where the subscripts  $A$  and  $S$  denote the APV and SRV, respectively.

The vortical impulse is determined by the distribution of vorticity in the flow field. Intense vorticity is distributed around the plate edge where the separation of vortical structures occurs. Thus, we can approximate the magnitude of the vortical impulse  $\mathbf{I}$  using a vortex loop model:  $I = \rho\Gamma wh$ , where  $\rho$  is the density of water and  $\Gamma$  is the strength of the vortex loop. Then the magnitude of mean circulatory force,  $\langle F_c \rangle$ , is scaled as

$$\langle F_c \rangle \sim \rho wh f(\Gamma_A + \Gamma_S). \quad (2.5)$$

Before proceeding to determine the magnitude of  $\Gamma$  we note that the circulation of the bottom edge is greater than that of the top edge due to a difference in linear acceleration. The Kelvin theorem dictates that vorticity is distributed over the plate surface to compensate for the difference in the circulation magnitudes at the edges. Hence, the total effective circulation induced by flapping can be scaled with the circulation at the bottom edge.

When a plate accelerates in a fluid, the pressure difference between the front and back faces is induced because the fluid must accelerate with the plate, which can be related to the acceleration of a virtual cylinder of fluid about the plate. This pressure difference cannot be maintained at the bottom edge and a vortical structure is then produced. By modelling the bottom edge as a blade element having a height  $\Delta h$  and width  $w$  as shown in figure 2.1, we get the added mass of the corresponding rectangular plate,  $\sim \rho w^2 \Delta h$  (Newman, 1977). Then, the added-mass force at the bottom edge is given by

$$F_a \sim \rho w^2 a \Delta h, \quad (2.6)$$

where the acceleration  $a$  is scaled as  $a \sim Rf^2\theta_m$ . Writing  $F_a \sim \Delta p_a w \Delta h$ , we get  $\Delta p_a \sim \rho w Rf^2\theta_m$ . Here  $\Delta h$  is considered small enough to ignore the variation of  $\Delta p_a$  along that length. The vortical structure that counterbalances this pressure difference can be modelled as a vortex sheet with tangential velocity discontinuity,  $\Delta U_t$ , across the plate (Theodorsen, 1935).

## 2.4 Scaling laws

---

Since  $\Delta p_a$  induces a vortical structure, we write  $\Delta p_a \sim \frac{1}{2}\rho(\Delta U_t)^2$ . The vortex sheet should be shed tangentially to the plate (Wu *et al.*, 2006) and evolved into a vortical structure, allowing us to write  $\Delta U_t \sim \Gamma_i/h$ . Therefore, we obtain the following scaling approximation of circulation:

$$\Gamma_i \sim hw^{1/2}R^{1/2}f\theta_m^{1/2}. \quad (2.7)$$

Because this procedure applies to both APV and SRV produced by sinusoidal reciprocation,  $i$  can be either A or S. The mean thrust for a period of flapping,  $\langle F_t \rangle$ , corresponding to  $\langle F_c \rangle$ , can be finally scaled as

$$\langle F_t \rangle \sim \rho h^2 w^{3/2} R^{1/2} f^2 \theta_m^{1/2}. \quad (2.8)$$

To validate our scaling analysis, we first measured the magnitude of circulation  $\Gamma$  experimentally. Limited by the power of the laser generator and the viewing area of the high-speed camera, we obtained vorticity fields for six cases with varying  $w$  (6, 8 and 12 cm),  $h$  (2, 4 and 6 cm) and  $f$  (0.1 and 0.2 Hz). Figure 2.5 shows the measurement results of  $\Gamma$  at the bottom edge when the instantaneous  $\theta$  is  $16^\circ$ . The circulation  $\Gamma$  was obtained by integrating the vorticity around the tail tip vortex. We see that  $\Gamma$  increases linearly with  $hw^{1/2}R^{1/2}f$ , consistent with our scaling law, (2.7), although  $\theta_m$  is held constant in this work.

We now turn to the thrust, which could be measured across wide ranges of  $w$ ,  $h$  and  $f$ . Figure 2.6 plots the mean thrust of 72 cases. Figure 2.6(a) shows that the mean thrust of a given geometry of plate increases linearly with  $f^2$  while the data are scattered for differing  $h$  and  $w$ . All of the scattered data are collapsed onto a master curve when plotted according to the scaling law (2.8) as shown in figure 2.6(b). It is remarkable that our simple theory correctly captures the scaling relations of the period-averaged value of thrust, whose actual temporal evolution is by no means simple. This close agreement arises from the fact that the thrust is dominated by the impulsive generation of vortices (leading to the peaks in thrust), with

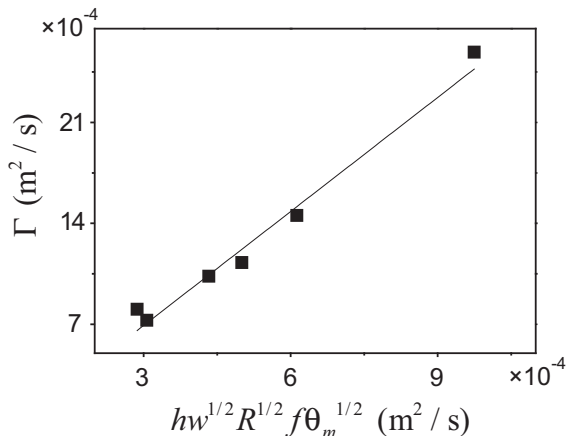


Figure 2.5: Measurement results of circulation plotted according to the scaling law, (2.7). The slope of the best-fitting line is 2.6.

which our theory is mainly concerned. Also, our simplification is supported by the fact that both added mass and the shape of vortical structures are determined by the plate geometry and that the plate rotation is sinusoidal.

The scaling law (2.8) can be rearranged so that the mean thrust scaled by  $\rho h^4 f^2$  is expressed as a function of the normalized stroke amplitude  $\beta = 2R\theta_m/h$  and the aspect ratio  $\eta = w/h$ :

$$\frac{\langle F_t \rangle}{\rho h^4 f^2} \sim \beta^{1/2} \eta^{3/2}, \quad (2.9)$$

where we dropped a numerical prefactor because the scaling relation is the principal interest. We see that our foregoing force analysis unveils the functional dependency of the scaled thrust on the dimensionless parameters which were merely listed in (2.2). Figure 2.7 replots the experimental data used in figure 2.6 according to (2.9), again validating our scaling law. Comparing the dimensionless relationship (2.2) and scaling law (2.9), it turns out that the scaled thrust is rather independent of  $Re$  in the range of  $Re$  tested in this work, i.e.  $2.7 \times 10^3$  to  $2.9 \times 10^4$ . We suppose that it is because in this range of  $Re$ , the ratio of convective to diffusive length

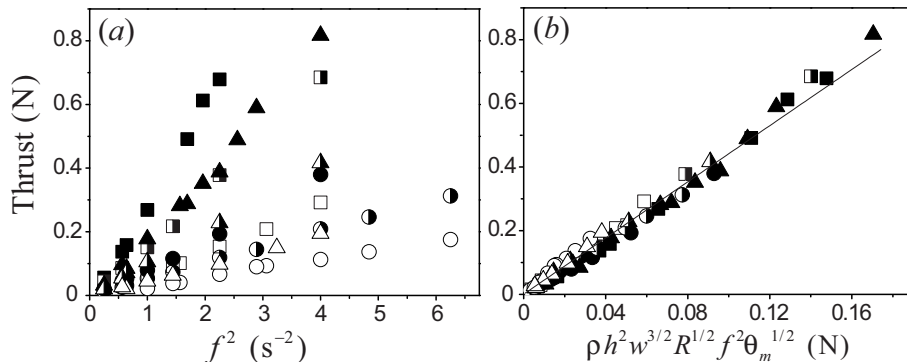


Figure 2.6: The mean value of period-averaged thrust,  $\langle F_t \rangle$ . (a)  $\langle F_t \rangle$  versus  $f^2$  for different plate geometries. The circles, triangles and squares correspond to the plates of  $w = 6, 9$  and  $12$  cm, respectively. The empty, half-filled and filled symbols correspond to the plates of  $h = 4, 6$  and  $8$  cm, respectively; (b)  $\langle F_t \rangle$  plotted according to the scaling law (2.8). The straight line is drawn by the least-square method. The slope of the best-fitting line is 4.7.

scales is large enough to approximate the separating flow around the plate as a vortex sheet, a key assumption of the vortex topology in our model. The dimensionless parameters  $R/h$  and  $\theta_m$  appear together as a product in  $\beta$ , a normalized stroke amplitude.

The bollard pull condition treated here is similar to having a Strouhal number, defined as  $St = hf/\hat{U}$  based on forward velocity  $\hat{U}$ , of infinity. Thus, the comparison with previous studies on the behaviour of flapping foils at very large Strouhal numbers may provide further validation of our theory. However, the range of  $St$  investigated thus far is rather limited mainly because most of flapping foils in natural situations work in a narrow range of  $St$ :  $0.2 < St < 0.4$  (Taylor *et al.*, 2003). Among few studies that dealt with the cases where the flapping velocity is at least comparable to the forward propulsion velocity, Dong, Mittal & Najjar (2006) provided detailed parameter values that allow the comparison of our theory with their results. As discussed in the Appendix A, the comparison supports

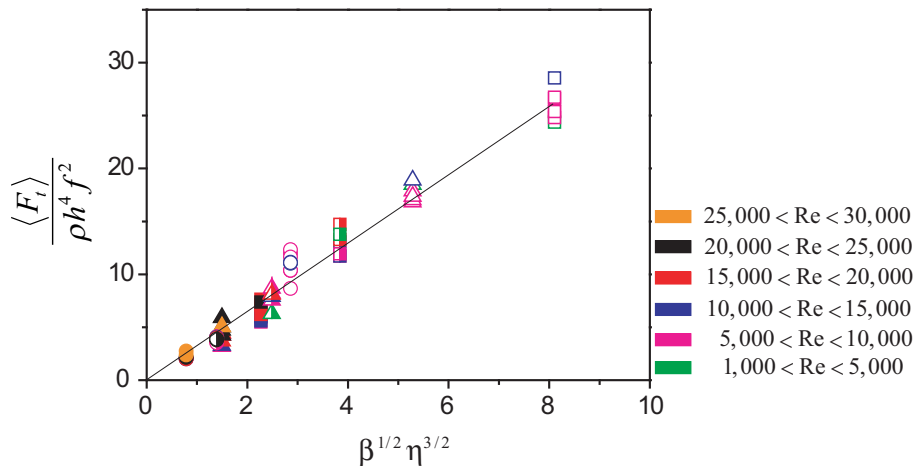


Figure 2.7: Dimensionless mean thrust,  $\langle F_t \rangle / \rho h^4 f^2$ , versus  $\beta^{1/2} \eta^{3/2}$  for different plate geometries. The circles, triangles and squares correspond to the plates of  $w = 6, 9$  and  $12$  cm, respectively. The empty, half-filled and filled symbols correspond to the plates of  $h = 4, 6$  and  $8$  cm, respectively. Regardless of the Reynolds number varying between  $2.7 \times 10^3$  and  $2.9 \times 10^4$ , the experimental data follow the scaling law (2.9). The slope of the best-fitting line is 3.3.

our scaling law favourably.

## 2.5 Conclusions

In summary, we visualised vortex structures around a flapping plate undergoing angular reciprocation with no freestream, and measured the consequent thrust. In contrast to the conventional starting-stopping vortex behaviour, the angularly reciprocating plate was shown to generate two distinct vortical structures as it accelerates and reverses its direction due to a high angle of incidence between the plate and relative flow velocities. This topological difference in vortical structure affects the resulting force history. While the lift during the starting phase of the plate motion gradually increases in the starting-stopping vortex paradigm, an instantaneous force

## 2.5 Conclusions

---

peak is induced when the plate accelerates in the angular reciprocation. In addition, the separation of the stopping vortex near the stroke reversal leads to a loss of lift in the starting-stopping vortex paradigm, whereas the SRV of angular reciprocation is believed to play a crucial role in force generation. The scaling law based on the assumption that the thrust production is dominated by the vortical impulses of APV and SRV was shown to agree well with the experimental measurements. We anticipate that the analysis of this canonical flapping configuration can greatly benefit the fundamental understanding of flapping fluid mechanics at high angles of incidence. It is worth further study to examine how the change in forward propulsion velocity and consequent variation in incident flow angle influence the wake dynamics around the foil and the force history. Also, our theory for thrust generation can be a useful guideline for designing flapping-based biomimetic robots.

## Chapter 3

# Hydrodynamic principles of the evolutionary selection of fish caudal fin shapes

### 3.1 Introduction

To increase their probability of survival, animals are believed to have optimized shapes as a consequence of millions of years of evolution. To understand the evolutionary direction (Gazzola *et al.*, 2014; Kim *et al.*, 2011; Motani, 2002; Park *et al.*, 2014) and design bio-inspired engineering systems (Floreano & Mattiussi, 2008; Pfeifer *et al.*, 2007), it is highly desirable to reveal the general physical laws underlying natural selection. The stereotypical shape of the caudal fin of highly migratory aquatic animals, i.e., a lunate tail with a high aspect ratio, is one of the representative examples evolutionary optimization, and is known to provide an advantage in terms of hydromechanical efficiency (Chopra & Kambe, 1977). On the other hand, the caudal fin of small non-migratory fish, which live in relatively weak currents and have a small habitat radius, seems to follow completely different design rules. This caudal fin has a variety of leading and trailing edge shapes characterized as forked, emarginated, and rounded

## 3.2 Experimental apparatus

---

caudal (Swainson, 1839), along with much smaller aspect ratios than that of highly migratory aquatic animals. However, the hydrodynamic principle underlying the evolutionary selection for the caudal fin shape of small fish is poorly understood.

The main interest of the present research is providing integrative insight into the evolutionary selection of the caudal fin shape of small fish at the elementary level. This can be summarized as finding the answers to the following two questions. 1) Why do the shapes of the caudal fins of small fish vary in contrast to the stereotypical lunate tails of large cruising fish? 2) Why is the aspect ratio of the caudal fins of small fish smaller than that of large cruising fish? One possible reason for these discrepancies is that the caudal fins of small and large fish are mainly used for different purposes. The caudal fin of large cruising fish is mainly utilized for length cruising, whereas the caudal fin of small fish is mainly used for impulsive motions such as sprinting for escaping predators or capturing prey. Such differences influence the dominant force-production mechanism. The thrust in impulsive motion is dominated by the acceleration-reaction owing to high Strouhal numbers, whereas the thrust mainly relies on a hydrodynamic lift while cruising (Sfakiotakis *et al.*, 1999).

## 3.2 Experimental apparatus

The apparatus used for measuring the flow fields and the resultant thrust is illustrated in figure 3.1(a). A tail made from a flat acrylic with a thickness of 3 mm was attached to a metallic rod with a length of 12 cm, which angularly reciprocates about the z-axis. The single-degree-of-freedom oscillation was driven by a DC motor and a scotch-yoke mechanism. The stroke angle of the sinusoidal rotation  $2\theta_m$  was fixed to 35 degrees. The frequency  $f$  ranges from 0.1 to 2.5 Hz, the width of the plate  $w$  ranges from 1.5 to 22.5 cm, and the height  $h$  ranges from 1.2 to 20 cm. The apparatus was immersed in a transparent water tank measuring 75, 55, and 33 cm in

## 3.2 Experimental apparatus

---

the x-, y- and z-directions, respectively. The velocity fields and vorticity contours were obtained based on the two-dimensional digital particle image velocity (DPIV) using seeding particles as hydrogen bubbles. To visualize the bubbles, the central plane perpendicular to the flapping tail was illuminated using a 2 W continuous laser with a 532 nm wavelength applied through a slit. The captured images were analyzed using DPIV software to generate the velocity fields with an interrogation size of  $32 \times 32$  and a 50 % overlap. The derived velocity vectors were validated using the dynamic mean value operator. The error vectors were interpolated using a kriging interpolation. The number of error vectors was within 2 % of the total number of velocity vectors.

Herein, we investigate the hydrodynamics of an angularly reciprocating flapping tail as an elementary model of the caudal fin oscillation in small fish. The center of oscillation remains stationary while a flapping motion is applied, which simulates a situation in which the caudal fin is used for sprinting from a stationary state. This condition captures the physical essence in which the force production is dominated by an acceleration-reaction for high Strouhal numbers. To examine systematically the parametric variations in the tail dimensions and shapes, the tail is simplified into a delta shape, as shown in figure 3.1(a). The design parameters of the flapping tail include the width  $w$ , height  $h$ , sweepback angle  $\Lambda$ , and side length  $l_s$ , and its kinematic parameters are the rotation radius of the tail tip  $R$ , stroke frequency  $f$ , and stroke angle  $\theta_m$ . The shapes of the tail are rectangular or trapezoidal shapes when the sweep back angle or side length is zero. The hydrodynamics of a flapping tail with high Strouhal numbers is governed by three non-dimensional variables (Lee *et al.*, 2013a): the Reynolds number,  $\text{Re} = Uh/\nu$ ; normalized stroke amplitude,  $\beta = 2R\theta_m/h$ ; and aspect-ratio,  $\text{AR} = w^2/S$ . In our experiments, the Reynolds number, defined based on the period-averaged 0.7 radius length speed, i.e.,  $U = 4(0.7R)\theta_m f$ , ranges from  $1.3 \times 10^3$  to  $1.09 \times 10^5$ . The normalized stroke

### 3.2 Experimental apparatus

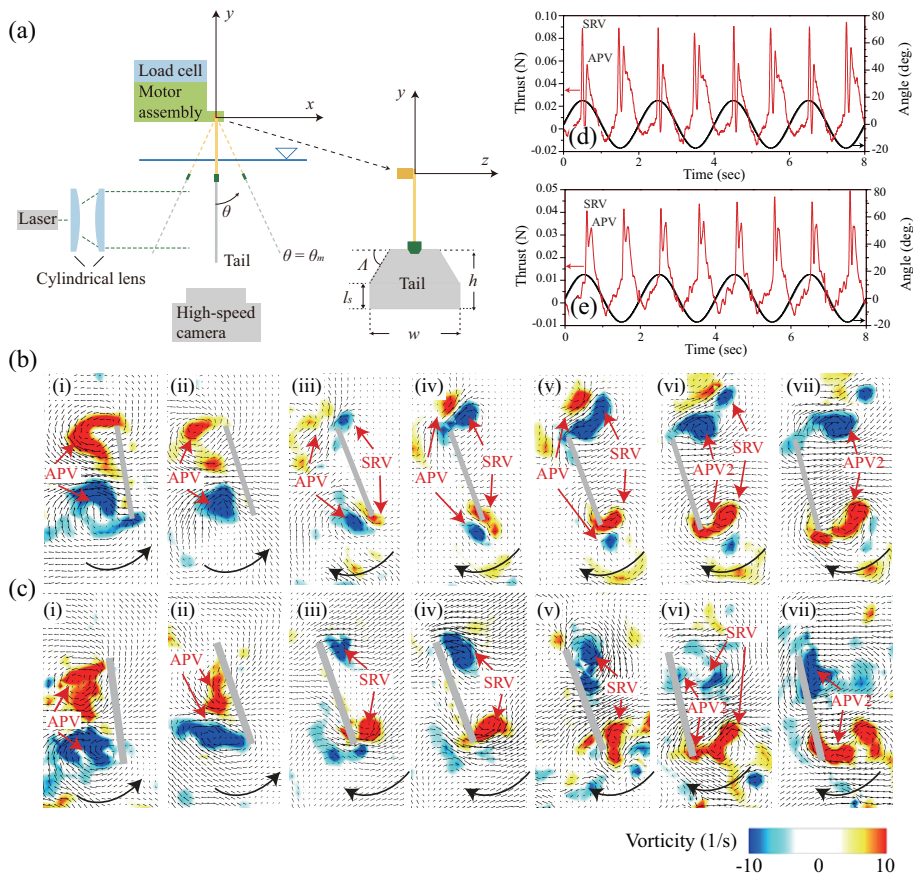


Figure 3.1: Experimental apparatus and measurements of flow fields and thrusts. (a) Schematic diagram of the experimental apparatus. (b, c) Flow fields and vorticity contour around rectangular and trapezoidal flapping tail, respectively, with  $[h, w] = [4, 12]$  cm, oscillating at 0.2 Hz. The round arrow indicates the instantaneous direction of the tail motion. (d, e) Measured thrust of the rectangular and trapezoidal flapping tail, respectively, with  $[h, w] = [4, 12]$  cm, oscillating at 0.5 Hz.

amplitude ranges from 0.9 to 6.7, and the aspect ratio ranges from 0.075 to 17.

## 3.3 Results

### 3.3.1 Flow measurements

We first measured the flow fields around the rectangular and trapezoidal shapes of a flapping tail, as shown in figure 3.1(*b, c*) to examine the fundamental thrust production mechanism. Thrust is produced through two distinct momentum transfer processes related to the tail deceleration and acceleration. When the tail decelerates and reverses, a strong vortical flow is generated around the tail edges, as shown in figure 3.1(*b, iii-iv*) and (*c, iii-iv*), which entrains the momentum jet pointing back surface of the tail. In return, the flapping tail experiences thrust as shown by the sharp force peak around the stroke reversal shown in figure 3.1(*d, e*). Subsequently, as the tail advances after a stroke reversal, a second vortical structure is generated by the tail acceleration, as shown in figure 3.1(*b, vi-vii*) and (*c, vi-vii*). The momentum transfer through the generation of this second vortical structure is another source of thrust, as shown by the second force peak in time history of the thrust in figure 3.1(*d, e*). The time history of the thrust then exhibits a curve dominated by two force peaks corresponding to the generation of the stroke reversal vortical structure (SRV) and the acceleration phase vortical structure (APV), respectively.

### 3.3.2 Scaling laws

The scaling law estimating the thrust is constructed as follows. It should be noted that the scaling law presented in this work was developed from the scaling analysis for the thrust of an angularly reciprocating rectangular plate proposed by Lee *et al.* (2013a). We start from a dimensional analysis. The period-averaged thrust,  $T$ , should be a function of

### 3.3 Results

the fluid properties, stroke frequency, stroke angle, tail dimensions, and shapes:  $T = f(\mu, R, h, S, w, f, \theta_m, \Lambda)$ . Applying the Buckingham  $\Phi$  theorem (Buckingham, 1914; Sonin, 2004), we obtain the following dimensionless relationship:

$$\frac{T}{\rho h^4 f^2} = f(\text{Re}, \text{AR}, \eta, \frac{h}{R}, \Lambda). \quad (3.1)$$

We next model the hydrodynamic forces acting on the flapping tail based on the flow observations. The thrust is produced by a reaction of the momentum imparted to the vortical structures, i.e., APV and SRV. The period averaged thrust,  $T$ , can then be scaled as a product of the frequency,  $f$ , and the momentum imparted to the vortical structures per cycle,  $\Delta I$ ;  $T \sim \Delta f$ . The momentum imparted to the fluids is composed of two parts associated with the APV and SRV as  $\Delta I \sim I_A + I_S$ , where subscripts  $A$  and  $S$  denote the APV and SRV, respectively. The flow around a flapping tail is highly separable, and most of the vorticities are concentrated around the tail edges. Thus, the momentum induced by the vortical structure is modeled as  $I_i \sim \rho \Gamma_i S$ , where  $\Gamma_i$  is the characteristic circulation of the vortical structure, and  $S$  is the area of the tail. The characteristic circulation  $\Gamma_i$  is scaled with the strength of the vortex at the bottom tip.

The scaling relation for the characteristic circulation,  $\Gamma_i$ , is obtained by applying the following physical constraint. The pressure difference across the back and front surfaces should be zero at the bottom tip of the tail where the vortical structures are separated into the flow field (Theodorsen, 1935; Wu *et al.*, 2006). Two distinct effects inducing the pressure difference should then counter balance each other: one is the acceleration of the tail, and the other is the tangential velocity discontinuity induced by the vortex sheet on the tail (Theodorsen, 1935; Wu *et al.*, 2006). This physical constraint enables us to write the following relation,  $\Delta p_a \sim \rho(\Delta U_t)^2$ , where  $\Delta p_a$  is the pressure difference induced by the acceleration, and  $U_t$  is the velocity discontinuity. The pressure difference induced by the acceleration,

### 3.3 Results

$\Delta p_a$ , can be scaled with the added mass force as  $F_a \sim \rho w^2 h a$ , where  $a$  is the acceleration at the tail tip. The pressure difference is then scaled as  $\Delta p_a \sim F_a / (hw) \sim \rho w a$ . Next, the velocity discontinuity can be related to the strength of the vortex at the bottom tip as  $\Delta U_t \sim \Gamma_i / h$  because the vortex sheet on the tail surface is separated tangentially and evolves into the vortex at the tail tip. Assuming that the motion of the tail follows a simple harmonic function in time, the deceleration and acceleration of the tail can be scaled with an identical equation,  $a \sim R \theta_m f^2$ , where  $R \theta_m$  is the distance traveled by the tail tip. Collecting all of these equations, the characteristic circulation is scaled as  $\Gamma_i \sim hw^{1/2} R^{1/2} \theta_m^{1/2} f$ , and finally, the thrust is scaled as

$$T \sim \rho S h w^{1/2} R^{1/2} \theta_m^{1/2} f^2. \quad (3.2)$$

To validate our scaling law, we compared 195 cases of thrust data measured by varying the tail dimensions, flapping frequency, stroke amplitude, and tail shapes based on our scaling law (3.2). As shown in figure 3.2(a, b), all of the data collapsed onto a single scaling curve, whereas the data were initially scattered by differing the tail dimensions and shapes when plotted with respect to  $f^2$ . We further examined the non-dimensional relation of the thrust by dividing both sides of equation (3.2) with  $\rho h^4 f^2$ . Equation (3.2) can be rearranged as follows:

$$\frac{T}{\rho h^4 f^2} \sim \frac{\eta^{5/2} \beta^{1/2}}{\text{AR}}. \quad (3.3)$$

The non-dimensional thrust is a function of the width-to-height ratio  $\eta$ , non-dimensional stroke amplitude  $\beta$ , and aspect-ratio AR, whereas it is independent of the Re and variations in the tail shape. In the range of Re studied in this work, i.e.,  $10^3 - 10^5$ , where the convective-to-diffusive length scale is sufficiently large to approximate a separating flow around a tail as a vortex loop model, our non-dimensional scaling law is in good agreement with the experimental measurements, as shown in figure 3.2(c).

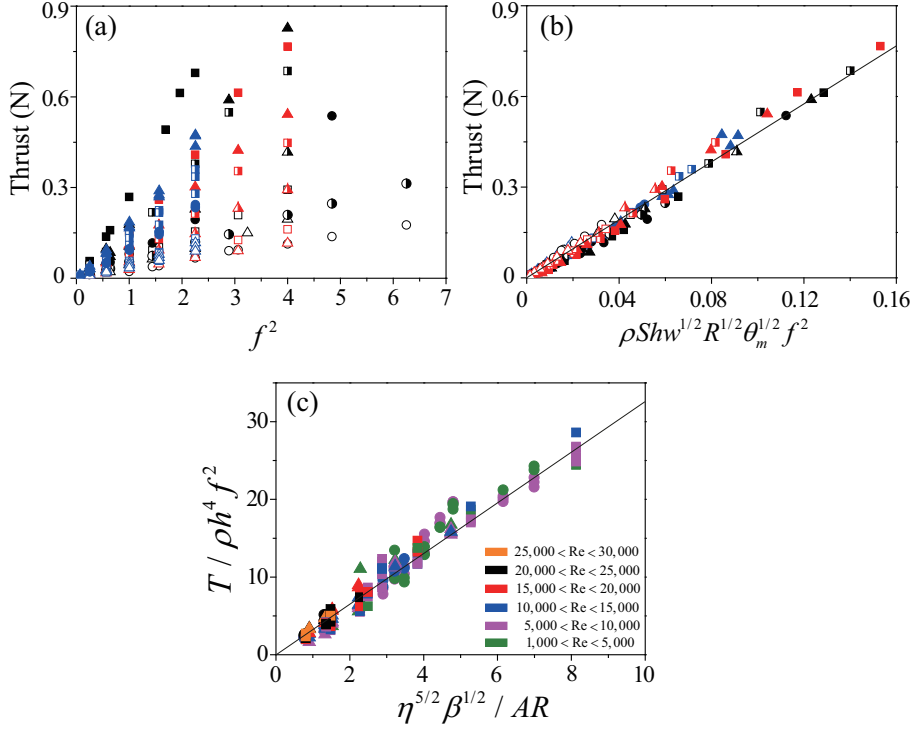


Figure 3.2: Comparison of period-averaged thrust using the scaling law. (a, b) Plots of period-averaged thrust versus  $f^2$  and the scaling law in equation (2), respectively, for differing the tail dimensions and shapes. The black, red, and blue colors correspond to the rectangular, trapezoidal, and delta shapes, respectively. The circles, triangles, and squares correspond to plates of  $w = 6, 9,$  and  $12$  cm, respectively. The empty, half-filled, and filled symbols correspond to plates of  $h = 4, 6,$  and  $8$  cm, respectively. (c) Dimensionless thrust,  $T/(\rho h^4 f^2)$ , versus  $\eta^{5/2} \beta^{1/2} / AR$  for the different tail dimensions and shapes. The circles, triangles, and squares correspond to a delta, trapezoidal, and rectangular shaped tail, respectively.

It should be noted that the thrust of an angularly reciprocating tail is predicted based on the universal scaling law regardless of the variations in tail shape. This is one of the key characteristics differentiating acceleration-reaction based thrust production from lift-based thrust production. For lift-based thrust production, the vorticity and resulting pressure distribution over the tail are closely related to the tail geometry<sup>7</sup>. Large cruising fish therefore have a strictly standardized tail shape that optimizes the vorticity distribution over the tail surface (Chopra & Kambe, 1977; Lighthill, 1970). On the other hand, for acceleration-reaction based thrust production, the vorticity distribution over the surface is marginal because the flow is highly separable and most of the vorticities are concentrated around the tail edges. Therefore, rather than selecting the shape that optimizes the vorticity distribution over the tail surface, satisfying the physiological and environmental requirements of individual species is a higher priority in determining the tail shape. This may be the physical background allowing for a great variety of tail shapes for small fish, in contrast to the stereotypical caudal fin shape of large cruising fish.

#### 3.3.3 Optimal aspect-ratio

Based on the scaling law, we next investigated the effect of the aspect ratio on the thrust and efficiency. The thrust of a rectangular flapping tail was measured by varying the aspect-ratio over two orders of magnitude, i.e., from 0.075 to 17. The trend in thrust curves is abruptly changed at an aspect ratio of around 0.7, as shown in figure 3.3(a). Before the transition, the thrust rapidly increases with the aspect-ratio, whereas after the transition, the thrust decreases with it. For a slender tail with an extremely low-aspect-ratio, the hydrodynamic forces can be modeled as an added-mass force based on the potential flow assumption (Ellington, 1984b; Lighthill, 1970), which is expressed as the added mass  $w^2h$  times the acceleration  $R\theta_m f^2$ ;  $T \sim \rho w^2 h R \theta_m f^2$ . The thrust before the transition was

### 3.3 Results

successfully predicted using the added mass force, as shown in figure 3.3(b). However, because the aspect ratio increases above the slenderness limit, the separated flow around the tail becomes prominent, thereby invalidating the theory based on the potential flow assumption. After the slenderness limit, the trend in thrust follows the prediction of our scaling law, as shown in figure 3.2(b, c) and figure 3.3(a), which considers the momentum imparted to the separated flows.

To examine the optimal aspect ratio for the thrust, we rearranged the scaling law in equation (3.2) into a function of the aspect ratio as

$$\tilde{T} \sim \frac{T}{\rho[(R\theta_m)^{1/2}S^{7/4}f^2]} \sim \text{AR}^{-1/4}. \quad (3.4)$$

Here,  $w$  and  $h$  are replaced by  $\text{AR}$  and  $S$  using the relations  $\text{AR} = w^2/S$  and  $S = wh$ . The aspect ratio maximizing the scaled thrust,  $\tilde{T}$ , therefore corresponds to the maximum thrust condition for the given tail area  $S$ , frequency  $f$ , and stroke amplitude  $R\theta_m$ . The scaled thrust,  $\tilde{T}$ , is plotted according to  $\text{AR}$  in figure 3.3(a). The thrust is maximized at the transition around an aspect ratio of 0.7, which corresponds to the slenderness limit, and after that point, the thrust decreases with the aspect ratio as a power of  $-1/4$ , as predicted by our scaling law (3.4). Therefore, the aspect-ratio around the slenderness limit is advantageous in maximizing the thrust in the given tail area and kinematics.

We next examined the optimal aspect ratio maximizing the efficiency. In general, the hydromechanical efficiency of aquatic animals is defined as a ratio of the work used for the propulsion to the total work conducted through the animal motion (Lighthill, 1970; Sfakiotakis *et al.*, 1999), i.e., the well-known Froude efficiency. However, the efficiency of an angularly reciprocating tail cannot be obtained using the conventional definition because the work used for the propulsion will be zero owing to the absence of forward motion. Instead, we introduce the hydrodynamic cost of endurance as a measurement of efficiency, which is analogous to the aerodynamic cost

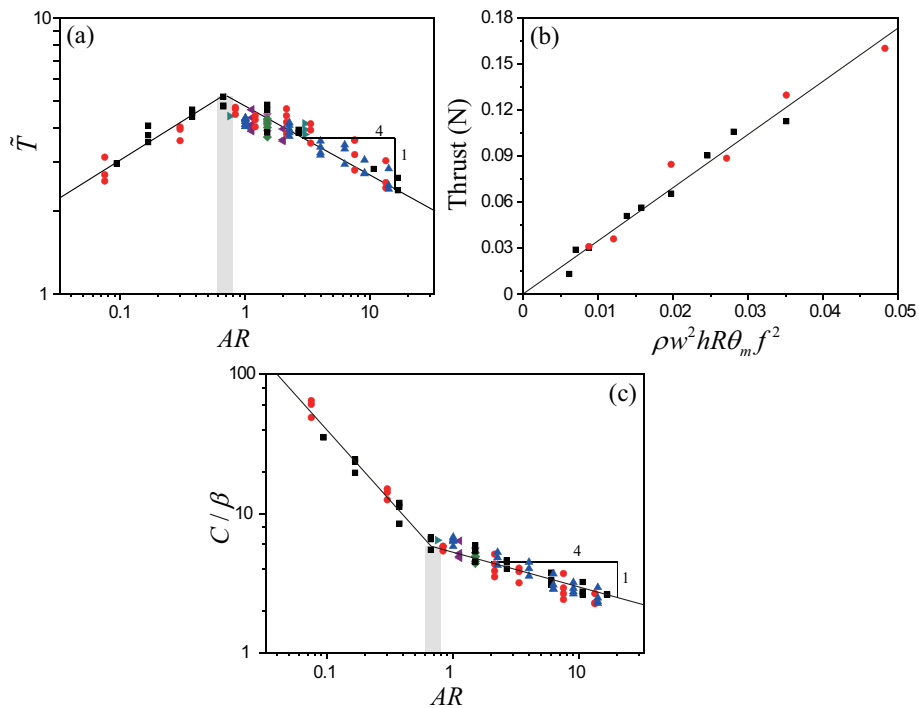


Figure 3.3: Effects of the aspect-ratio on the thrust and efficiency. (a) The scaled thrust,  $\tilde{T}$ , versus the aspect ratio. The circles, triangles, squares, diamonds, down-pointing triangles, and left- and right-pointing triangles correspond to rectangular tails with an area of 30, 36, 24, 96, 54, 72, and 48 cm<sup>2</sup>, respectively. (b) The thrust data before the slenderness limit versus the scaling law based on the added-mass force. (c) The ratio of hydrodynamic cost of endurance and non-dimensional stroke amplitude versus the aspect ratio.

of endurance in hovering insects (Lentink & Dickinson, 2009; Wang, 2008). The hydrodynamic cost of endurance  $C$  is defined as a dimensionless power to produce a unit thrust,  $C = Wf/TU_{ref}$ , where  $W$  is the work conducted by the tail motion defined as  $W = \int_0^{1/f} \overrightarrow{\tau}(t) \cdot \overrightarrow{\Omega}(t) dt$  with  $\tau$  and  $\Omega$  being the torque and angular velocity, respectively, and the reference velocity  $U_{ref} = (2T/\rho S)^{1/2}$  being constant for a given tail area  $S$  and thrust  $T$ . The inverse of the hydrodynamic cost of endurance is proportional to the efficiency of the angularly reciprocating tail.

The scaling law for the hydrodynamic cost of endurance can be obtained using the scaling relation for the work conducted by the tail motion,  $W \sim TR\theta_m \sim \rho S h w^{1/2} R^{3/2} \theta_m^{3/2} f^2$ , and equation (3.2) as

$$C \sim \left(\frac{R\theta_m}{h}\right) AR^{-1/4} \sim \beta AR^{-1/4} \quad (3.5)$$

The ratio of the hydrodynamic cost of endurance and the non-dimensional stroke amplitude is plotted according to the aspect ratio, as shown in figure 3.3(c). The hydrodynamic cost of endurance decreases rapidly with the aspect-ratio up to the slenderness limit, implying a drastic improvement in efficiency. The decreasing trend in the hydrodynamic cost of endurance stabilizes after the slenderness limit, reaching a power of -1/4 corresponding to the scaling law (3.5).

### 3.4 Discussion

From the trends in thrust and efficiency, we can infer three optimal strategies to determine the aspect ratio. For the purpose of thrust maximization, the aspect ratio around the slenderness limit, i.e., 0.7, is preferred, whereas the aspect ratios below the slenderness limit are unfavorable in terms of both thrust and efficiency. On the other hand, the efficiency is continuously improved as the aspect ratio increases, although there is a loss in thrust above the slenderness limit. Therefore, maximizing the aspect ratio within the limitation of structural requirements is advantageous

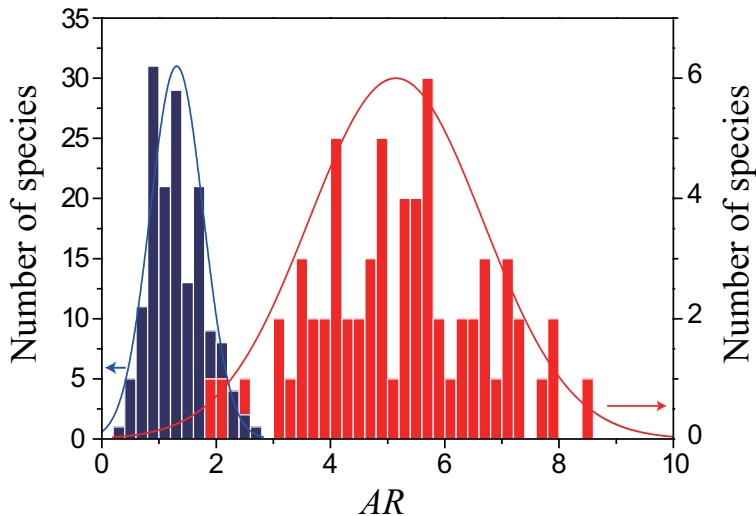


Figure 3.4: Distribution of the aspect ratio of highly migratory aquatic animals (red) and non-migratory freshwater fish (blue).

for the purpose of improving the efficiency. The third strategy is selecting the intermediate aspect-ratio considering the tradeoff between the thrust and efficiency under the physiological and environmental requirements of individual species.

To examine what strategies are adopted by actual fish, we compared the distribution of the aspect ratio of highly migratory aquatic animals and non-migratory freshwater fish, which are expected to have a high priority in terms of efficiency improvement or thrust maximization, respectively. As shown in figure 3.4, highly migratory aquatic animals usually have a high aspect ratio, which is advantageous to their efficiency. On the other hand, non-migratory freshwater fish generally have a smaller aspect ratio than highly migratory aquatic animals. The highest number of species is distributed within an aspect ratio ranging between 0.6 and 0.8, which corresponds to the slenderness limit that maximizes the thrust in the given tail area and kinematics. The second-highest number of species is distributed within the aspect ratio ranging between 1.2 and 1.4, where the efficiency

is expected to be improved by about 15 % at the expense of a loss in thrust with equal percentage compared to the thrust maximization condition. Only 3.8 % of non-migratory freshwater fish are distributed within the aspect ratio below the slenderness limit, which is a detriment in terms of both thrust and efficiency. These results show that small fish in nature adopt the following three strategies corresponding to our study: 1) an aspect ratio below the slenderness limit is avoided, 2) a considerable number of small fish tune the aspect ratio of the caudal fin with the slenderness limit for the purpose of maximizing their thrust, and 3) a large number of non-migratory fish species have selected a low-to-moderate aspect-ratio considering the tradeoff between the thrust and efficiency, which is still much smaller than that of large cruising fish, implying that their sprinting ability has a higher priority than their efficiency.

We conclude this chapter with a summary and answers to previously suggested questions on the caudal fin shape of small fish. We examined the hydrodynamics of an angularly reciprocating tail as an elementary mode of the caudal fin oscillation of small fish while sprinting. The thrust of the flapping tail originates from the added mass force below the slenderness limit around an aspect ratio of 0.7. Above the slenderness limit, the thrust can be predicted based on a universal scaling law that considers the reaction of the momentum imparted to the vortical structures generated by the tail motion regardless of the tail shape. The thrust in the given tail area and the kinematics are maximized around the slenderness limit, and the efficiency increases continuously with the aspect ratio. Based on these results, we can provide answers to the previously suggested questions on the caudal fin shape of small fish. First, small fish have a variety of tail shapes preferentially satisfying the physiological and environmental requirements of individual species because their thrust is loosely related to their tail shape owing to the dominant influence of the separated flows around the tail edges. Second, small aquatic animals have selected a low aspect ratio,

### 3.4 Discussion

---

but one above the slenderness limit, to improve their sprinting ability at the expense of their efficiency. This seems to be an inevitable choice for small aquatic animals because their sprinting capability is as important as their efficiency in terms of survival from predators.

## Chapter 4

# A scaling law for the lift of hovering insects

### 4.1 Introduction

Insects can move more freely in air than most other creatures on earth. In particular, insect hovering is one of the most fascinating acrobatic flight modes that has defied an explanation in terms of conventional aerodynamics for decades. Since a quasi-steady analysis of conventional aerodynamics was considered inappropriate for explaining the hovering dynamics (Ellington, 1984a,b), unsteady mechanisms have been actively sought that can rationalize the aerodynamic force production through flapping. Several pioneering studies have found important unconventional mechanisms of hovering insects, such as the leading-edge vortex (Ellington *et al.*, 1996), wake capture and rotational mechanisms (Dickinson *et al.*, 1999).

Wing flaps of hovering insects can be largely decomposed into a translational mode and a rapid rotational stroke-reversal mode, which contribute to lift in different ways. The unusually large lift produced during the translational mode was explained by a highly stabilized leading edge vortex that is attached to a wing even above a critical angle of attack (Ellington *et al.*,

1996). It was suggested that the wing rotation during stroke reversal produces instantaneous force peaks via the Kramer effect and interactions with previously existing wake structures (Dickinson *et al.*, 1999). The central concern of scientists has now moved to more specific issues, such as measuring the precise three-dimensional kinematics of flapping wings (Liu & Sun, 2008; Mou *et al.*, 2011; Walker *et al.*, 2010; Willmott & Ellington, 1997a,b), analysing the time history of aerodynamic forces using dynamically scaled model wings (Fry *et al.*, 2005; Park & Choi, 2012; Sane & Dickinson, 2002), and numerically computing the flow structure and forces around the flapping wing (Bos *et al.*, 2008; Jardin *et al.*, 2009; Kweon & Choi, 2010; Liu & Aono, 2009).

Despite considerable advances in the understanding of fluid flows associated with insect hovering, a simple model to calculate forces that enable the insects to be airborne has been unavailable so far. Therefore, the main interest of the present research is providing a scaling law for the lift of hovering insects by elucidating an essential physical picture underpinning the aerodynamic feat.

We first revisit the conventional aerodynamics to check their relevance. In the conventional steady potential-flow theory, the lift of wing is obtained by the following two steps. First, the flow field around the wing is determined by the continuity equation and the boundary conditions composed of kinematic boundary condition on wing surface, smooth flow-off requirement at the trailing edge and far-field velocity. These kinematic relations give the velocity field and instantaneous circulation around the wing. Second, the Kutta-Joukowski theorem gives the lift of the wing as the product of the fluid density, free-stream velocity and the circulation bound to the wing (Newman, 1977). We suppose that the first kinematic step still holds for hovering insect wings because the separating flow is confined around the leading edge vortex and a smooth flow-off condition is recovered at the trailing edge (Birch & Dickinson, 2003; Sane, 2003). However, the second

## 4.2 Experimental apparatus

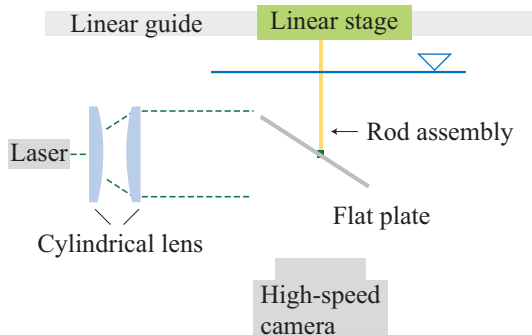


Figure 4.1: Experimental apparatus to visualize the flow field.

dynamic step is far from valid for hovering insect wings, which flap in a cyclic manner only after several chord lengths of travel. The separated vorticity of leading and trailing edges remains in the vicinity of the wing during most of stroke cycle (Jardin *et al.*, 2009; Liu & Aono, 2009; Poelma *et al.*, 2006). Instead of the Kutta-Joukowski theorem, we need to consider the momentum of the flow field induced by the vortical structures around the wing directly so as to model the lift.

In the following, therefore, we first approximate the instantaneous circulation of the leading edge vortex of hovering wings, which is assumed to play a dominant role in lift production, using the steady theory. We next measure the strength of leading edge vortex of dynamically scaled robot wing to test whether the steady aerodynamic theory provides a reasonable approximation for the strength of leading edge vortex. We then construct a novel model for the momentum induced by the vortical structure around the wing, which eventually determines the lift.

## 4.2 Experimental apparatus

A rectangular, rigid acrylic flat plate of 1 mm thickness is attached to a rod, which is driven by a linear stage (Newport IMS-LM), as shown in figure 6.1. The span of the plate is varied as 4, 6 and 8 cm and its chord

## 4.3 Results and discussion

---

is varied as 1.5, 2, 2.5, 3.5, and 4 cm. The flat plate and rod assembly is immersed in a water tank measuring 125, 15, and 25 cm in length, width and depth, respectively. The free surface is 10 cm above the top of the flat plate. While the plate is linearly translated along the length of the water tank, the velocity varies sinusoidally to complete a half-period as  $U(t) = U_0 \sin(\pi t/T)$  for the time interval  $0 < t < T$  with  $U_0$  being the maximum velocity. The velocity fields and vorticity contours are obtained by two-dimensional digital particle image velocimetry (DPIV). Polyamide particles of 50  $\mu\text{m}$  diameter are used as seeding particles. The central plane perpendicular to the plate is illuminated to visualize seeding particles with 8 W continuous laser of 532 nm wavelength through a slit. The images captured by a high-speed camera (Photron APX-RS), consisting of  $1024 \times 1024$  pixels, are analysed to generate a velocity field with a  $64 \times 64$  interrogation size and a 75% overlap. The derived velocity vectors are validated by a dynamic mean value operator. The vorticity field is obtained using a commercial graphic software based on the derived velocity field.

## 4.3 Results and discussion

### 4.3.1 Estimation of leading edge vortex strength

The shear flow separated at the leading edge of a hovering insect wing spirals into the leading edge vortex. Thus, the strength of the leading edge vortex is related to that of the shear flow generated on the wing, which is modeled as vortex sheets in the classical steady airfoil theory. We scale the strength of the leading edge vortex via the circulation around a three-dimensional wing (Newman, 1977),  $\Gamma$ , as

$$\Gamma \sim \frac{U\bar{c}\Lambda \sin \alpha}{\Lambda + 2}. \quad (4.1)$$

where  $\sim$  signifies “is scaled as,”  $U$  is the freestream velocity,  $\alpha$  is the angle of attack,  $\bar{c}$  is the mean chord.  $\Lambda = R/\bar{c}$  is the aspect ratio with  $R$  being

### 4.3 Results and discussion

---

the wing span. To test whether the present model provides a reasonable approximation for the strength of leading edge vortex on the wings operated in hovering conditions, we measured the vorticity of flows around a flat plate translating linearly at high angles of attack within a water tank. The ranges of all independent parameters, such as wing velocity, stroke distance, angle of attack, wing span, and chord, were selected to dynamically scale the characteristic values of the wings of hovering insects. The Reynolds number,  $Re = \rho U \bar{c} / \mu$  with  $\mu$  being the fluid viscosity, ranged from 200 to 3500, the dimensionless stroke amplitude ( $A$ , a ratio of stroke distance to mean chord) from 1.6 to 3.4,  $\alpha$  from  $25^\circ$  to  $70^\circ$ , and  $\Lambda$  from 1.5 to 2.7.

Figure 6.2(a) displays the representative velocity field and resulting vorticity contours. The leading edge vortex was identified using the criteria proposed by Lee *et al.* (2013a) as shown in figure 6.2(b). Figure 6.2(c) plots the measured instantaneous circulation in the leading edge vortex at  $t=T/2$  according to the scaling law (5.4) for 19 cases. All the data collapse onto a straight line with a slope 3.06, which is very close to the value expected from conventional aerodynamics,  $\pi$  (Newman, 1977).

#### 4.3.2 A model for lift

Now we move on to the lift of hovering insects by considering the momentum induced by the vortical structure generated by wing stroke. Because the vortical structure around the wing is characterized as the vortex loop over the wing (Jardin *et al.*, 2009; Liu & Aono, 2009; Poelma *et al.*, 2006), we approximate the momentum induced by the vortical structure,  $\Delta I$ , as a vortex loop around the wing. Thus, we write  $\Delta I \sim \rho \Gamma S \sim \rho \Gamma R \bar{c}$  (Dickinson, 1996; Lee *et al.*, 2013a; Wu *et al.*, 2006). The reaction force exerted on the wing due to the time-derivate of vortical impulse is scaled as  $F \sim \Delta I / T \sim \rho \Gamma R \bar{c} / T$ , which is perpendicular to the wing surface. Here,  $T$  is the flapping period.

### 4.3 Results and discussion

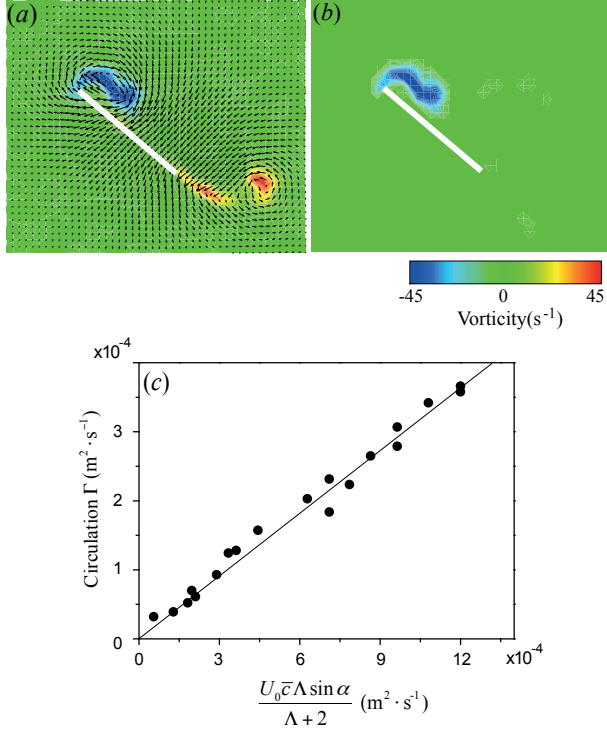


Figure 4.2: (a) Velocity field and vorticity contour around a translating wing with  $\text{Re}=2500$ ,  $\alpha=45^\circ$ ,  $\Lambda=1.7$  at  $t=T/2$ . (b) Isolated leading edge vortex around the identical wing. (c) Instantaneous circulation of leading edge vortex at  $t=T/2$  versus the scaling parameter  $U_0 \bar{c} \Lambda \sin \alpha / (\Lambda + 2)$ .

For the flapping translation of hovering insects, the linear velocity of the wing is scaled as  $U \sim \Phi R n$  with  $\Phi$  and  $n$  being the stroke amplitude and flapping frequency, respectively. Thus, circulation around the leading edge vortex can be scaled as  $\Gamma \sim \Phi R n \bar{c} \Lambda \sin \alpha / (\Lambda + 2)$  via the scaling relation (5.4). Combining these relations, we obtain the scaling approximations of lift and drag with respect to the stroke plane as  $L \sim \rho \Phi R^2 \bar{c}^2 n^2 \Lambda \sin \alpha \cos \alpha / (\Lambda + 2)$  and  $D \sim \rho \Phi R^2 \bar{c}^2 n^2 \Lambda \sin^2 \alpha / (\Lambda + 2)$ , respectively. The vertical component of the produced aerodynamic force balances the insect weight,  $W$ . The contribution of drag to the vertical component

### 4.3 Results and discussion

of the period-averaged aerodynamic force is very small compared to that of lift because the drags during up- and down-strokes are canceled out with each other except for dragonfly-like wing motions having severe asymmetry of up- and down-strokes (Wang, 2004). Balancing the vertical component of lift with the insect weight, we get

$$W \sim 0.5\rho\Phi R^2\bar{c}^2n^2 \frac{\Lambda \sin 2\alpha}{\Lambda + 2} \cos \beta. \quad (4.2)$$

where  $\beta$  is the stroke plane angle, that is, the angle between the horizontal and stroke planes.

We first compare our theory for lift with the data of 33 species of hovering insects from previously published papers that report the wing dimensions, flapping frequency and body weight (Ellington, 1984c,d; Ennos, 1989; Fry *et al.*, 2005; Liu & Sun, 2008; Mou *et al.*, 2011; Walker *et al.*, 2010; Weis-Fogh, 1973; Willmott & Ellington, 1997a,b). While the raw data scatter considerably when plotted against one of the most influential factors in the force production, the flapping frequency, figure 6.4(b), the data plotted according to the scaling law collapse onto a master curve, figure 6.4(c). Since most of those experimental observations do not report the angle of attack, we have simply modified the scaling law by ignoring  $\sin 2\alpha$ . Considering that the right-hand side of Eq. (5.5) varies by up to 6 orders of magnitude without  $\sin 2\alpha$ , the variation of  $\sin 2\alpha$  for different insects is indeed insignificant. It varies from 0.6 to 0.9 with the angle of attack changing from  $20^\circ$  to  $60^\circ$ . We validate our theory further with the data of six species of insects for which the angles of attack during each half-stroke are known (Ellington, 1984c,d; Fry *et al.*, 2005; Liu & Sun, 2008; Mou *et al.*, 2011; Walker *et al.*, 2010; Willmott & Ellington, 1997a,b). The weight of insect normalized by the dynamic pressure force,  $0.5\rho U^2 R\bar{c}$  with the characteristic wing tip velocity  $U \sim \Phi Rn$  and the wing area  $R\bar{c}$ , is scaled as

$$\frac{2W}{\rho R^3 \Phi^2 \bar{c} n^2} \sim \left(\frac{\bar{c}}{R\Phi}\right) \frac{\Lambda}{\Lambda + 2} \cos \beta \sin 2\alpha. \quad (4.3)$$

### 4.3 Results and discussion

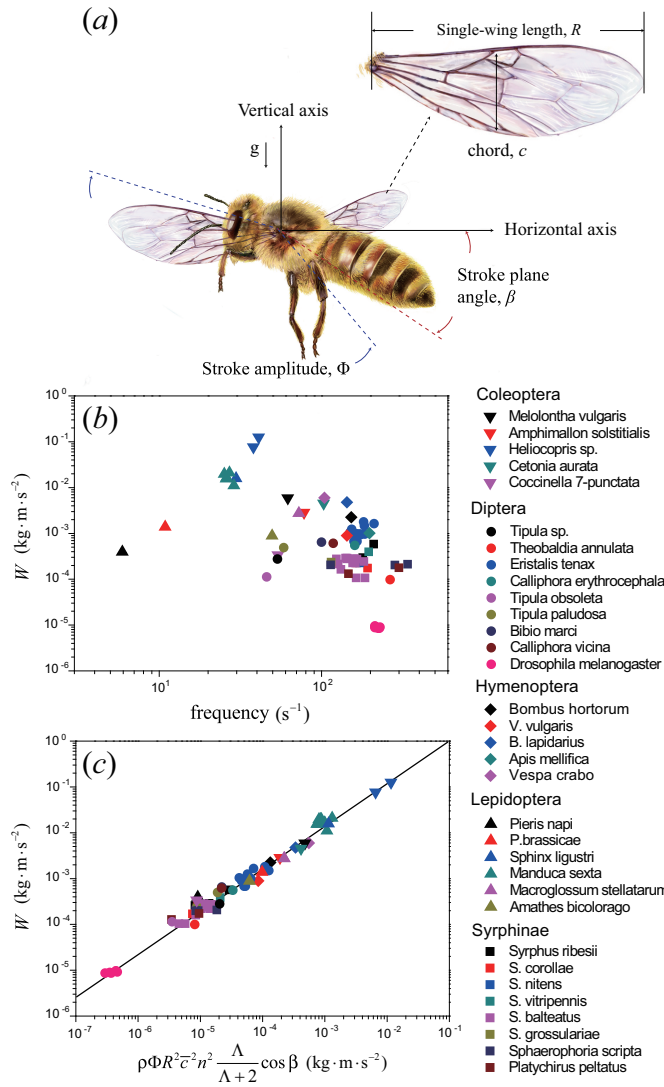


Figure 4.3: (a) Illustration to define morphological and kinematical parameters of hovering insects. Weight of the insect versus (b) frequency, and (c) the scaling parameter  $\rho\Phi R^2 c^2 n^2 \cos\beta$ . We compare our theory with experimental observations (81 data points) for 33 species of hovering insects (Ellington, 1984c,d; Ennos, 1989; Fry *et al.*, 2005; Liu & Sun, 2008; Mou *et al.*, 2011; Walker *et al.*, 2010; Weis-Fogh, 1973; Willmott & Ellington, 1997a,b).

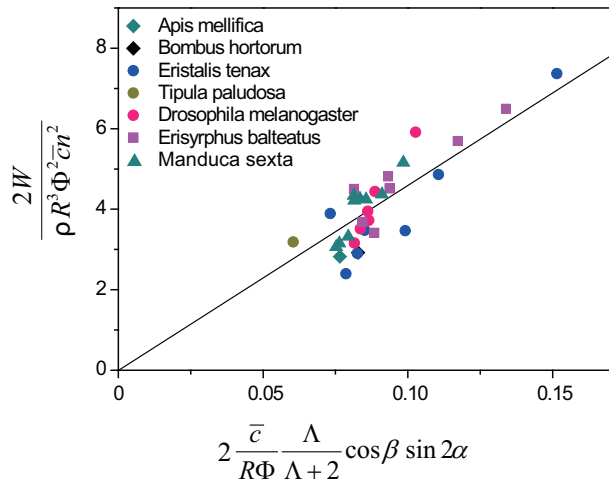


Figure 4.4: Experimental validation of the normalized scaling law (5.6). We compare our theory with experimental observations (32 data points) for six species of hovering insects (Ellington, 1984c,d; Fry *et al.*, 2005; Liu & Sun, 2008; Mou *et al.*, 2011; Walker *et al.*, 2010; Willmott & Ellington, 1997a,b).

We plot the experimental data according to the dimensionless scaling law (5.6) in figure 6.5. The scaling law agrees favourably with the experimental observations with the slope of the best-fitting straight line 46.2.

### 4.3.3 Scaling law based on the conventional steady potential-flow theory

In a conventional theory, the lift and circulation of the leading edge vortex can be written as  $L \sim \rho \Gamma U R$  and  $\Gamma \sim U \bar{c} \Lambda \sin \alpha / (\Lambda + 2)$ , respectively (Dickinson, 1996; Newman, 1977). Since the flapping velocity  $U \sim \Phi R n$ , the scaling law based on the conventional steady potential-flow theory is simply given by

$$\frac{W}{\rho R^3 \Phi^2 \bar{c} n^2} \sim \frac{\Lambda}{\Lambda + 2} \sin \alpha \cos \beta. \quad (4.4)$$

We plot the experimental data according to (5.7) in figure 6.6, where the data are scattered rather than collapsing onto a single master curve as in

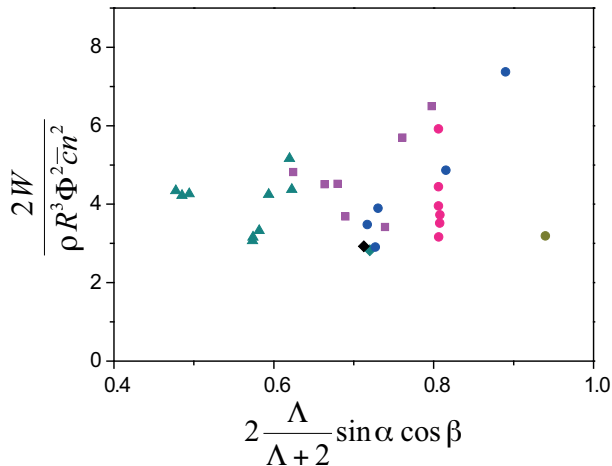


Figure 4.5: The experimentally measured weight of hovering insects plotted according to the scaling law (5.7) based on the conventional steady potential-flow theory. The symbols are from figure 6.5.

figure 6.5. This clearly shows that the conventional theory fails to capture the aerodynamic performance of hovering insects as pointed out by Ellington (1984a,b).

## 4.4 Conclusions

We conclude with a discussion of our results and their implications. Our analysis is distinguished from the conventional steady potential-flow theory in that the lift is scaled as  $L \sim \rho \Gamma \bar{c} R / T$  rather than  $L \sim \rho \Gamma U R$  with  $U \sim \Phi R n$ . It is mainly due to the difference in the vorticity generation process. The steady lift production arises from the formation of trailing vortices at wing tips (freely convecting chordwise vorticity) with its generation rate proportional to the translational velocity  $U$  while the spanwise vortex sheet is bound to the wing surface. As a result, the evolution of the vortical structure around the steady wing can be modelled by a single vortex loop with a monotonically increasing area (Dickinson, 1996; Newman,

1977; Wu *et al.*, 2006). In contrast, on the hovering insect wing, the vorticity is generated all around the edges including the spanwise vorticity at the leading edge (Liu & Aono, 2009; Poelma *et al.*, 2006). We have shown that it is the generation of spanwise vorticity along the wing edges that plays a crucial role in producing lift for hovering insects.

Our theory has been shown to successfully capture the dominant physical mechanism underlying the lift generation in hovering flights, allowing us to obtain a simple scaling law for the lift with given morphological and kinematic parameters of the insects. However, detailed fluid-dynamic phenomena associated with hovering, such as time-dependent flow structures, force history, and interaction with wake, can be adequately accounted for by numerically computing the full Navier-Stokes equation.

We believe that our theory will not only help one to grasp the essential aerodynamics of hovering easily but also shed light on some biological observations that have eluded scientific explanation for decades (Dickinson *et al.*, 1999; Ellington, 1984a). For instance, the wing loads,  $W/(R\bar{c})$ , of the hoverfly *Syrphus balteatus* is  $\sim 8.97$  N/m<sup>2</sup>, which is similar to that of the crane fly *Tipula paludosa* ( $\sim 9.11$  N/m<sup>2</sup>) despite dramatic differences in their wing size and kinematics. The stroke angle of the hoverfly wing ranges only from 60° to 70°, which is almost half of the typical stroke angle of many hovering insects including the crane fly. The wingspan of the hoverfly, about 9.9 mm, is also almost half that of the crane fly. However, the flapping frequency of the hoverfly (124 Hz), which is almost twice higher than that of the crane fly (58 Hz), successfully compensates for such disadvantages because  $W/(R\bar{c})$  is proportional to  $n^2$ , but scales linearly with  $R$  and  $\Phi$ . In other words, hoverflies flap their wings fast just enough to surmount the drawbacks of small stroke angle and wingspan. This provides a clear fluid-dynamic explanation of how different evolutionary selections for wing kinematics and morphology among insect species can arrive at the same functionality: the hovering with similar wing loads. We also expect

## 4.4 Conclusions

---

that our scaling law will be a simple yet powerful guideline for designing flapping-based micro air vehicles.

## Chapter 5

# Experimental study on the fluttering flag-plate interaction

### 5.1 Introduction

Fluttering instability of a flag has been extensively studied in the seminal work of Lord Rayleigh (1878), which shows that the interface between two moving fluids is always unstable. Studies of interface instability have been further elaborated on, taking into account interfacial mass, rigidity, structural damping, and finite dimensions (Argentina & Mahadevan, 2005; Connell & Yue, 2007; Eloy *et al.*, 2008, 2012; Huang & Sung, 2010; Tang & Païdoussis, 2007, 2008) in order to interpret the fluid flow-induced flutter of a flag. The flag in the incoming fluid flow is shown to remain stable until the critical velocity and has a bi-stable nature for a certain range of fluid velocity after the critical velocity (Eloy *et al.*, 2012; Zhang *et al.*, 2000). Several fluttering modes are reported that are classified as stable-state, periodic flutter, and chaotic flutter in terms of dynamic states (Alben & Shelley, 2008; Connell & Yue, 2007; Tang & Païdoussis, 2007; Zhang *et al.*, 2000), and node-less, one-node, imperfect node, and multiple-node flutter in

terms of deformed shapes (Taneda, 1968; Tang & Jiang, 2009; Viro *et al.*, 2013). Transition in such modal behaviours is determined by two non-dimensional parameters: mass ratio,  $\mu = \rho L / \rho_p h$ , and non-dimensional velocity,  $U_R = UL(\rho_p h / D)^{1/2}$ , (Alben & Shelley, 2008; Argentina & Mahadevan, 2005; Tang & Paidoussis, 2007) where  $\rho$  is the fluid density,  $L$  and  $h$  are the length and thickness of the flag, and  $D$  is the flexural rigidity of the flag. The mass ratio implies the mass of the flag relative to that of an interacting fluid, while the non-dimensional velocity is the ratio of the fluid velocity to the bending wave velocity. Furthermore, studies on the interaction dynamics of multiple flags (Farnell *et al.*, 2004; Jia *et al.*, 2007; Kim *et al.*, 2010; Ristroph & Zhang, 2008; Zhang *et al.*, 2000) and flapping dynamics of an inverted flag (Kim *et al.*, 2013) have complemented the existing knowledge on fluttering flags.

Meanwhile, the oscillation of flags has been suggested as an alternative to the conventional wind turbine for harvesting wind energy because of its low price and noise, structural simplicity, abundance, and small size (Akaydin *et al.*, 2010; Allen & Smits, 2001; Bae *et al.*, 2014; Tang & Jiang, 2009). Several mechanisms are employed to convert mechanical energy of the flag to electrical energy such as electromagnetic (Tang & Jiang, 2009), piezoelectric (Akaydin *et al.*, 2010; Allen & Smits, 2001), and triboelectric (Bae *et al.*, 2014) generators. The energy transfer process from wind to the flexible plate has been examined in order to propose a design guideline of a flutter-based wind energy harvester. The energy harvesting efficiency of a piezoelectric flag has been systematically investigated using a fully coupled numerical simulation of fluid-solid-electric systems (Michelin & Doaré, 2013). However, the foregoing studies on fluttering flags have focused on the fundamental problem of fluid-flag interaction in general. The interaction of a flag and the adjacent rigid plate, which has implications for diverse real systems, from the larynx in mammals and the syrinx in birds (Balint & Lucey, 2005; Grotberg & Jensen, 2004) to triboelectric wind en-

ergy harvesters (Bae *et al.*, 2014), has rarely been studied thus far in both dynamics and energy transfer processes.

Here we systematically investigated the dynamics and the energy transfer process of flag flutter adjacent to a plate. We first describe the experimental apparatus and the hydrodynamic modelling used to study the flag flutter adjacent to the plate. We then examine the stability condition and provide a simple scaling law to predict the critical velocity of flag flutter. Next, the dynamics and energy transfer process are examined by varying the inter-space distance. Subsequently, we investigate contact modes of the flag-plate interaction, which enables construction of a regime plot of contact behaviours depending on the mass ratio and non-dimensional velocity. Finally, the reduced frequency and Strouhal number of flag flutter adjacent to the plate are examined to reveal the flag-fluid interaction characteristics by varying the flag length and the incoming velocity.

## 5.2 Materials and methods

### 5.2.1 Experimental apparatus

We conducted wind tunnel experiments to study flag flutter adjacent to the plate. The wind tunnel was designed to drive the wind flow from the top to the bottom. The flag was installed in a hanging configuration, as shown in figure 6.1, to avoid initial deflection possibly caused by its own weight. The wind speed varied from 2.2 m/s to 21 m/s. Flags were cut from polyimide film of 125 and 140  $\mu\text{m}$  thickness, polycarbonate film of 100 and 130  $\mu\text{m}$  thickness, and 80  $\mu\text{m}$  woven fabric (Solueta SILTEX). The length and the width of the flag were varied in the range of  $L = 500 - 1600$  mm and,  $w = 300 - 800$  mm, respectively. The bending stiffness of the flag,  $D = Eh^3/[12(1-\nu^2)]$  with  $E$ ,  $h$  and  $\nu$  being the Young's modulus, thickness of the flag and the Poisson ratio of the flag material, respectively, was varied in the range of  $2.61 \times 10^{-5} - 6.72 \times 10^{-4}$  N·m. The aspect ratio ( $= w/L$ ),

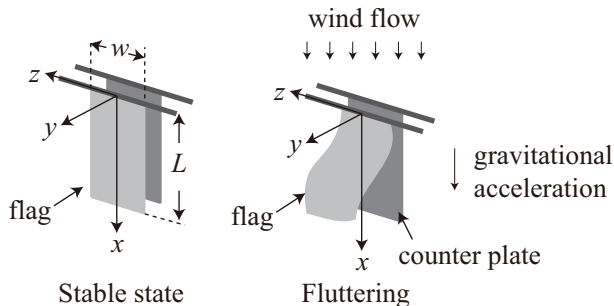


Figure 5.1: Schematic diagrams of the experimental setup.

mass ratio, and non-dimensional velocity ranged from 0.25 to 1, 0.5 to 2.5, and 15 to 150, respectively. A plate having the same dimensions as the flag was installed in parallel with the flag. The critical velocity for flutter was examined by varying the inter-space distance as 1, 1.5, 2, and 2.5 cm. The motion of the flag was captured using a high-speed camera (Photron APX-RS) at 1500 and 3000 frames per second. The contact surface of the plate was covered by polytetrafluoroethylene (PTFE) film that has a higher electron affinity than woven fabric. The instantaneous voltage difference was then induced by contact electrification whenever contact between the woven flag and plate occurred. The voltage signal was measured using an electrometer (Keithley 6514) to detect the contact.

### 5.2.2 Hydrodynamic modelling

The deformation of the flag occurs primarily in the  $xy$ -plane. We assumed the motion of the flag as a two-dimensional plate for simplicity. The fluid flow around the fluttering flag is modelled using the discrete vortex method (Katz & Plotkin, 2001; Tang & Païdoussis, 2007). The section of the flag and the plate is reconstructed by  $N$  number of bound vortex panels based on the displacement data extracted from captured images. The length of each panel is  $\Delta l = L/N$ . The wake structure is supposed to be separated from the trailing edge at each time step with the longitudinal

## 5.2 Materials and methods

---

clearance of  $0.25U\Delta t$  and to travel downstream with a free stream velocity  $U$ , during a time interval  $\Delta t$ . The strength of the vortex panels,  $\gamma_i$ , is determined by a system of algebraic equations, by the flow tangency condition, and by Kelvin's circulation theorem. Enforcing the flow tangency condition on the collocation point,  $(x_{c,i}, y_{c,i})$ , placed at the 3/4 chord of each panel, we obtain the following equations:

$$A_{ij}\gamma_j = \beta_i, \quad (5.1)$$

$$A_{ij} = \frac{(y_{c,i} - y_{v,j}) \sin \alpha_i + (-x_{c,i} + x_{v,j}) \cos \alpha_i}{2\pi[(y_{c,i} - y_{v,j})^2 + (x_{c,i} - x_{v,j})^2]}, \quad (5.2)$$

$$\beta_i = (u_i - U - u_{w,i}) \sin \alpha_i + (v_i - v_{w,i}) \cos \alpha_i, \quad (5.3)$$

where  $(x_{v,i}, y_{v,i})$  is the location of the bound vortex placed at the 1/4 chord of each panel,  $\alpha_i$  is the angle of attack of each panel,  $(u_i, v_i)$  is the  $x$  and  $y$  directional velocity of each panel, and  $(u_{w,i}, v_{w,i})$  is the velocity induced by wake structures. The wake-induced velocity is calculated using the following equation:

$$(u_{w,i}, v_{w,i}) = \sum_j \frac{\gamma_{w,j}}{2\pi} \frac{(y_{c,i} - y_{w,j}, -x_{c,i} - x_{w,j})}{(y_{c,i} - y_{w,j})^2 + (x_{c,i} - x_{w,j})^2}. \quad (5.4)$$

The strength of the newly generated wake structure is determined by Kelvin's circulation theorem, resulting in the following relation:

$$\sum_{i=1}^N \gamma_i^k = \sum_{i=1}^N \gamma_i^{k+1} + \gamma_{w,N}^{k+1}, \quad (5.5)$$

where subscripts  $k$  and  $k+1$  denote the time step, and  $\gamma_{w,N}$  is the strength of the newly generated vortex. Combining equations (5.1) and (5.5), we can determine the strength of the bound and free vortices in the current time step. The pressure difference at each vortex panel,  $\Delta p_i$ , is calculated using the following equation (Katz & Plotkin, 2001; Tang & Paidoussis, 2007).

$$\Delta p_i = \rho[(-u_i + U + u_{w,i}) \cos \alpha_i + (v_i - v_{w,i}) \sin \alpha_i] \frac{N\gamma_i}{L} + \rho \frac{\partial}{\partial t} \sum_{j=1}^i \gamma_j. \quad (5.6)$$

The work done by the fluid can now be calculated as the product of the exerted fluid dynamic force and the velocity of the flag elements.

### 5.2.3 Proper orthogonal decomposition

The modal behaviour of a fluttering flag is analysed using proper orthogonal decomposition (POD) with the displacement data represented in the curvilinear coordinate. The displacement data set is defined as  $\{d_1, d_2, \dots, d_n\}$ , where  $d_i \in \mathbb{R}^m$  and  $n$  and  $m$  are the number of the displacement data and data point in the displacement data, respectively. The orthonormal basis,  $\psi_i \in \mathbb{R}^m$ , can be calculated by the eigenvalue decomposition of matrix  $Y^T Y$ , where  $Y = [d_1, d_2, \dots, d_n] \in \mathbb{R}^{m \times n}$ :

$$Y^T Y q_i = \sigma_i^2 q_i, \quad (5.7)$$

$$\psi_i = (1/\sigma_i) Y q_i, \quad (5.8)$$

where  $\sigma_i^2$  and  $q_i$  are the non-zero eigenvalue and eigenvector of  $Y^T Y$ , respectively. The orthonormal bases satisfy the following expression (Berkooz *et al.*, 1993):

$$\sum_{j=1}^n \|d_j - \sum_{i=1}^l (d_j^T \psi_i) \psi_i\|^2 \rightarrow \text{minimize}, \quad (5.9)$$

where  $l$  is the number of orthonormal bases. The energy fraction captured by each mode can be calculated as following:

$$\text{Energy fraction of mode } i = \sigma_i^2 / \sum_{j=1}^l \sigma_j^2. \quad (5.10)$$

## 5.3 Results and discussion

### 5.3.1 Stability condition

We first examined the critical velocity of the flag placed adjacent to the rigid plate by varying flag materials, dimensions, and inter-space distances. The rigid plate has negligible influence on the critical condition in the ranges of the parameters studied in this work. When the flag remains stable in the incoming flow, boundary layers on the plate are a dominant source to distort

### 5.3 Results and discussion

---

the uniform incoming flow. The boundary layer thickness of the plate,  $\delta$ , reaches at most about 1/5 of the inter-space distance according to the calculation based on the laminar boundary layer theory,  $\delta \sim 5.0L/\text{Re}_L^{1/2}$ . Therefore, it is reasonable that the stability condition remains unchanged. Hysteresis is observed for the critical condition as shown in figure 6.2(a); the flag flutter continues far below the critical velocity, once flutter occurs.

The scaling law describing the critical velocity of flag flutter,  $U_c$ , is constructed based on the assumption that the flutter occurs when the work done by the fluid flow excites the critical bending energy for flag flutter. The work done by the fluid flow can be expressed as a product of the area,  $Lw$ , displacement  $A$ , and the pressure difference across the flag,  $\Delta p$ . The pressure difference is scaled with the classical airfoil theory, represented by,  $\Delta p \sim \rho U^2 A/L$  (Argentina & Mahadevan, 2005; Katz & Plotkin, 2001). The bending energy of the flag is scaled as  $\int_0^L Dw\kappa^2 dL \sim Dw(A/L^2)^2 L \sim DwA^2/L^3$ . Balancing the work done by the fluid and bending energy of the flag, we can obtain the following scaling relation for the critical velocity as:

$$U_c \sim \left(\frac{D}{\rho L^3}\right)^{1/2}. \quad (5.11)$$

To validate our scaling law (5.11), we compared the critical velocity measured by experiments performed with our scaling law as shown in figure 6.2(b). The stability conditions are compared in the two-dimensional plot of mass ratio,  $\mu$ , and the non-dimensional velocity to mass ratio,  $U_R/\mu$ , in figure 6.2(c) with the stability conditions reported in previous publications (Argentina & Mahadevan, 2005; Berkooz *et al.*, 1993; Katz & Plotkin, 2001; Tang & Païdoussis, 2007; Yamaguchi *et al.*, 2000a,b) for achieving the following two merits: first, it directly reflects the relation between the critical velocity and the flag length when the physical properties of the flags are given (Tang & Païdoussis, 2007). Second, it shows the transition of modal behaviours, which appears as a sudden jump in the stability boundary around the mass ratio of 1.2.

### 5.3 Results and discussion

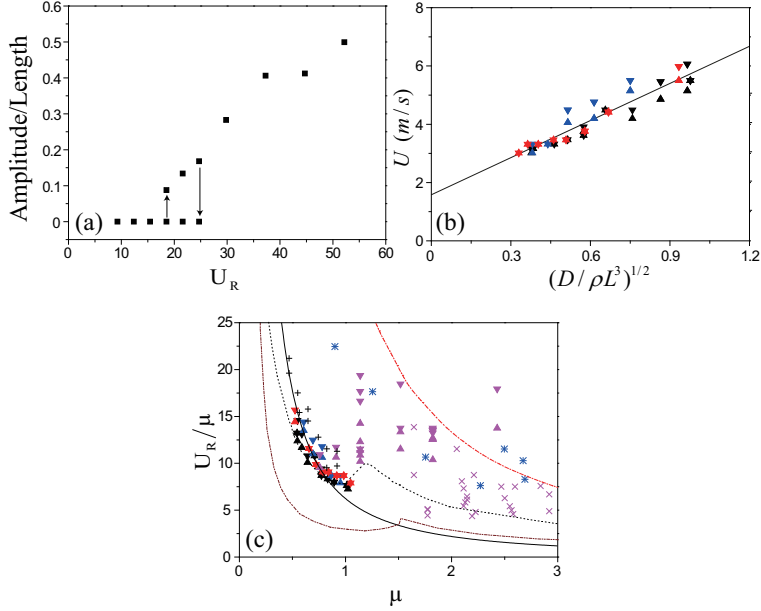


Figure 5.2: (a) Ratio of flapping amplitude and flag length,  $A/L$  versus non-dimensional velocity  $U_R$  for the  $[L, w] = [7.5, 5]$  cm sized of woven flag. (b) Plot of critical velocity for flag flutter according to the scaling law (5.11). (c) Plot of critical conditions for flag flutter depending on the mass ratio,  $\mu$  and the non-dimensional velocity to mass ratio,  $U_R/\mu$ : solid line, present scaling law; dashed line, theory of Tang & Paidoussis (2007); dash-dot line, theory of Argentina & Mahadevan (2005); dash-dot-dot line, theory of Yamaguchi *et al.* (2000b); cross, experimental data of Huang (1995); x-marker, experimental data of Yamaguchi *et al.* (2000a); asterisk, experimental data of Watanabe *et al.* (2002). In here, black, red, blue, and magenta triangles correspond to flags made from polyimide with  $140 \mu\text{m}$  thickness, polycarbonate with  $130 \mu\text{m}$  and  $100 \mu\text{m}$  thickness and woven fabric of  $80 \mu\text{m}$  thickness, respectively.

## 5.3 Results and discussion

---

Before the bending mode transition, the critical velocity is shown to increase linearly with  $D/(\rho L^3)$  as shown in figure 6.2(b and c), consistent with the prediction of the scaling law (5.11). However, once the bending mode transition occurs, the stability condition cannot be predicted by linear stability analysis (Argentina & Mahadevan, 2005; Tang & Païdoussis, 2007; Yamaguchi *et al.*, 2000b) or our scaling law as shown in figure 6.2(c). Moreover, the stability conditions show a certain amount of discrepancies between experimental data published in previous studies [28-31] and experimental data found in this study. This may be caused by the increasing influence of non-linear effects (Eloy *et al.*, 2008; Tang & Païdoussis, 2007) and planeity defects (Eloy *et al.*, 2012), which inevitably arise with a difference in magnitude in each of the experimental conditions. While there is some extent of discrepancy between the stability boundaries suggested by previous studies and our scaling law, all the stability boundaries predict similar trends close to the experimental observations.

### 5.3.2 Dynamics and energy transfer process

Sequences of fluttering motions are examined, as shown in figure 6.3, by setting the inter-space distance as infinity, which corresponds to the single flag flutter, 2.5 cm and 1.5 cm at a fixed wind velocity of 5.2 m/s. In contrast to the stability condition, the fluttering motion adjacent to the plate is disturbed even without contact with the decrease in fluttering frequency, as shown in figure 6.3(b). The fluttering amplitude of the plate side is almost identical to the amplitude of the single flag flutter, whereas the opposite maximum amplitude decreases, resulting in breaking of symmetry. As the plate is placed closer to the flag, the contact occurs with the edge of the flag as shown in figure 6.3(c).

We next investigated the modal behaviour and energy transfer process of the single flag flutter near the critical condition in comparison with the flag-plate interaction. The fluttering motion is symmetric in the centre

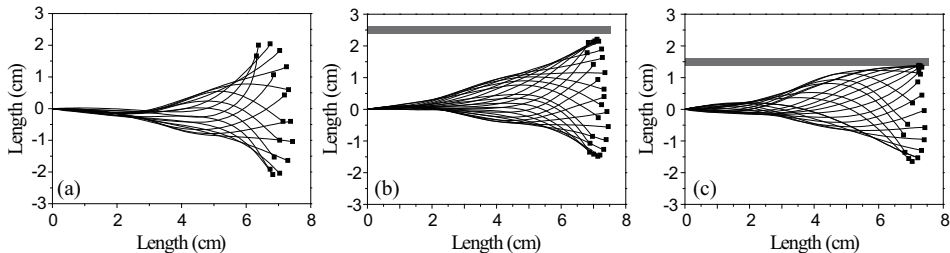


Figure 5.3: Sequential images of fluttering motions for  $[L, w] = [7.55]$  cm-sized woven flags at a wind velocity of 5.2 m/s. In here, inter-space distances are (a) infinity (b) 2.5 cm (c) 1.5 cm.

while it follows a figure-of-eight trajectory at the edge as shown in figure 6.4(a), implying a periodic oscillation. First to third orthonormal bending modes, captured by the POD, are shown in figure 6.4(b). Most of the energy of the fluttering flag ( $\sim 99.4\%$ ) is captured in the first two bending modes as shown in figure 6.4(c). The energy transfer process is analysed by the discrete vortex method using the displacement data measured by the high speed camera. The energy is transferred from the fluid to the flag along the middle part of the flag ( $\sim 25\text{-}80\%$  of the flag from the pin-point), whereas the mechanical energy of the flag is extracted to the fluid at the end part ( $\sim 80\text{-}100\%$ ).

Power delivered to the lengthwise flag element versus the dimensionless length of the flag is shown in figure 6.4(d-f). The energy transfer process can be characterized as having three distinct stages; energy absorption, transition and energy release, which correspond to the figure 6.4(d-f), respectively. The energy absorption occurs when the flag edge is reversed and the middle part of the flag approaches the maximum displacement, as shown in figure 6.4(d), because of the strong positive work along the middle part of the flag. During this process, the magnitude of the energy extracted from the end part of the flag is much smaller than the energy transferred to the middle part. Subsequently, the power input along the middle part

### 5.3 Results and discussion

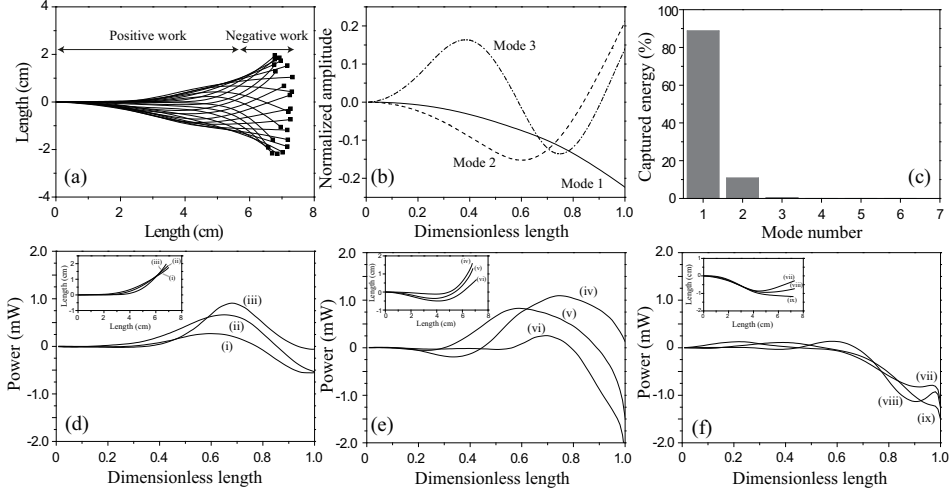


Figure 5.4: Analysis on dynamics and energy transfer for  $[L, w] = [7.5, 5]$  cm sized of woven flag at wind velocity of 4.9 m/s. (a) Sequential images of fluttering motion. (b) First-to-third mode shapes obtained by proper orthogonal decomposition. (c) Energy captured by bending modes. (d-e) Plots of power delivered from the fluid flow to the lengthwise flag element versus the dimensionless length. In here, the inset shows the posture of the flag when corresponding time.

is attenuated gradually, whereas the energy release from the end part develops rapidly as the middle part decelerates and the end part accelerates as shown in figure 6.4(e) - a transition from energy absorption to energy release. Negative power along the end part of the flag is maintained while the middle part is reversing and the end part is decelerating as shown in figure 6.4(f), which results in the release of energy to the fluid flow.

The overall energy transfer process of the flag flutter adjacent to the plate is similar to that of the single flag flutter; energy absorption, transition and energy release occur subsequently for each half cycle of oscillation as shown in figures 6.5 and 6.6. Energy is pumped into the flag by the positive work along the middle part as shown in figures 6.5(a, d) and 6.6(a, d), whereas the energy is released by the negative work at the end part

### 5.3 Results and discussion

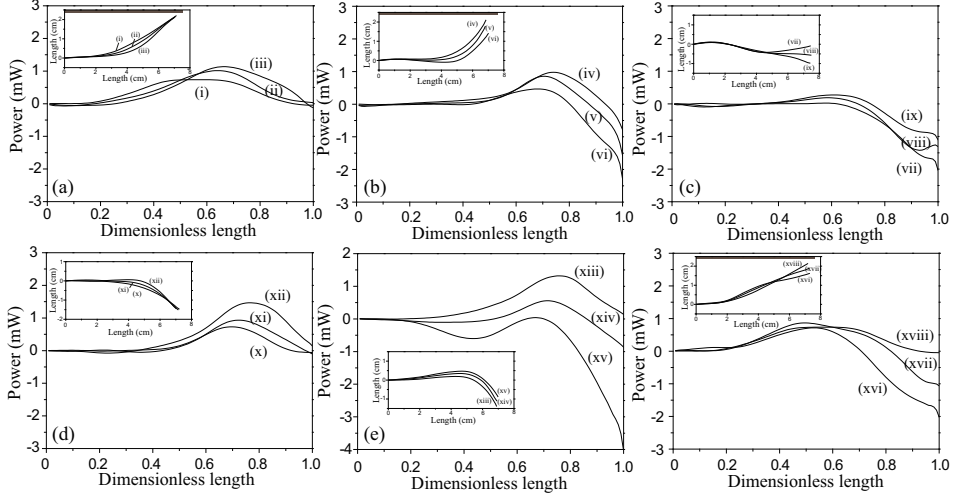


Figure 5.5: Energy transfer process of flag flutter adjacent to the plate. Here,  $[L, w] = [7.55]$  cm,  $U = 5.2$  m/s and inter-space distance is 2.5 cm. (a-f) Plots of power delivered from the fluid flow to the lengthwise element versus the dimensionless length. Here, the inset shows the posture of the flag when corresponding time.

as shown in figures 6.5(c, f) and 6.6(c, f). However, asymmetry in energy transfer process occurs because of the influence of the plate. When the flag approaches the plate, the energy transfer rate is magnified as shown in figures 6.5(e-f) and 6.6(e-f). When the flag approaches the plate, the fluid velocity between the plate and flag should be higher to satisfy mass conservation due to the channel-closing effect. Then, the pressure difference across the flag also becomes higher, resulting in the increase of the aerodynamic force and power input. The effect of the plate becomes prominent when the plate is placed closer to the flag as shown in higher power of figure 6.6(e-f).

## 5.3 Results and discussion

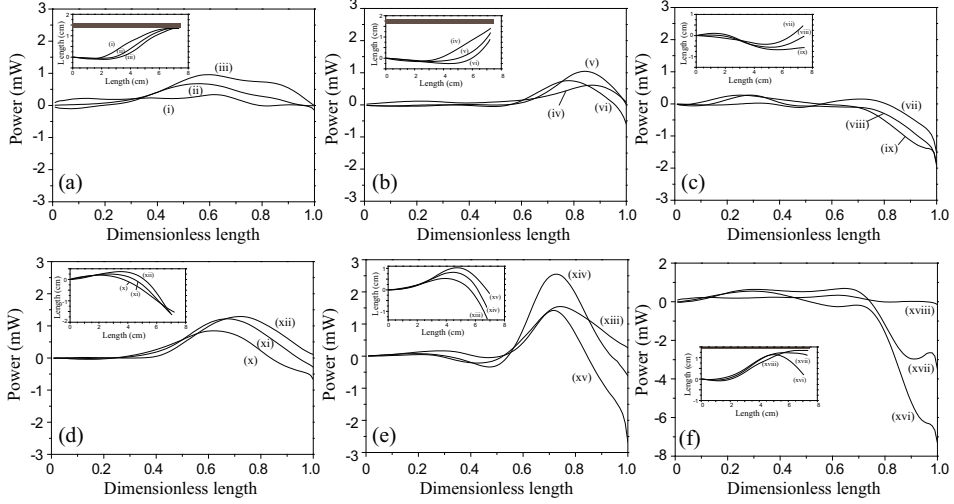


Figure 5.6: Energy transfer process of flag flutter adjacent to the plate. Here,  $[L, w] = [7.55]$  cm,  $U = 5.2$  m/s and inter-space distance is 1s.5 cm. (a-f) Plots of power delivered from the fluid flow to the lengthwise element versus the dimensionless length. Here, the inset shows the posture of the flag when corresponding time.

### 5.3.3 Flag-plate contact modes

We next investigated the flag-plate contact dynamics systematically by varying the wind speed and the flag length. Contact is detected by measuring the voltage signal induced by the contact electrification. Contact frequency calculated by the FFT analysis of voltage measurement data corresponds to the frequency calculated from the fluttering images. The increase in wind speed promotes transition in dynamic modes from stable-state to periodic flutter and subsequent chaotic flutter as shown in figure 5.7. When the wind speed moderately increases above the critical velocity, flutter arises in a periodic manner with a definite contact frequency as shown in figure 5.7(a, d and g). The fluttering behaviour is asymmetrical to the centreline owing to the contact between the flag and the plate. By further increasing the wind speed, the motion of the flag becomes irregu-

### 5.3 Results and discussion

---

lar and unpredictable as shown in figure 5.7(j), which corresponds to the chaotic flutter. The transition to the chaotic mode results in the excitation of a wide range of contact frequency, rather than apparent dominant frequency as shown in figure 5.7(k). Chaotic behaviour is limited to the end part of the flag around the transition condition, while irregular behaviour spreads to the entire flag length as velocity increases far above the critical condition.

In addition, the modal behaviour of the fluttering flag and the resulting contact modes are changed by the variation of the flag length. For a relatively short flag flutter, the contact occurs once at the very edge of the flag under the dominant influence of the first two bending modes as shown in figure 5.7(c). Then, the single peak curve is observed in the voltage signal as shown in the inset of figure 5.7(b). As the flag length increases, higher bending modes become excited as shown in figure 5.7(c, f, i and l), and then, the first contact is highly likely to occur at the middle part of the flag. For the moderately long flag, double contact behaviour -comprising two instantaneous contacts at the middle and edge of the flag - is observed with the excitation of third bending mode as shown in figure 5.7(d, f). Then, the voltage shows two distinct peaks corresponding to the double contacts as shown in the inset of figure 5.7(e). By additionally increasing the flag length, contact-propagation behaviour, rather than instantaneous contact, is observed. The contact point propagates along the plate with the traveling wave as shown in figure 5.7(g), with the excitation of the third and fourth bending modes as shown in figure 5.7(i). In this situation, the frequency calculated from the FFT analysis does not show apparent dominant frequency because of the prolonged first contact, as shown in figure 5.7(h), while the fluttering motion seems to be periodic.

The regime plot of flag-plate interaction modes is constructed in figure 5.8(a) and depends on the mass ratio,  $\mu$  and the non-dimensional velocity to mass ratio,  $U_R/\mu$ . The regime plot has two transition boundaries on the

### 5.3 Results and discussion

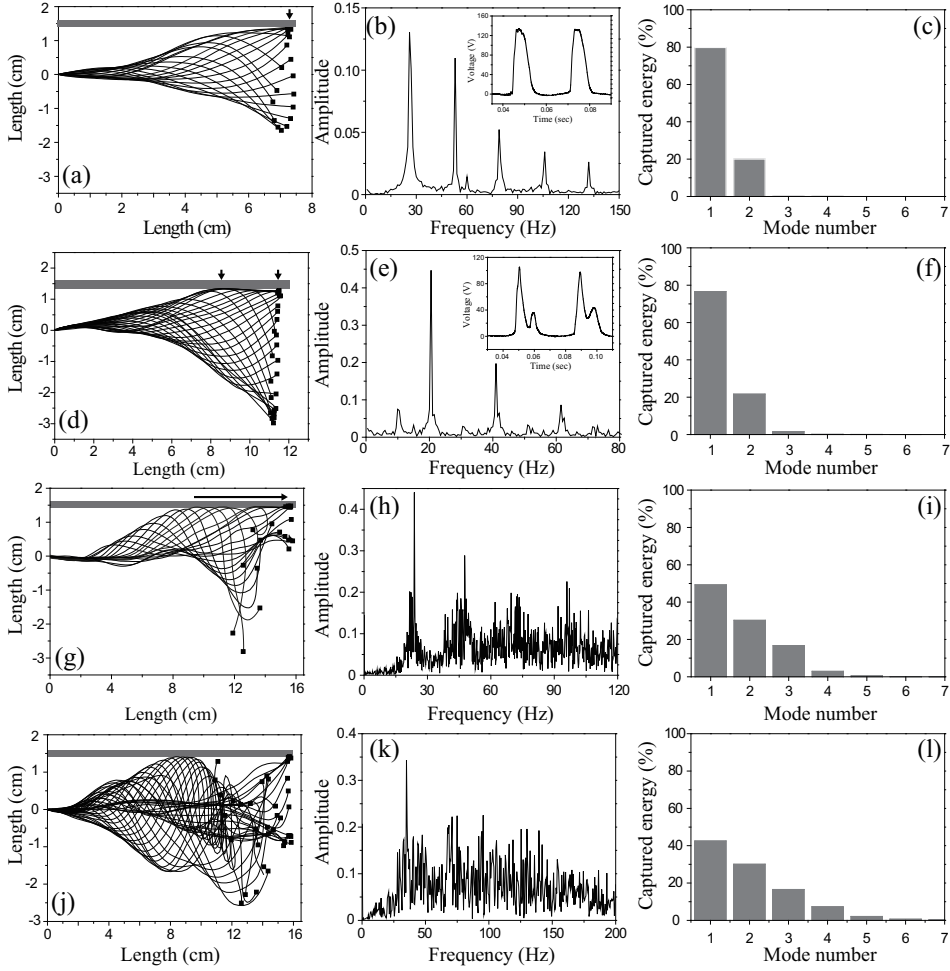


Figure 5.7: Sequential images of fluttering motion (a, d, g, j), contact frequency calculated from the FFT analysis (b, e, h, k), energy fraction captured by each bending modes (c, f, i, l). (a-c)  $[L, w] = [7.5, 5]$  cm sized woven flag at a wind velocity of 5.2 m/s. (d-f)  $[L, w] = [12, 3]$  cm sized woven flag at a wind velocity of 5.2 m/s. (g-i)  $[L, w] = [16, 8]$  cm sized woven flag at a wind velocity of 7.3 m/s. (j-l)  $[L, w] = [16, 8]$  cm sized woven flag at a wind velocity of 10.8 m/s.

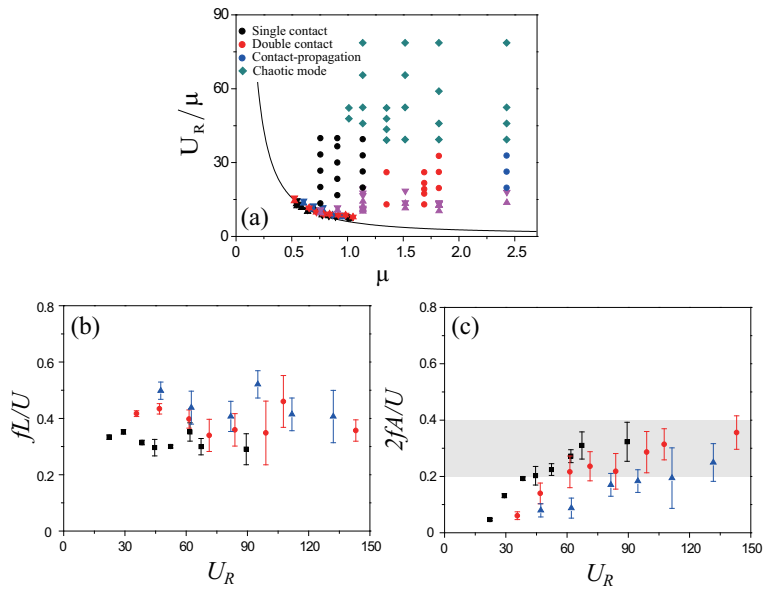


Figure 5.8: (a) Regime plot of contact modes (b, c) Reduced frequency and Strouhal number of flag flutter adjacent to the rigid plate as functions of non-dimensional velocity, where rectangles, circles, and triangles correspond to the 7.5, 12, and 16 cm length of flag, respectively.

### 5.3 Results and discussion

---

dynamic states: critical condition for flutter, above which periodic oscillation arises, and transition to chaotic mode. When the flag-plate contact occurs in a periodic manner, contact behaviours can be classified as single contact, double contact or contact-propagation. Increase in the mass ratio leads to transitions of contact behaviours. Transition from the single to double contact mode corresponds to the transition of modal behaviour of the single flag flutter around a mass ratio of 1.2 (Viro *et al.*, 2013). In the chaotic mode, the contact behaviour cannot be defined as a characteristic motion due to the irregularity.

We further examined the variation of two non-dimensional parameters - reduced frequency and Strouhal number, which describe the interaction characteristics of fluid flow and flag flutter - by increasing the non-dimensional velocity as shown in figure 5.8(b, c). Reduced frequency is the ratio of the time-scale of fluid flow passing through the flag ( $= L/U$ ) to the period of oscillation ( $= 1/f$ ). The reduced frequencies of three different flags are confined in the narrow range of 0.3 to 0.6 as shown in figure 5.8(b). These results correspond to the previous observations on the single flag flutter which show the adjustment of reduced frequencies at similar values (Viro *et al.*, 2013), implying that the interaction characteristics of fluid and flag flutter are dominated by the inherent properties of the fluttering flag rather than the contact. The Strouhal number is the ratio of the velocity of the flag edge ( $= 2Af$ ) and the wind speed ( $= U$ ), which describes the interaction dynamics of an object moving in the fluid and wake generated by the motion of the object (Williamson, 1996). The Strouhal number monotonically increases with the non-dimensional velocity and converges around 0.3 when the non-dimensional velocity is approximately 60, regardless of flag dimensions. This value corresponds to the optimal Strouhal number that maximizes the efficiency of flapping foils and animals moving in the fluid (Taylor *et al.*, 2003), implying that the fluttering flag self-optimizes

the amplitude and the frequency adapting to the incoming flow in high wind.

## 5.4 Conclusions

In this study, we have investigated the dynamics and energy transfer process of flag flutter adjacent to the rigid plate. The influence of the plate is negligible when the flag does not flutter below the critical velocity, whereas the presence of the plate brings about asymmetry in the dynamics and energy transfer process even without contact when the flutter begins. The flapping amplitude of the plate side is almost unchanged, whereas the opposite maximum amplitude decreases. The transmitted power from the fluid to the flag increases as the inter-space distance between the flag and plate decreases. We further studied the contact behaviours by varying the flag length and the wind velocity. The contact modes are changed from stable-state to periodic contact and subsequently to chaotic contact, by increasing the wind speed. When the contact occurs in a periodic manner, the contact characteristics can be classified as single contact, double contact, and contact propagation, wherein the transition occurs by increasing the flag length. The reduced frequency of the flag flutter adjacent to the plate corresponds to that of single flag flutter. Furthermore, the Strouhal number is shown to correspond to the optimal condition that maximizes the efficiency, revealing the self-optimization of fluttering flag in high wind. These results confirm that the dynamics of the fluttering flag adjacent to the plate are influenced by the inherent flag-fluid interaction characteristics rather than the contact between the flag and the plate.

## Chapter 6

# Flutter-driven triboelectrification for harvesting wind energy

We note that the study in this chapter was a result of collaborative research with Samsung Advanced Institute of Technology. The contents of this chapter appeared in the publication, Bae *et al.* (2014). To clarify the overall flow of this study, here we report the whole contents of the publication (Bae *et al.*, 2014). The experiments associated with the electrical performance of the device were conducted with Jihyun Bae and the manuscript was written with Jihyun Bae, Jong-Jin Park and Ho-Young Kim.

### 6.1 Introduction

As the needs for the portable and wireless electronics have been growing rapidly, the energy harvesting technology has been highlighted as a promising solution to supply the electrical power without wiring to external sources. Thus far, diverse environmental energy sources have been exploited for the energy harvesting, such as mechanical vibration, light,

heat and electromagnetic radiation. Among possible environmental energy sources, wind energy can be an ideal source for energy harvesting system due to its absolute abundance (Knight, 2004; Lee *et al.*, 2013b; Traber & Kemfert, 2011) and has long been actively developed since the invention of the windmill. Recently, flow-induced vibration of flexible structures has been suggested as an alternative to overcome the drawbacks of wind-turbine based wind energy generator including structural complexity, the large volume and weight, high cost of manufacturing and installation, low efficiency and noise. Most research in this area focused on piezoelectric materials (Doaré & Michelin, 2011; Fei *et al.*, 2012; Peng & Chen, 2012; Zhang *et al.*, 2012) such as Lead zirconium titanate (PZT) and Polyvinylidene fluoride (PVDF), where a deformation of piezoelectric material gives rise to electrical energy. The recently invented triboelectric generator harvests mechanical energy through a periodic contact motion based on the coupling of the triboelectric and electrostatic effects, and many approaches have been carried out to improve the electrical output performance of the triboelectric generator (Cheng *et al.*, 2013; Lin *et al.*, 2013; McCarty & Whitesides, 2008; Niu *et al.*, 2013; Wang *et al.*, 2012a,b; Yang *et al.*, 2013a; Zhang *et al.*, 2000, 2013). A triboelectric generator is one of the most promising energy conversion systems due to its low cost, simple fabrication routes, and the possibility of high power density (Xie *et al.*, 2013; Yang *et al.*, 2013b).

Meanwhile, there has been considerable research on the basic dynamics of flexible structures like flags, which can be bent, folded, twisted, or waved in the air (Argentina & Mahadevan, 2005; Bao *et al.*, 2010; Huang & Sung, 2010; Liu *et al.*, 2001; Pang *et al.*, 2001; Schouveile & Eloy, 2009; Shelley & Zhang, 2011; Zhu *et al.*, 2014). The first experimental study on fluttering behavior was performed by Taneda (1968) with a flag made of various fabrics and shapes, to find a variety of flapping modes (e.g. nodeless, one-node, imperfect-node, and two-node flutters). In addition, using one dimensional

filaments, the distinct dynamic states (e.g. a stretched-straight state and a flapping state) and the coupled interaction between the states were observed through a flowing soap film experiment (Tian *et al.*, 2011). On the other hand, the interaction of the flag and a counter rigid plate hitherto has received scant attention, although their coupled dynamics can be a very powerful vibration source for triboelectric generator due to its self-sustained nature.

In the present work, we first investigate the interaction dynamics of a flexible flag textile and a solid plate to obtain the stability boundaries of fluttering. We show that the dynamic behaviors can be classified into three distinct regimes of single contact, double contact and chaotic contact. We then develop a FTEG, with the configuration of a flag and a counter plate arranged in parallel with respect to the air stream, based on the knowledge of the interaction dynamics of the flag and plate. As a result, the instantaneous output voltage, current and power of 7.5 cm  $\times$  5 cm size FTEG reaches 250 V, 70  $\mu$ A, and 17.5 mW, respectively, at the incoming flow velocity of 22 m/s. In addition, the frequency of the electronic peak is extremely high (about 115 Hz) compared to the previously suggested energy harvesting devices Zhang *et al.* (2013), which ensures the overwhelming electrical performance of the current FTEG. The 7.5 cm  $\times$  5 cm size FTEG with a dual plate configuration at the incoming air velocity of 15 m/s can fully charge a 100  $\mu$ F capacitor within 4 minutes. In ambient open environment, we demonstrate that the FTEG can be easily developed for the large-scale energy harvesting system as well, with an extremely simple fabrication process, very low cost and weight.

## 6.2 Materials and methods

### 6.2.1 Experimental set-up for characterization

In the typical wind tunnel system, a specific holder was attached to install the flutter-driven triboelectric generator (FTEG). The prepared flexible electrode and the triboelectric active plate with top and bottom electrodes were placed on the holder with 1-cm separation in accordance with the coupled interaction experiment between the flag and the plate. Both the top and bottom electrodes were connected to the electrometer (Keithley 6514) to measure the electrical performances including the open-circuit voltage, short-circuit current and capacitor-charging time. The fluttering behaviour of the flag was characterized by capturing the bending motions using a high-speed camera (Photon APX-PS) at a frame rate of 1,500 Hz.

### 6.2.2 Fabrication of a FTEG

The triboelectric active material was chosen for maximizing the contact electrification effect and fluttering behavior. A conductive, highly flexible, Au-coated woven structure (Solueta Co. Ltd. SILTEX, CNG type) was employed as a flag-type electrode. A PTFE film (3M) with adhesive on one side is chosen as a triboelectric layer with high electron affinity and acts as a counter surface for making contact with the fluttering flag. For the rigid counter plate, the same textile electrode was placed on the substrate and the PTFE film was attached to the top of the electrode as shown in figure 6.1a-iii. The micro-structured woven surface (fig. 6.1a-i) and the texturized surface on the PTFE film (fig. 6.1a-ii) aid in enhancing the friction area without additional complex surface fabrication steps.

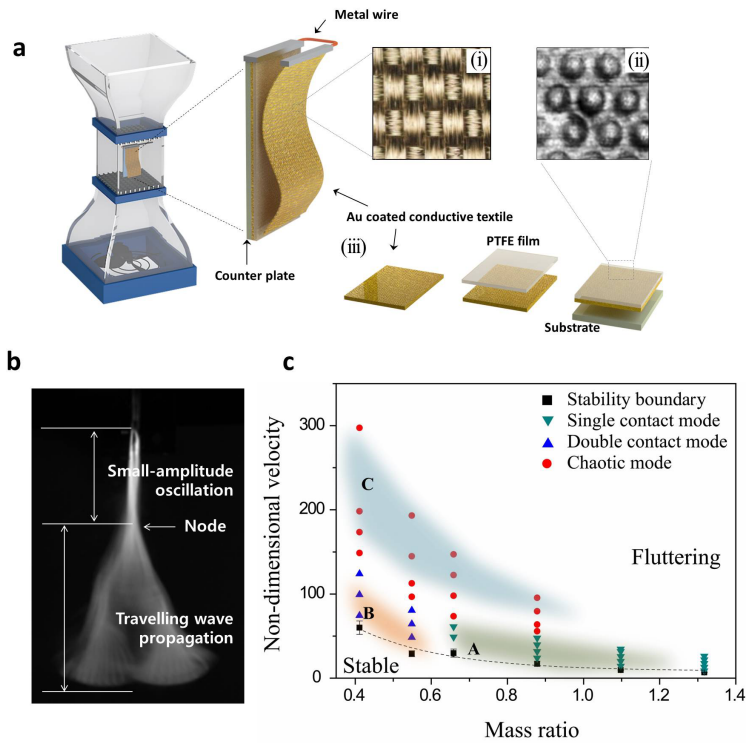


Figure 6.1: Experimental set-up and characterization of fluttering behavior. (a) Schematic diagram of a wind tunnel and the structural design of a FTEG including surface characteristics of (i) a highly flexible flag and (ii) a counter plate, and (iii) the fabrication of the counter plate. (b) Fluttering images of a stand-alone configuration of dimensions  $7.5 \text{ cm} \times 5 \text{ cm}$  as captured with a high speed camera. (c) The regime map of the dynamic interaction between a flag and a plate.

## 6.3 Results

### 6.3.1 Flutter-driven Triboelectric generator (FTEG) set-up

For the construction of the simplest wind-driven energy harvesting system using fluttering behavior, a flexible flag and a rigid plate were arranged in face to face as shown in figure 6.1 so that the interaction between them can lead to a rapid periodic contact and separation. The flexible flag with a metal coated on the surface acts as the fluttering body as well as an electrode. Polytetrafluoroethylene (PTFE), a triboelectric material of high electron affinity, was attached to the surface of the rigid plate in order to achieve contact electrification between conductor and dielectric. The two structures become oppositely charged whenever they are in contact. The subsequent separation of the two charged structures induces an electronic potential difference that can induce the flow of free electrons to an external circuit. This simple mechanism can be successfully employed for converting the kinetic energy of the wind to electrical energy.

### 6.3.2 Analysis of fluttering behavior

To optimize an electrical output from the contact-separation behavior of the flag and rigid plate, it is important to understand the detailed dynamic characteristics of flutters. As shown in figure 6.1b, a flexible Au-coated woven flag exhibited oscillations with a node. From the top to the node, where the fluttering amplitude is nearly zero, only a very small amplitude oscillation arises. Below the node, a traveling wave propagated toward the trailing edge with increasing amplitude.

In order to induce a self-sustained contact-propagation-separation of conductor and dielectric through the high frequency oscillation of flag flutter, we simply placed the counter plate next to the flag flutter within a critical distance. We then systematically examined the coupled interaction between the flag and the plate by varying the dimensions of the structures

(width  $w$  and length  $L$ ), bending stiffness of the flag  $B$ , flag-plate distance  $d$ , and incoming velocity  $U$ .

The onset velocity for flutter is largely dependent on the bending stiffness, incoming air velocity, and the length of the flag. However, the flag-plate distance had a negligible effect on the stability of the flag. Hysteresis was observed for the flutter onset velocity. The fluttering of the flag suddenly arises above a certain critical velocity. However, once fluttering occurs, it continues despite the decrease of air velocity far below the critical value. Bistability was observed between the two critical velocities, where a small external excitation can induce the transition from the stable to fluttering state.

The stability boundary can be characterized in a 2-dimensional space of dimensionless parameter as shown in figure 6.1c: the non-dimensional velocity,  $U\sqrt{\rho w L^3/B}$ , and the dimensionless mass of the flag,  $m_L/(\rho w L)$ , where  $m_L$  is the mass per unit length of the flag and  $\rho$  is the fluid density. The non-dimensional velocity is the ratio of the kinetic energy of incoming flow to the elastic energy of the flag. The dimensionless mass is the mass of the flag relative to that of an interacting fluid. Flags with larger dimensionless mass are prone to fluttering at a lower non-dimensional velocity due to the destabilizing effects of inertia. In general, by raising the incoming velocity above the stability boundary, the flexible flag begins to flutter in a periodic manner.

In the fluttering region in figure 6.1c, we observed two distinct contact-separation modes. The transition from the single contact mode in region A (fig. 6.1c) to the double contact mode in region B (Fig 1c) occurs as the dimensionless mass decreases, which can be tuned by adjusting the length of the flag. This is because of the transition in bending mode of fluttering flag. As the flag length decreases, the second bending mode is excited, and contact is then likely to occur only at the trailing edge of the flag,

resulting in the single contact mode. As the flag length increases, double-contact behavior, composed of one contact in the middle of the flag and a second contact at the end of the flag, arises easily because the third bending mode is excited. The transition between the single and double contact mode appears when the dimensionless mass ranges from 0.55 to 0.66. This corresponds to the previously reported condition of bending mode transition of single paper flutter (Tang & Jiang, 2009; Virost *et al.*, 2013). Furthermore, most flutter experiments have reported that the bending mode transition arises when the dimensionless mass of the flag is in the range of 0.4 to 0.8 (Eloy *et al.*, 2012; Tang & Païdoussis, 2007).

Figure 6.2 shows sequential images of the contact-propagation-separation behaviors for the single and double contact modes with different flag lengths at a fixed flag-plate separation of 10 mm, captured using a high speed camera (Photron APX-RS) at the frame rate of 1500 Hz. In the single contact mode for flag dimensions of 7.5 cm  $\times$  5 cm, the oscillating flag collides with the counter surface with a high kinetic energy due to the large swing amplitude at the edge (fig. 2a-i). The contact surface then increases and decreases again gradually following the travelling wave (fig. 6.2a-ii-iv). The flag then moves away from the counter plate (fig. 2a-v). The flag finally reaches the maximum amplitude (fig. 2a-vi) and repeats the cycle. In addition, considering the force at the moment of impact between the fluttering flag and the counter surface, the oscillating motion in the single contact mode is similar to that of a flail with a free-swinging stick or a double pendulum. This motion effectively transforms the angular momentum of the oscillating flag into impact.

On the other hand, in the double contact mode for flag dimension of 12 cm  $\times$  3 cm, after the first contact occurs (fig. 2b-i), the traveling wave propagates (fig. 2b-ii), which leads to a propagation of the contact area along the wave direction (fig. 2b-iii). A second-contact then arises later towards the trailing edge of the flag (fig. 2a-iv), but with a smaller contact

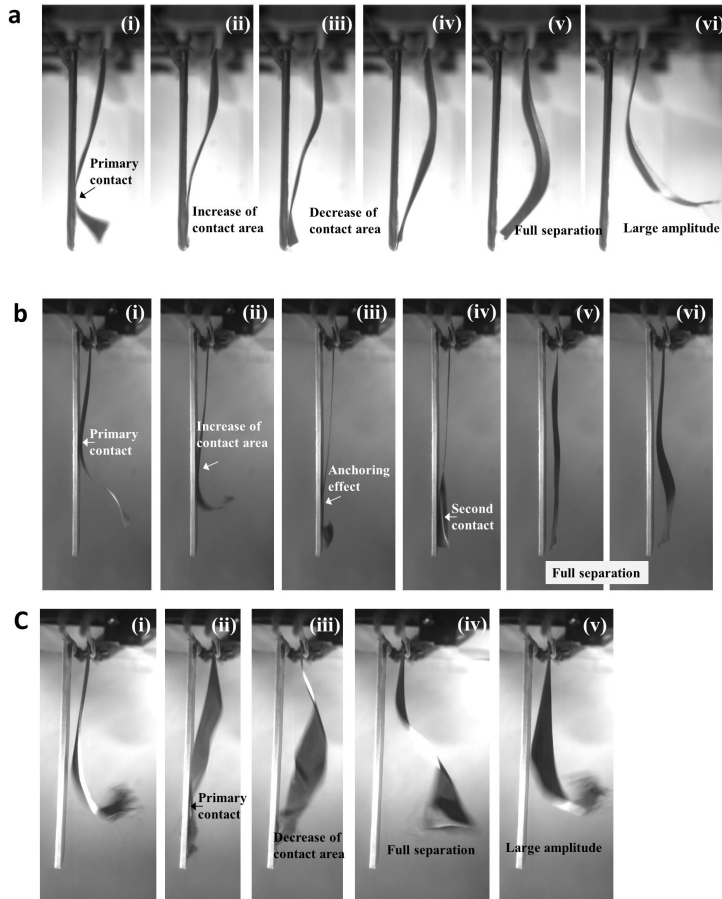


Figure 6.2: Sequential images of contact-separation behavior. (a) Single contact mode: fluttering behavior of a flexible structure with dimensions  $7.5 \text{ cm} \times 5 \text{ cm}$ . For (b) double contact mode and (c) chaotic modes, fluttering behavior of a flexible structure with dimensions  $12 \text{ cm} (L) \times 3 \text{ cm} (W)$  was captured by a high speed camera under a flow velocity of  $9.2 \text{ m/s}$ .

strength than the initial contact due to the anchoring effect of the previously contacting surface. The flag then moves away from the counter plate (fig. 2a-v-vi). Another transition can be observed between periodic (regions A and B) and chaotic flutter (region C, fig. 6.1c). The chaotic mode shown in figure 6.2c occurs above a critical non-dimensional velocity that is a function of the mass ratio. The chaotic transition boundary can be approximated as  $U\sqrt{\rho w L^3/B} \approx 41.73m_L/(\rho w L)^{-1.29}$ . The fluttering motion loses its regularity and becomes random and chaotic. Flutter occurs in a circular or spanwise direction so that the contact area changes very irregularly.

### 6.3.3 Working principle

The electricity generation process in a FTEG is based on the contact-propagation-separation motion induced by a flutter. It causes gradual increase and decrease of the total contact area via wave propagation, resulting in an electrical signal distinct from what is obtained by a pushing or sliding mode of triboelectric generator. Previous study was shown that the sliding mode is more effective than the pushing mode in terms of the electric signal generation because of the sequential increase in the area at the surface for sliding, which enhances friction (Yang *et al.*, 2013a,b; Zhu *et al.*, 2013a). From this point of view, electricity generation from a FTEG would be strongly distinguished on the change in effective contact area due to the fluttering behavior. As shown in figure 6.1a, the configuration of a FTEG is based on the metal-polymer structure. Under no external flow, all the charge on the inner contact surface will be generated with the opposite polarity to that generated at the contact. This occurs due to the strong electrostatic attraction to the tribo-charged surface, which in turn ensures good contact between the PTFE film and the Au-coated flag. When the flag is blown by the wind, the flag moves backward and forward, following pendulum motion, and there is no electrical charge difference until the moment contact is made. Right after contact, wave propagation occurs,

which leads to a gradual increase and decrease in the contact surface and, results in inducing charge separation on the surface. The separated charges on the surface raise the potential on the Au-coated flag and induce a current flow to an external load to the electrode on the PTFE. While the flag periodically approaches the plate, an electrical potential difference between the electrode on the PTFE and the Au-coated flag will occur at a higher potential. A reverse current flow will then drive the system toward electrostatic equilibrium. In general, after the flag contacts the plate, the contact area gradually increases before separation. In addition, this motion drives a higher potential on the PTFE electrode and will contribute to a current flow from the electrode to the Au-coated flag.

### 6.3.4 Electrical characterization of FTEG

Voltage and current measurements were carried out under a flow velocity of 7.5 m/s for the single and double contact modes at a total device size of around 7.5 cm  $\times$  5 cm and 12 cm  $\times$  3 cm, respectively. In the single contact-separation mode, transferred charges produced an alternating-current output with a short circuit current ( $I_{sc}$ ) of 25  $\mu$ A, an open circuit voltage ( $V_{oc}$ ) of 140 V (fig. 6.3a and 6.3b), and a consecutive contact area of 2 cm  $\times$  5 cm. Based on the enlarged profiles of the electrical signal and the fluttering images, the flag-plate interaction consisted of the following steps: a primary contact of the curved area (fig. 6.3c-i and 6.3d-i), an increase in contact area (fig. 6.3c-ii and 6.3d-ii), a decrease in contact area (fig. 6.3c-iii and 6.3d-iii), and eventual separation. These steps are clearly reflected in  $I_{sc}$  and  $V_{oc}$ . A gradual increase in contact area after primary contact appears as associated with the distinctive increase in  $I_{sc}$  and  $V_{oc}$ . A decrease in contact area then appears at separation, which is also evident from the  $V_{oc}$  profile.

For the double contact mode, the two peaks per cycle in  $I_{sc}$  and  $V_{oc}$  are shown in figure 6.3g and 6.3f, which are the results of additional con-

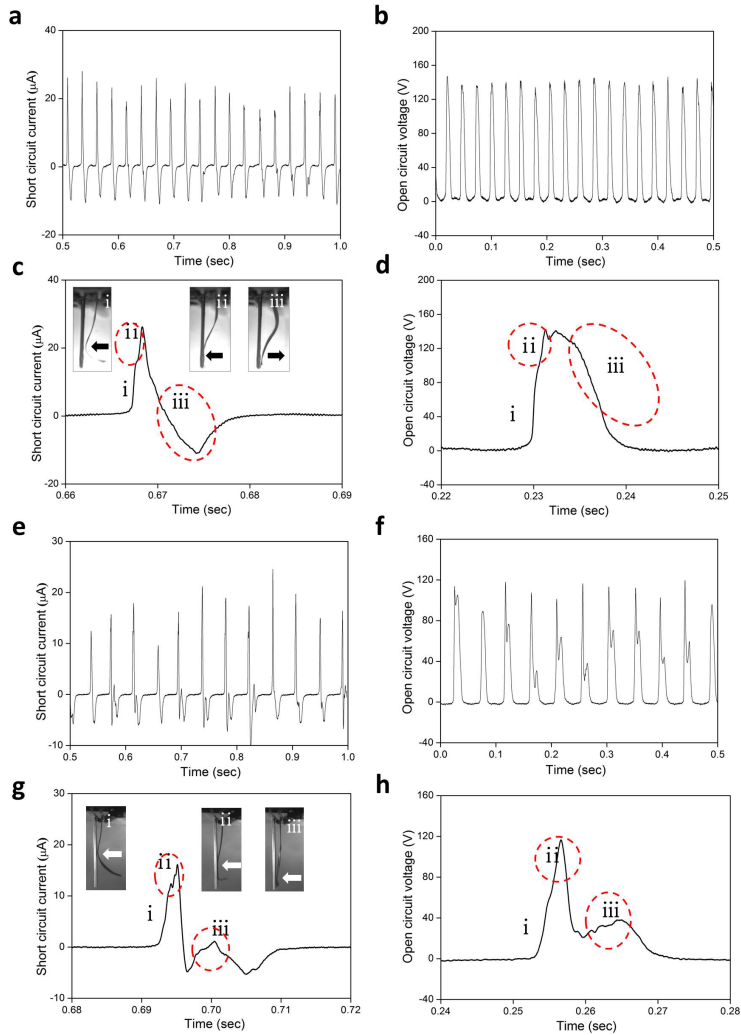


Figure 6.3: Analysis of the electrical signal for each mode. (a-d) Electrical signal of the FTEG under a flow velocity of 7.5 m/s with dimensions 7.5 cm  $\times$  5 cm. (a) Short circuit current. (b) Open circuit voltage. (c) Peak in the profile of short circuit current. (d) Peak in the open circuit voltage. (e-h) Electrical signal of the FTEG under a flow velocity of 7.5 m/s with dimensions 12 cm  $\times$  3 cm. (e) Short circuit current. (f) Open circuit voltage. (g) Peak in the short circuit current. (h) Peak in the open circuit voltage.

tact at the end of the flexible flag. The fluttering behavior drives primary contact (fig. 6.3g-i and 6.3h-i), the propagation with an increase in contact area (fig. 6.3g-ii and 6.3h-ii), the second contact at the edge of the flexible structure (fig. 6.3g-iii and 6.3h-iii), and eventual separation. From the enlarged profile of  $V_{oc}$  and  $I_{sc}$ , the sequential increase in contact area and the second peak from the edge contact clearly induce distinct electrical signals compared with the single contact mode. The subsequent change in the contact area due to the travelling wave propagation in fluttering effectively enhances triboelectrification or induces an additional contact mode depending on the flag dimensions. Such propagation is a novel characteristic of a FTEG using a flexible flag. Unlike other types of triboelectric generator, electricity generation in a FTEG is dependent on the polarization magnitude due to the effective contact area and the rate of triboelectric charge separation. In this respect, understanding flutter-induced contact behavior for different structure dimensions and flow velocities is critical.

### 6.3.5 Performance of a FTEG as a function of flow velocity

To investigate the relationship between electric output and fluttering behavior of a flexible flag as a function of flow velocity, a systematic measurement was performed under flow velocities varying from 7.5 m/s to 22 m/s. As shown in Figure 4a, the maximum peak of  $V_{oc}$  in the single contact mode increases with increasing flow velocity and dramatically jumps to the maximum value of 240 V at 22 m/s. This result can be explained from a change in surface contact area in the fluttering motion with an increase of flow velocity efficiently. At higher wind speeds, a higher fluttering speed results which increases the contact force. Since both the PTFE surface and the woven flexible electrode have a regular micro-pattern on the surface shown in Figure 1a, a larger applied force will enhance the micro-scale contact area between them, resulting in a higher surface charge density (Fan *et al.*, 2012; Zhu *et al.*, 2013b). As the flow velocity increases, the fluttering

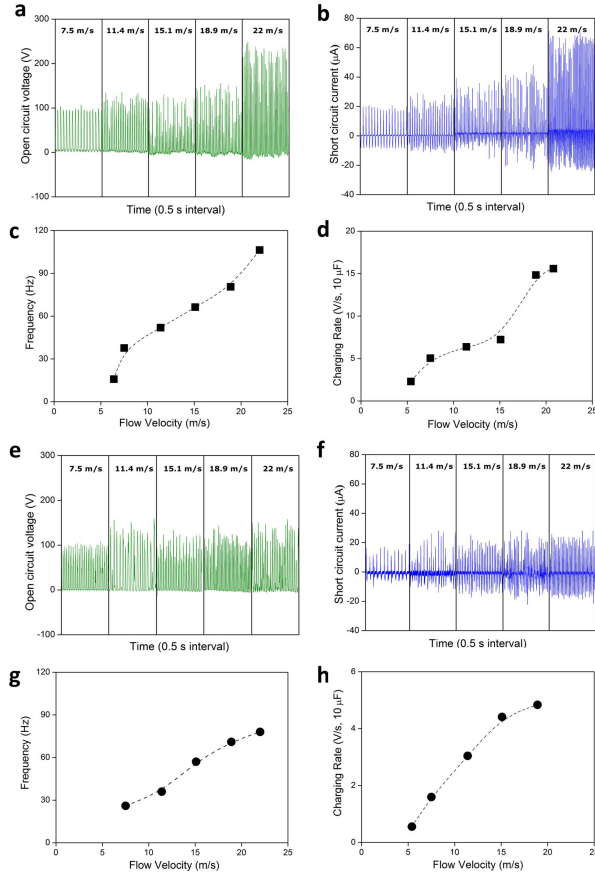


Figure 6.4: Influence of flow velocity on electrical output. (a-d) Electrical output performance of a FTEG with a single contact configuration. (a) Open circuit voltage, (b) short circuit current, (c) frequency of electrical output for single contact mode, and (d) charging rate for a  $10 \mu\text{F}$  capacitor with flow velocities from 7.5 m/s to 22 m/s. (e-h) Electrical output performance of the FTEG with a double contact configuration. (e) Open circuit voltage, (f) short circuit current, (g) frequency of electrical output for double contact mode, and (h) charging rate for a  $10 \mu\text{F}$  capacitor with flow velocities from 7.5 m/s to 22 m/s.

motion becomes chaotic and an irregular spanwise directional bending of the flutter motion can also be observed, which can increase the effective contact-propagation region unpredictably. This implies that the coupling between flow velocity and fluttering motion may result in an increase of  $V_{oc}$  at higher flow velocity. As shown in figure 6.4b, the peak of  $I_{sc}$  increases with increasing wind speed. This occurs because a higher wind speed results in both more transferred charge as discussed before and a higher charge transfer rate with an increase of contact frequency as shown in Figure 4c. The averaged output current density and power density with variable flow velocities were investigated with a charging rate of a 10  $\mu\text{F}$  capacitor. As shown in Figure 6.4d, in the single contact mode, the charging rate of a 10  $\mu\text{F}$  capacitor increased with flow velocity.

In contrast, in the double contact mode  $V_{oc}$  and  $I_{sc}$  only slightly increase with flow velocity (fig. 6.4e and f). Such an effect is because the effective contact area in double contact mode tends to decrease with increasing flow velocity due to chaotic behavior, resulting in only a slight increase in electrical output. Although  $V_{oc}$  and  $I_{sc}$  in double contact mode are less dependent on flow velocity, the frequency of  $V_{oc}$  directly depends on the flow velocity. The charging rate of a 10  $\mu\text{F}$  capacitor increased with increasing flow velocity as shown in figure 6.4g and 6.4h. This implies that the frequency of the electrical output plays a dominant role in enhancing the power density of a triboelectric generator system.

### 6.3.6 Durability and Efficiency

In the FTEG system, the durability of the device will depend on that of the flag material because of the cyclic impact motion. We tested an electrical performance during prolonged fluttering. Prior to the test, the selvage of the flag was sealed with an adhesive to prevent threads from coming loose. The average electrical performance was evaluated by monitoring the time it took to charge a 1000  $\mu\text{F}$  capacitor to 30 V in every charging cycle.

The results indicated that the charging time did not change significantly even after a continuous 12 million flutter while slight damage to the flag around the bottom edge was observed. In addition, a flag contaminated intentionally with dust was employed for the charging test to confirm the reliability in harsh open environments. The charging time with the dust-contaminated flag increased, but after seven charging cycles (about 15 min), the charging time recovered significantly to reach 110 % of the charging time of the dust-free flag. We suppose that the high frequency of the oscillating flag would prevent the flag from becoming contaminated by environmental dust as well as acting to remove dust. The efficiency of the FTEG can be defined as the ratio of the electric energy generated by a single plate FTEG to the mechanical energy of the flag. The mechanical energy of the flag can be calculated from the images captured by a high-speed camera at the instant of contact; flag dimensions of  $7.5 \text{ cm} \times 5 \text{ cm}$  and a  $7.1 \text{ m/s}$  flow velocity result in a mechanical energy of  $0.018 \text{ mJ}$  per cycle. The induced electrical energy under the same conditions is  $0.0018 \text{ mJ}$  at a load of  $2 \text{ M}\Omega$ . The energy conversion efficiency is thus calculated to be 10 %.

### 6.3.7 Application of multiple arrays of FTEGs

Using a simple dual plate design with dimensions  $7.5 \text{ cm} \times 5 \text{ cm}$  at a  $15 \text{ m/s}$  flow velocity, the electrical signals were obtained as shown in figure 6.5(a) and (b). The frequency of the electrical output reached  $158 \text{ Hz}$ , and increased up to  $50 \mu\text{A}$  and  $200 \text{ V}$ , respectively. The improved frequency and electrical output characteristics imply a larger average system power density, which can be combined with an energy storage system such as capacitors or batteries. For this purpose, the charging time of a  $100 \text{ F}$  capacitor to  $10 \text{ V}$  was compared with different configurations of a single plate (A), a dual plate (B), and a parallel connection of two dual plate with circuit A (C) and circuit B (D) as shown in figure 6.5c. We see that the charging time decreases from  $174 \text{ s}$  to  $73 \text{ s}$  when a dual plate

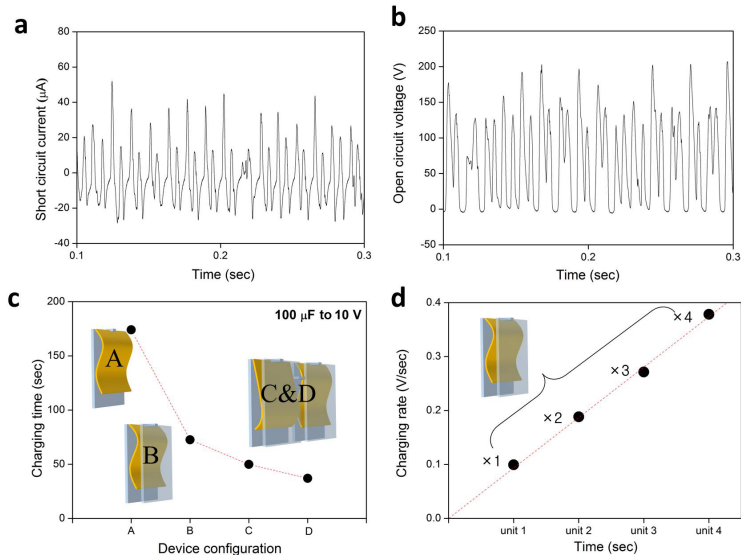


Figure 6.5: Electrical output performance of the dual plate configuration for a FTEG with dimensions  $7.5 \text{ cm} \times 5 \text{ cm}$  at a flow velocity of  $15 \text{ m/s}$  and charging performance for different configurations. (a) Short circuit current for a dual plate configuration. (b) Open circuit voltage of a dual plate configuration. (c) Charging time of a  $100 \mu\text{F}$  capacitor to  $10 \text{ V}$  with a single plate, a dual plate, and a parallel connection between two dual units. (d) The charging rate increasing with the number of units connected side-by-side and in 2 by 2 arrays.

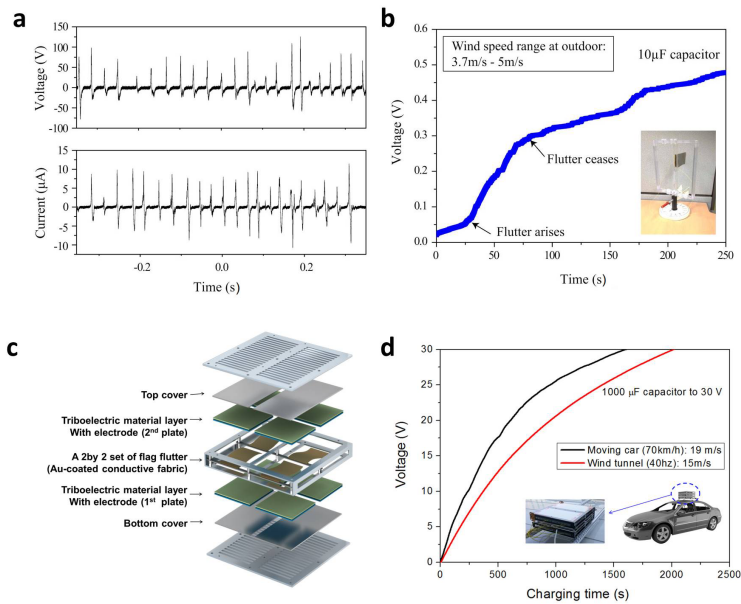


Figure 6.6: The demonstrations for an open environment. Electrical output performance of the rotatable FTEG. (a) Open circuit voltage. (b) Short circuit current. (c) Charging time of a 10  $\mu\text{F}$  capacitor to 0.5 V by charging with the rotatable FTEG (inset: image of the rotatable FTEG). (d) Schematic of the FTEG packaging module. (e) Comparison of the charging time between charging in the open environment and wind tunnel system.

configuration is used. In the parallel connection, the charging time can be further reduced from 50 s to 37 s by adopting different circuit designs that connect the rectifier to each unit. Figure 6.5d shows that the charging rate increases linearly with the number of units arranged side by side.

### 6.3.8 Demonstration in an open environment

To demonstrate the performance of an FTEG in an ambient environment, we prepared two types of setups, as explained in the following. First, we incorporated an FTEG into a weathercock so that the system can work under the wind of any direction. We observed the fluttering behavior of

the rotatable FTEG and investigated its electrical performance by charging a 10 F capacitor to 0.5 V with a maximum open circuit voltage of 100 V (fig. 6.6a) and short circuit current of 12.5  $\mu\text{A}$  (fig. 6.6b) at an ambient wind velocity of around 3.7 - 5 m/s (3 BF in Beaufort wind force scale). In response to an arbitrary natural wind direction, the rotatable FTEG repositioned itself so that it was parallel to the wind direction. The charging time of the capacitor in an open environment is shown in figure 6.6c, and various natural wind speeds result in different charging slopes. Second, a solid, robust of FTEG packaging module was also designed as shown in figure 6.6d, which enables the FTEG to be securely mounted on the roof of a moving vehicle. Figure 6.6e shows the electrical performance of charging a 1000  $\mu\text{F}$  capacitor to 30 V with the FTEG attached to a car moving at a speed of 70 km/h (19 m/s) in comparison with the charging performance within the wind tunnel at 15 m/s wind speed. A charging time of 25 min is obtained when the car is travelling at 70 km/h. These demonstrations confirmed that the FTEG can operate in an open environment under a variety of wind conditions.

## 6.4 Discussion

We have shown that fluttering behavior can be effectively employed to induce a contact-propagation-separation of a flexible flag and a rigid plate for triboelectrification. The regimes of dynamic interactions including single contact, double contact, and chaotic modes, were identified in a regime map for different flag lengths and flow velocities. Each contact mode resulted in a distinct frequency and amplitude for the electrical output. The single contact mode exhibited large electrical outputs and high fluttering frequency. With increasing flow velocity, electric performance was enhanced linearly. In a FTEG, the average power density depended on contact force, effective contact area, and a type of contact motion including a stable periodic contact and chaotic contact, in addition to the frequency

of the electrical output. We demonstrated a self-sustained FTEG with a maximum voltage of 250 V and current of 70  $\mu\text{A}$  at a flow velocity of 22 m/s. With a dual plate FTEG design, the frequency of the electrical performance reached 158 Hz at a flow velocity of 15 m/s. This work introduced a new route for triboelectric energy harvesting by utilizing the well-known phenomenon of a fluttering flag, which is a self-sustained motion with extremely high frequency. This FTEG shows excellent electrical performance with a very simple configuration and has the potential for implementation over large areas at low cost. This system can improve electronic performance without size and shape limitations.

# Chapter 7

## Conclusions

In the present research, we have conducted the fluid dynamic study of the flapping foils for bio locomotion and the fluttering flags adjacent to the rigid plate for wind energy harvesting. The scaling laws are constructed for the force produced by the flapping foils by considering the momentum imparted to the vortical structures generated by the foil motion. The novel concept of the wind generator based on the contact electrification of the fluttering flag and the plate have been suggested.

The fluid dynamics of an angularly reciprocating plate has been examined first as an elementary model of the flapping locomotion, especially for the simulation of the sprinting from stationary condition. The flow fields around the angularly reciprocating plate are visualized by the PIV techniques, which reveals that the two distinct vortical structures are generated each half cycle. The first vortical structure is generated when the tail accelerates, while the second vortical structure is generated when the tail decelerates and reverses. The scaling law considering the momentum imparted to the vortical structures is in good agreement with the experiments.

The wake and thrust of an angularly reciprocating plate has been studied further by varying the tail shapes and aspect ratio over two order of magnitudes. The thrust of the angularly reciprocating tail is maximized at

---

the aspect ratio around 0.7, where the mechanism of the force production transits from the added mass force to momentum imparted to the vortical structures. The efficiency is continuously increases with the aspect ratio, whereas the increasing rate of the efficiency is abruptly changed by the transition of the force production mechanism around the aspect ratio 0.7. Based on our experiments, we can interpret the hydrodynamic principle of the caudal fin shape of small aquatic animals that the low aspect ratio of them provides advantage in thrust in given kinematic conditions as an expense of the efficiency.

Next, the interaction dynamics of the fluttering flag and the adjacent rigid plate has been studied. There is no change in the stability condition when the plate is placed adjacent to the flag compared to the flag alone case. However, the asymmetry is observed for the flag adjacent to the rigid plate even without contact when the flutter begins. Four distinct contact modes are observed by varying the incoming wind velocity and flag length. When the flag length is relatively short, the first contact at the edge of the flag is observed by the dominant influence of the first two bending modes. As the flag length increases, the higher bending modes are excited resulting the change in modal behavior from single contact to double contact and contact propagation. In addition, the fluttering modes changed subsequently from the stable state to periodic contact and chaotic contact as wind velocity increases. The modal behavior is illustrated in the two dimensional regime plot of non dimensional velocity and the mass ratio.

The novel concept of the wind generator has been developed on the basis of the fluid dynamic study of the fluttering flags, which exploits triboelectric effect of the flag and the plate. The electric performance of the flutter driven triboelectric generator (FTEG) is examined systematically by varying the flag length and the wind velocity. This FTEG shows excellent electrical performance with a very simple configuration and has the potential for implementation over large areas at low cost.

# Appendix A

## Comparison of the scaling law with high- $St$ computational results

Dong *et al.* (2006) numerically computed the thrust coefficient  $C_T$  of foils flapping at high  $St$ , which varies as 0.6, 0.8, 1.0 and 1.2. At these high  $St$ , the incident flow angle is quite large near stroke reversals despite a relatively low angle of attack during linear translation ( $30^\circ$  at mid-line), which is expected to generate flow fields similar to the ones observed in this work. We convert their results as the following to compare with our scaling law, (2.9). The expression for  $C_T$  can be rearranged to be related to  $\langle F_t \rangle / (\rho h^4 f^2)$  as

$$\langle C_T \rangle = \frac{\langle F_t \rangle}{0.5\rho U^2 S} = \frac{2}{\pi} \frac{\langle F_t \rangle}{\rho h^4 f^2} \left( \frac{2Af}{\hat{U}} \right)^2 \left( \frac{h}{A} \right)^2 \frac{h}{w}, \quad (\text{A.1})$$

where  $S$  is the foil area and  $A$  is the heave amplitude of the foil oscillation.

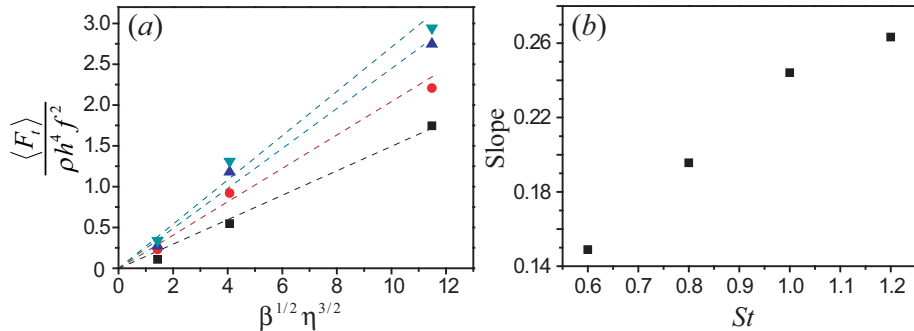


Figure A.1: (a) Computational results of Dong et al. (2006) plotted according to the scaling law (2.9). The squares, circles, upright triangles and upside-down triangles correspond to  $St = 0.6, 0.8, 1.0$  and  $1.2$ , respectively. (b) The slope of best-fitting straight lines of (a) as a function of  $St$ .

Hence, the scaled thrust is written as

$$\frac{\langle F_t \rangle}{\rho h^4 f^2} = \frac{\pi}{2} \langle C_T \rangle \left( \frac{\hat{U}}{2Af} \right)^2 \left( \frac{A}{h} \right)^2 \frac{w}{h}. \quad (\text{A.2})$$

Table A.1 lists the values taken from Dong et al. and the derived quantities,  $\beta$ ,  $\eta$ , and  $\langle F_t \rangle / (\rho h^4 f^2)$ . We note that  $A/h$  was held constant at 0.5 in Dong et al. Plotting the data according to the scaling law (2.9), the scaled thrust indeed increases linearly with  $\beta^{1/2} \eta^{3/2}$  at each  $St$  as shown in figure A.1(a). The slope of the straight line increases with  $St$  as shown in figure A.1(b). The difference of the slopes found in Dong et al. and the value predicted in our work, 3.3, is attributed to the small pitch-bias angle as well as the small  $St$  employed in Dong et al. Although further work is necessary to fully confirm the consistency of these computational results and our scaling law (for example, the effects of  $Re$ , angle of attack, pitch-bias angle, and nondimensional stroke amplitude need to be investigated), the present comparison supports our scaling law favourably.

---

Dong <i>et al.</i> (2006)			Converted data		
$St$	$C_T$	$AR$	$\beta$	$\eta$	$\langle F_t \rangle / (\rho h^4 f^2)$
0.6	0.1	1.27	1	1.27	0.109
0.6	0.25	2.55	1	2.55	0.546
0.6	0.4	5.09	1	5.09	1.744
0.8	0.375	1.27	1	1.27	0.230
0.8	0.75	2.55	1	2.55	0.921
0.8	0.9	5.09	1	5.09	2.208
1.0	0.7	1.27	1	1.27	0.274
1.0	1.5	2.55	1	2.55	1.180
1.0	1.75	5.09	1	5.09	2.747
1.2	1.25	1.27	1	1.27	0.340
1.2	2.4	2.55	1	2.55	1.311
1.2	2.7	5.09	1	5.09	2.943

Table A.1: Raw data of Dong *et al.* (2006) and their converted values. Here  $St = 2Af/U$  and  $AR$  is the aspect ratio.

## Appendix B

# Influence of the chordwise vortices on the thrust of an angularly reciprocating plate

In previous chapters 2-3, we have constructed the scaling law for the thrust of an angularly reciprocating plate on the basis of the observations of the 2-dimensional flow fields around the flapping plate. However, in 3-dimensional airfoil theory, the trailing vortices separated from the wing tip induces the downward velocity resulting in the decrease of effective angle of attack and the occurrence of the induced drag. Therefore, the effects of the chordwise vortices are still unclear for the angular reciprocation within the 2-dimensional flow observations. The measurement of the 3-dimensional vortical structures should be complemented to examine the influence of the chordwise vortices on the thrust of an angularly reciprocating plate.

The measurement results of the 3-dimensional flow structures of moving plate which conducts the similar motion to the flapping plate investigated in the present study can be found in figure 2.4 and 3.5 (therein) in Kim

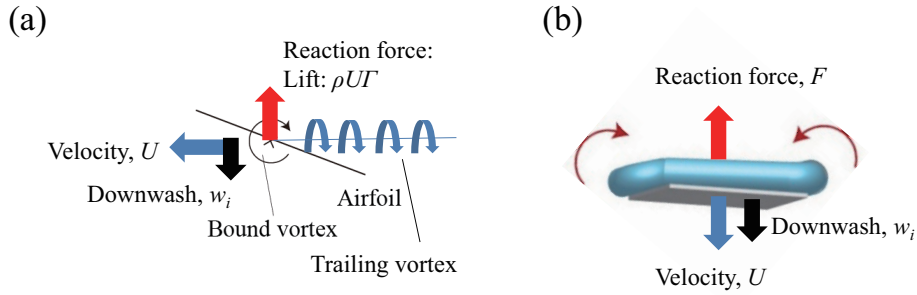


Figure B.1: Schematic illustrations of the vortical structure of (a) lift-based locomotion (b) drag-based locomotion

(2010). In that results, in contrast to the 3-dimensional vortical structure around the conventional airfoil, the separated chordwise vortices did not convected to downstream along the free-stream. The separated chordwise vortices are connected to the tip vortex forming the vortex loop around the tail edges corresponding to the our scaling law based on the vortex loop model. Moreover, the velocity induced by the chordwise vortices is parallel to the direction of the motion, whereas the downwash induced by the chordwise vortices is normal to the direction of the motion in the lift production of 3-dimensional airfoil as schematically illustrated in figure B.1. The momentum induced by the downwash of the chordwise vortices is already considered in the derivation of the scaling law, by regarding the momentum of the vortex loop.

# References

- AHLBORN, B., CHAPMAN, S., STAFFORD, R., BLAKE, R.W. & HARPER, D.G. (1997). Experimental simulation of the thrust phases of fast-start swimming of fish. *J. Exp. Biol.*, **200**, 2301–2312.
- AKAYDIN, H.D., ELVIN, N. & ANDREOPOULOS, Y. (2010). Energy harvesting from highly unsteady fluid flows using piezoelectric materials. *J. Intel. Mat. Syst. Str.*, **21**, 1263–1278.
- AKAYDIN, H.D., ELVIN, N. & ANDREOPOULOS, Y. (2012). Smart materials and structures. *J. Fluids Struct.*, **21**, 025007.
- ALBEN, S. & SHELLEY, M.J. (2008). Flapping states of a flag in an inviscid fluid: Bistability and the transition to chaos. *Phys. Rev. Lett.*, **100**, 074301.
- ALLEN, J.J. & SMITS, A.J. (2001). Energy harvesting eel. *J. Fluids Struct.*, **15**, 629–640.
- ANSARI, S.A., ŻBIKOWSKI, R. & KNOWLES, K. (2006a). Non-linear unsteady aerodynamic model for insect-like flapping wings in the hover. part 1: methodology and analysis. *J. Aerospace Eng.*, **220**, 61–83.
- ANSARI, S.A., ŻBIKOWSKI, R. & KNOWLES, K. (2006b). Non-linear unsteady aerodynamic model for insect-like flapping wings in the hover. part 2: implementation and validation. *J. Aerospace Eng.*, **220**, 169–186.

## REFERENCES

---

- ARGENTINA, M. & MAHADEVAN, L. (2005). Fluid-flow-induced flutter of a flag. *Proc. Natl Acad. Sci.*, **102**, 1829–1834.
- BAE, J., LEE, J., KIM, S., HA, J., LEE, B.S., PARK, Y., CHOONG, C., KIM, J.B., WANG, Z.L., KIM, H.Y., PARK, J.J. & CHUNG, U.I. (2014). Flutter-driven triboelectrification for harvesting wind energy. *Nat. Commun.*, **5**, 4929.
- BALINT, T.S. & LUCEY, A.D. (2005). Instability of a cantilevered flexible plate in viscous channel flow. *J. Fluids Struct.*, **20**, 893–912.
- BAO, C.Y., TANG, C., YIN, X.Z. & LU, X.Y. (2010). Flutter of finite-span flexible plates in uniform flow. *Chinese Phys. Lett.*, **27**, 064601.
- BERKOOZ, G., HOLMES, P. & LUMLEY, J.L. (1993). The proper orthogonal decomposition in the analysis of turbulent flows. *Annu. Rev. Fluid Mech.*, **25**, 539–575.
- BIRCH, J.M. & DICKINSON, M.H. (2003). The influence of wing-wake interactions on the production of aerodynamic forces in flapping flight. *J. Exp. Biol.*, **206**, 2257–2272.
- BOS, F.M., LENTINK, D., VAN OUDHEUSDEN, B.W. & BIJL, H. (2008). Influence of wing kinematics on aerodynamic performance in hovering insect flight. *J. Fluid Mech.*, **594**, 341–368.
- BOYER, F., POREZ, M., LEROYER, A. & VISONNEAU, M. (2008). Fast dynamics of an eel-like robot comparisons with navierstokes simulations. *IEEE Trans. Robot.*, **24**, 1274–1288.
- BUCHHOLZ, J.H.J. & SMITZ, A.J. (2006). On the evolution of the wake structure produced by a low-aspect-ratio pitching panel. *J. Fluid Mech.*, **546**, 433–443.

## REFERENCES

---

- BUCHHOLZ, J.H.J. & SMITZ, A.J. (2008). The wake structure and thrust performance of a rigid low-aspect-ratio pitching panel. *J. Fluid Mech.*, **603**, 331–365.
- BUCKINGHAM, E. (1914). On physically similar systems; illustrations of the use of dimensional equations. *Phys. Rev.*, **4**, 345–376.
- CHENG, G., LIN, Z.H., LIN, L., DU, Z. & WANG, Z.L. (2013). Pulsed nanogenerator with huge instantaneous output power density. *ACS Nano*, **7**, 7383–7391.
- CHOPRA, M.G. (1976). Large amplitude lunate-tail theory of fish locomotion. *J. Fluid Mech.*, **74**, 161–182.
- CHOPRA, M.G. & KAMBE, T. (1977). Hydromechanics of lunate-tail swimming propulsion. part 2. *J. Fluid Mech.*, **79**, 49–69.
- CONNELL, B.S.H. & YUE, D.K.P. (2007). Flapping dynamics of a flag in a uniform stream. *J. Fluid Mech.*, **581**, 33–67.
- DEVORIA, A.C. & RINGUETTE, M.J. (2012). Vortex formation and saturation for low-aspect-ratio rotating flat-plate fins. *Exp. Fluids*, **52**, 441–462.
- DICKINSON, M.H. (1996). Unsteady mechanisms of force generation in aquatic and aerial locomotion. *Amer. Zool.*, **36**, 537–554.
- DICKINSON, M.H., LEHMANN, F.O. & SANE, S.P. (1999). Wing rotation and the aerodynamic basis of insect flight. *Science*, **284**, 1954–1960.
- DOARÉ, O. & MICHELIN, S. (2011). Piezoelectric coupling in energy-harvesting fluttering flexible plates: linear stability analysis and conversion efficiency. *J. Fluids Struct.*, **27**, 1357–1375.

## REFERENCES

---

- DONG, H., MITTAL, R. & NAJJAR, F.M. (2006). Wake topology and hydrodynamic performance of low-aspect-ratio flapping foils. *J. Fluid Mech.*, **566**, 309–343.
- DRUCKER, E.G. & LAUDER, G.V. (1999). Locomotor forces on a swimming fish: three-dimensional vortex wake dynamics quantified using digital particle image velocimetry. *J. Exp. Biol.*, **202**, 2393–2412.
- ELLINGTON, C.P. (1984a). The aerodynamics of flapping animal flight. *Am. Zool.*, **24**, 95–105.
- ELLINGTON, C.P. (1984b). The aerodynamics of hovering insect flight. i. the quasi-steady analysis. *Phil. Trans. R. Soc. Lond. B*, **305**, 1–15.
- ELLINGTON, C.P. (1984c). The aerodynamics of hovering insect flight, ii: Morphological parameters. *Phil. Trans. R. Soc. B*, **305**, 17–40.
- ELLINGTON, C.P. (1984d). The aerodynamics of hovering insect flight, iii: Kinematics. *Phil. Trans. R. Soc. B*, **305**, 41–78.
- ELLINGTON, C.P., VAN DEN BERG, C., WILLMOTT, A.P. & THOMAS, A.L.R. (1996). Leading-edge vortices in insect flight. *Nature*, **384**, 626–630.
- ELOY, C., LAGRANGE, R., SOUILLIEZ, C. & SCHOUVEILER, L. (2008). Aeroelastic instability of a flexible plate in a uniform flow. *J. Fluid Mech.*, **611**, 97–106.
- ELOY, C., KOFMAN, N. & SCHOUVEILER, L. (2012). The origin of hysteresis in the flag instability. *J. Fluid Mech.*, **691**, 583–593.
- ENNOS, A.R. (1989). The kinematics and aerodynamics of the free flight of some diptera. *J. Exp. Biol.*, **142**, 49–85.

## REFERENCES

---

- FAN, F.R., LIN, L., ZHU, G., WU, W., ZHANG, R. & WANG, Z.L. (2012). Transparent triboelectric nanogenerators and self-powered pressure sensors based on micropatterned plastic films. *Nano Lett.*, **12**, 3109–3114.
- FARNELL, D.J.J., DAVID, T. & BARTON, D.C. (2004). Coupled states of flapping flags. *J. Fluids Struct.*, **19**, 29–36.
- FEI, F., MAI, J.D. & LI, W.J. (2012). A wind-flutter energy converter for powering wireless sensors. *Sensor. Actuat. A- Phys.*, **173**, 163–171.
- FLOREANO, D. & MATTIUSI, C. (2008). *Bio-inspired artificial intelligence: theories, methods, and technologies*. MIT press.
- FRY, S.N., SAYAMAN, R. & DICKINSON, M.H. (2005). The aerodynamics of hovering flight in drosophila. *J. Exp. Biol.*, **208**, 2303–2318.
- GAZZOLA, M., ARGENTINA, M. & MAHADEVAN, L. (2014). Scaling macroscopic aquatic locomotion. *Nature Phys.*, **10**, 758–761.
- GROTBERG, J.B. & JENSEN, O.E. (2004). Biofluid mechanics in flexible tubes. *Annu. Rev. Fluid Mech.*, **36**, 121–147.
- HUANG, L.X. (1995). Flutter of cantilevered plates in axial flow. *J. Fluids Struct.*, **9**, 127–147.
- HUANG, W.X. & SUNG, H.J. (2010). Three-dimensional simulation of a flapping flag in a uniform flow. *J. Fluid Mech.*, **653**, 301–336.
- JARDIN, T., DAVID, L. & FARCY, A. (2009). Characterization of vortical structures and loads based on time-resolved piv for asymmetric hovering flapping flight. *Exp. Fluids*, **46**, 847–857.
- JIA, L.B., LI, F., YIN, X.Z. & YIN, X.Y. (2007). Coupling modes between two flapping filaments. *J. Fluid Mech.*, **581**, 199–220.

## REFERENCES

---

- JONES, M.A. (2003). The separated flow of an inviscid fluid around a moving flat plate. *J. Fluid Mech.*, **496**, 405–441.
- KATZ, J. & PLOTKIN, A. (2001). *Low-Speed Aerodynamics, second ed.*. Cambridge University Press.
- KIM, D. (2010). *Characteristics of three-dimensional vortex formation and propulsive performance in flapping locomotion*. Doctoral dissertation, California Institute of Technology.
- KIM, D. & GHARIB, M. (2011). Characteristics of vortex formation and thrust performance in drag-based paddling propulsion. *J. Exp. Biol.*, **214**, 2283–2291.
- KIM, D., COSSÉ, J., HUERTAS CERDERIRA, C. & GHARIB, M. (2013). Flapping dynamics of an inverted flag. *J. Fluid Mech.*, **736**, R1.
- KIM, J. & CHUNG, W.K. (2006). Accurate and practical thruster modeling for underwater vehicles. *Ocean Eng.*, **33**, 566–586.
- KIM, S., HUANG, W.X. & SUNG, H.J. (2010). Constructive and destructive interaction modes between two tandem flexible flags in viscous flow. *J. Fluid Mech.*, **661**, 511–521.
- KIM, W., GILET, T. & BUSH, J.W. (2011). Optimal concentrations in nectar feeding. *Proc. Natl Acad. Sci. USA*, **108**, 16618–16621.
- KNIGHT, J. (2004). Urban wind power: Breezing into town. *Nature*, **430**, 12–13.
- KWEON, J. & CHOI, H. (2010). Sectional lift coefficient of a flapping wing in hovering motion. *Phys. Fluids*, **22**, 071703.
- LANG, T.G. (1966). *Hydrodynamic Analysis of Cetacean Performance in Whales, Dolphins and Porpoises*. Univ. California Press.

## REFERENCES

---

- LEE, J., PARK, Y.J., JEONG, U., CHO, K.J. & KIM, H.Y. (2013a). Wake and thrust of an angularly reciprocating plate. *J. Fluid Mech.*, **720**, 545–557.
- LEE, S., BAE, S.H., LIN, L., YANG, Y., PARK, C., KIM, S.W., CHA, S.N., KIM, H., PARK, Y.J. & WANG, Z.L. (2013b). Super-flexible nanogenerator for energy harvesting from gentle wind and as an active deformation sensor. *Adv. Funct. Mater.*, **23**, 2445–2449.
- LENTINK, D. & DICKINSON, M.H. (2009). Rotational accelerations stabilize leading edge vortices on revolving fly wings. *J. Exp. Biol.*, **212**, 2705–2719.
- LIGHTHILL, M.J. (1970). Aquatic animal propulsion of high hydromechanical efficiency. *J. Fluid Mech.*, **44**, 265–301.
- LIN, L., WANG, S., XIE, Y., JING, Q., NIU, S., HU, Y. & WANG, Z.L. (2013). Segmentally structured disk triboelectric nanogenerator for harvesting rotational mechanical energy. *Nano Lett.*, **13**, 2916–2923.
- LIU, F., CAI, J., ZHU, Y., TSAI, H.M. & WONG, A.S.F. (2001). Calculation of wing flutter by a coupled fluid-structure method. *J. Aircraft*, **38**, 334–342.
- LIU, H. & AONO, H. (2009). Size effects on insect hovering aerodynamics: an integrated computational study. *Bioinspir. Biomim.*, **4**, 015002.
- LIU, Y. & SUN, M. (2008). Wing kinematics measurement and aerodynamics of hovering droneflies. *J. Exp. Biol.*, **211**, 2014–2025.
- MCCARTY, L.S. & WHITESIDES, G.M. (2008). Electrostatic charging due to separation of ions at interfaces: contact electrification of ionic electrets. *Angew. Chem. Int. Edit.*, **47**, 2188–2207.

## REFERENCES

---

- MICHELIN, S. & DOARÉ, O. (2013). Energy harvesting efficiency of piezoelectric flags in axial flows. *J. Fluid Mech.*, **714**, 489–504.
- MICHELIN, S., LLEWELLYN SMITH, S.G. & GLOVER, B.J. (2008). Vortex shedding model of a flapping flag. *J. Fluid Mech.*, **617**, 1–10.
- MOTANI, R. (2002). Scaling effects in caudal fin propulsion and the speed of ichthyosaurs. *Nature*, **415**, 309–312.
- MOU, X.L., LIU, Y.P. & SUN, M. (2011). Wing motion measurement and aerodynamics of hovering true hoverflies. *J. Exp. Biol.*, **214**, 2832–2844.
- NEWMAN, J.N. (1977). *Marine Hydrodynamics*. MIT Press.
- NIU, S., LIU, Y., WANG, S., LIN, L., ZHOU, Y.S., HU, Y. & WANG, Z.L. (2013). Theory of sliding-mode triboelectric nanogenerators. *Adv. Mater.*, **25**, 6184–6193.
- PANG, Z., JIA, L.B. & YIN, X. (2001). Calculation of wing flutter by a coupled fluid-structure method. *J. Aircraft*, **22**, 121701.
- PARK, H. & CHOI, H. (2012). Kinematic control of aerodynamic forces on an inclined flapping wing with asymmetric strokes. *Bioinspir. Biomim.*, **7**, 016008.
- PARK, K., KIM, W. & KIM, H.Y. (2014). Optimal lamellar arrangement in fish gills. *Proc. Natl Acad. Sci. USA*, **111**, 8067–8070.
- PARK, Y.J., JEONG, U., LEE, J., KWON, S.R., KIM, H.Y. & CHO, K.J. (2012). Kinematic condition for maximizing the thrust of a robotic fish using a compliant caudal fin. *IEEE Trans. Robot.*, **28**, 1216–1227.
- PENG, J. & CHEN, S.G. (2012). Flow-oscillating structure interactions and the applications to propulsion and energy harvest. *Appl. Phys. Res.*, **4**, 1–14.

## REFERENCES

---

- PFEIFER, R., LUNGARELLA, M. & MAHADEVAN, F., IIDA (2007). Self-organization, embodiment, and biologically inspired robotics. *Science*, **318**, 1088–1093.
- POELMA, C., DICKSON, W.B. & DICKINSON, M.H. (2006). Time-resolved reconstruction of the full velocity field around a dynamically-scaled flapping wing. *Exp. Fluids*, **41**, 213–225.
- RAYLEIGH, L. (1878). On the instability of jets. *Proc. Lond. Math. Soc.*, **10**, 4–13.
- RISTROPH, L. & ZHANG, J. (2008). Anomalous hydrodynamic drafting of interacting flapping flags. *Phys. Rev. Lett.*, **101**, 194502.
- SANE, S.P. (2003). The aerodynamics of insect flight. *J. Exp. Biol.*, **206**, 4191–4208.
- SANE, S.P. & DICKINSON, M.H. (2002). The aerodynamic effects of wing rotation and a revised quasi-steady model of flapping flight. *J. Exp. Biol.*, **205**, 1087–1096.
- SCHOUVEILE, L. & ELOY, C. (2009). Coupled flutter of parallel plates. *Phys. Fluids*, **21**, 081703.
- SFAKIOTAKIS, M., LANE, D.M. & DAVIES, J.B.C. (1999). Review of fish swimming modes for aquatic locomotion. *J. Ocean. Eng.*, **24**, 237–252.
- SHELLEY, M., VANDENBERGHE, N. & ZHANG, J. (2005). Heavy flags undergo spontaneous oscillations in flowing water. *Phys. Rev. Lett.*, **94**, 094302.
- SHELLEY, M.J. & ZHANG, J. (2011). Flapping and bending bodies interacting with fluid flows. *Annu. Rev. Fluid Mech.*, **43**, 449–465.
- SONIN, A.A. (2004). A generalization of the  $\pi$ -theorem and dimensional analysis. *Proc. Nat. Acad. Sci. USA*, **101**, 8525–8526.

## REFERENCES

---

- SRYGLEY, R.B. & THOMAS, A.L.R. (2002). Unconventional lift-generating mechanisms in free-flying butterflies. *Nature*, **420**, 660–664.
- SWAINSON, W. (1839). *On the natural history and classification of fishes, amphibians and reptiles or monocardian animals*. Longman.
- TAIRA, K. & COLONIUS, T. (2009). Three-dimensional flows around low-aspect-ratio flat-plate wings at low reynolds numbers. *J. Fluid Mech.*, **623**, 187–207.
- TANEDA, S. (1968). Waving motions of flags. *J. Phys. Soc. Japan*, **24**, 392–401.
- TANG, D.M., YAMAMOTO, H. & DOWELL, E.H. (2003). Flutter and limit cycle oscillations of two-dimensional panels in three-dimensional axial flow. *J. Fluids Struct.*, **17**, 225–242.
- TANG, L. & PAÏDOUSSIS, M.P. (2007). On the instability and the post-critical behaviour of twodimensional cantilevered flexible plates in axial flow. *J. Sound Vib.*, **305**, 97–115.
- TANG, L. & PAÏDOUSSIS, M.P. (2008). The influence of the wake on the stability of cantilevered flexible plates in axial flow. *J. Sound Vib.*, **310**, 512–526.
- TANG, P.M.P., L. & JIANG, J. (2009). Cantilevered flexible plates in axial flow: energy transfer and the concept of flutter-mill. *J. Sound Vib.*, **326**, 263–276.
- TAYLOR, G.K., NUDDS, R.L. & THOMAS, A.L.R. (2003). Flying and swimming animals cruise at a strouhal number tuned for high power efficiency. *Nature*, **425**, 707–711.
- TECHET, A.H. (2008). Propulsive performance of biologically inspired flapping foils at high reynolds numbers. *J. Exp. Biol.*, **211**, 274–279.

## REFERENCES

---

- THEODORSEN, T. (1935). General theory of aerodynamic instability and the mechanism of flutter. *NACA Report*, **496**.
- TIAN, F.B., LUO, H., ZHU, L. & LU, X.Y. (2011). Coupling modes of three filaments in side-by-side arrangement. *Phys. Fluids*, **23**, 111903.
- TRABER, T. & KEMFERT, C. (2011). Gone with the wind? electricity market prices and incentives to invest in thermal power plants under increasing wind energy supply. *Energ. Econ.*, **33**, 249–256.
- VAN DEN BERG, C. & ELLINGTON, C.P. (1997). The three-dimensional leading-edge vortex of a ‘hovering’ model hawkmoth. *Phil. Trans. R. Soc. B*, **352**, 329–340.
- VIDELER, J.J., STAMHUIS, E.J. & POVEL, G.D.E. (2004). Leading-edge vortex lifts swifts. *Science*, **306**, 1960–1962.
- VIROT, E., AMANDOLESE, X. & HÉMON, P. (2013). Fluttering flags: an experimental study of fluid forces. *J. Fluids Struct.*, **43**, 385–401.
- WALKER, S.M., THOMAS, A.L.R. & TAYLOR, G.K. (2010). Deformable wing kinematics in free-flying hoverflies. *J. R. Soc. Interface*, **7**, 131–142.
- WANG, S., LIN, L. & WANG, Z.L. (2012a). Nanoscale triboelectric-effect-enabled energy conversion for sustainably powering portable electronics. *Nano Lett.*, **12**, 6339–6346.
- WANG, S., LIN, L., XIE, Y., JING, Q., NIU, S. & WANG, Z.L. (2012b). Sliding-triboelectric nanogenerators based on in-plane charge-separation mechanism. *Nano Lett.*, **13**, 2226–2233.
- WANG, Z.J. (2004). The role of drag in insect hovering. *J. Exp. Biol.*, **207**, 4147–4155.
- WANG, Z.J. (2008). Aerodynamic efficiency of flapping flight: analysis of a two-stroke model. *J. Exp. Biol.*, **211**, 234–238.

## REFERENCES

---

- WATANABE, Y., SUZUKI, S., SUGIHARA, M. & SUEOKA, Y. (2002). An experimental study of paper flutter. *J. Fluids Struct.*, **16**, 529–542.
- WEIS-FOGH, T. (1973). Quick estimates of flight fitness in hovering animals, including novel mechanisms for lift production. *J. Exp. Biol.*, **59**, 169–230.
- WILLIAMSON, C.H. (1996). Vortex dynamics in the cylinder wake. *Annu. Rev. Fluid Mech.*, **28**, 477–539.
- WILLMOTT, A.P. & ELLINGTON, C.P. (1997a). The mechanics of flight in the hawkmoth *manduca sexta*. i. kinematics of hovering and forward flight. *J. Exp. Biol.*, **200**, 2705–2722.
- WILLMOTT, A.P. & ELLINGTON, C.P. (1997b). The mechanics of flight in the hawkmoth *manduca sexta*. ii. aerodynamic consequences of kinematic and morphological variation. *J. Exp. Biol.*, **200**, 2723–2745.
- WU, J.Z., MA, H.Y. & ZHOU, M.D. (2006). *Vorticity and Vortex Dynamics*. Springer.
- WU, T.Y. (2006). A non-linear unsteady flexible wing theory. *Struct. Control. Health Monit.*, **13**, 553–560.
- WU, T.Y. (2007). A non-linear theory for a flexible unsteady wing. *J. Eng. Math.*, **58**, 279–287.
- XIE, Y., WANG, S., LIN, L., JING, Q., LIN, Z.H., NIU, S., WU, Z. & WANG, Z.L. (2013). Rotary triboelectric nanogenerator based on a hybridized mechanism for harvesting wind energy. *ACS Nano*, **7**, 7119–7125.
- YAMAGUCHI, N., SEKIGUCHI, T., YOKOTA, K. & TSUJIMOTO, Y. (2000a). Flutter limits and behaviors of a flexible thin sheet in high-speed flow: experimental results and predicted behaviors for low mass ratios. *ASME J. Fluids. Eng.*, **122**, 74–83.

## REFERENCES

---

- YAMAGUCHI, N., YOKOTA, K. & TSUJIMOTO, Y. (2000b). Flutter limits and behaviors of a flexible thin sheet in high-speed flow: analytical method for prediction of the sheet behavior. *ASME J. Fluids. Eng.*, **122**, 65–73.
- YANG, W., CHEN, J., ZHU, G., WEN, X., BAI, P., LIN, Y. & WANG, Z.L. (2013a). Harvesting vibration energy by a triple-cantilever based triboelectric nanogenerator. *Nano Res.*, **6**, 880–886.
- YANG, Y., ZHU, G., ZHANG, H., CHEN, J., ZHONG, X., LIN, Z.H., SU, Y., BAI, P., WEN, X. & WANG, Z.L. (2013b). Triboelectric nanogenerator for harvesting wind energy and as self-powered wind vector sensor system. *ACS Nano*, **7**, 9461–9468.
- YU, J., HU, Y., HUO, J. & WANG, L. (2009). Dolphin-like propulsive mechanism based on an adjustable scotch yoke. *Mech. Mach. Theory*, **44**, 603–614.
- ZDUNICH, P., BILYK, D., MACMASTER, M., LOEWEN, D., DELAURIER, J., KORNBLOH, R., LOW, T., STANFORD, S. & HOLEMAN, D. (2007). Development and testing of the mentor flapping-wing micro air vehicle. *J. Aircraft*, **44**, 1701–1711.
- ZHANG, J., CHILDRESS, S., LIBCHABER, A. & SHELLEY, M. (2000). Flexible filaments in a flowing soap film as a model for one-dimensional flags in a two-dimensional wind. *Nature*, **408**, 835–839.
- ZHANG, R., LIN, L., JING, Q., WU, W., ZHANG, Y., YAN, L., HAN, R.P.S. & WANG, Z.L. (2012). Nanogenerator as an active sensor for vortex capture and ambient wind-velocity detection. *Energ. Environ. Sci.*, **5**, 8528–8533.

## REFERENCES

---

- ZHANG, X.S., HAN, M.D., WANG, R.X., ZHU, F.Y., LI, Z.H., WANG, W. & ZHANG, H.X. (2013). Frequency-multiplication high-output triboelectric nanogenerator for sustainably powering biomedical microsystems. *Nano Lett.*, **13**, 1168–1172.
- ZHU, G., CHEN, J., LIU, Y., BAI, P., ZHOU, Y.S., JING, Q., PAN, C. & WANG, Z.L. (2013a). Linear-grating triboelectric generator based on sliding electrification. *Nano Lett.*, **13**, 2282–2289.
- ZHU, G., LIN, Z.H., JING, Q., BAI, P., PAN, C., YANG, Y., ZHOU, Y. & WANG, Z.L. (2013b). Toward large-scale energy harvesting by a nanoparticle-enhanced triboelectric nanogenerator. *Nano Lett.*, **13**, 847–853.
- ZHU, G., CHEN, J., ZHANG, T., JING, Q. & WANG, Z.L. (2014). Radial-arrayed rotary electrification for high performance triboelectric generator. *Nat. Commun.*, **5**, 3426.
- ZHU, L. & PESKIN, C.S. (2002). Simulation of a flapping flexible filament in a flowing soap film by the immersed boundary method. *J. Comput. Phys.*, **179**, 452–468.

# 국 문 초 록

## 펼럭이는 날개와 깃발의 유체역학: 스케일링 분석과 실험

서울대학교 대학원  
기계항공공학부  
이 정 수

### 요 약

본 연구에서는 수중 및 공중 생명체들의 대표적인 이동 메커니즘인 플레핑 날개의 운동과 평판 근처에서 펼럭거리는 깃발의 운동에 대한 유체역학적 분석을 수행하였다. 플레핑 날개의 운동으로 인해서 발생하는 보텍스 유동에 전달되는 운동량에 대한 모델링을 바탕으로 플레핑 날개에서 발생하는 힘을 예측하는 스케일링 법칙을 도출하였다. 또한 펼럭거리는 깃발과 평판의 마찰 대전 효과를 이용하여 바람의 에너지를 전기 에너지로 전환시키는 새로운 개념의 에너지 하베스팅 메커니즘을 개발하였다.

우선적으로 가장 단순한 형태의 플레핑 운동 모드로서 플레핑 날개가 단순 회전 왕복 운동만을 수행할 때 발생하는 와류 구조와 추력에 대한 분석을 수행하였다. 플레핑 날개 주위의 유동장을 가시화한 결과 반주기당 두 개의 보텍스 구조가 각각 플레핑 날개가 가속 및 감속을 할 때 형성된다는 것을 확인하였다. 이 관찰을 바탕으로

두 개의 보텍스 구조에 유도되는 운동량을 모델링하여 플레핑 날개에서 발생하는 추력을 예측하는 스케일링 법칙을 도출하였으며, 이를 다양한 조건에서의 실험을 통하여 검증하였다.

플레핑 날개의 회전 왕복 운동에 관련된 연구를 확장하여 작은 물고기들이 상대적으로 넓은 꼬리 지느러미 형상을 갖는 물리적 배경에 대한 고찰을 수행하였다. 이를 위해 플레핑 날개의 형상 및 종횡비를 다양하게 변화시켜가면서 추력 및 유동장 변화를 분석하였다. 그 결과 플레핑 날개에서 발생하는 추력은 플레핑 날개의 형상 변화에 관계없이 플레핑 날개 주위의 보텍스 구조에 유도되는 운동량을 고려한 스케일링 법칙을 통해 예측할 수 있다는 것을 확인하였다. 또한 플레핑 날개의 추력은 날개가 0.7의 종횡비를 지닐 때 최대화되는 반면 플레핑 날개의 효율은 날개의 종횡비가 증가할수록 계속적으로 향상되는 것을 확인하였다. 본 연구의 수학적 모델링과 자연계 물고기 꼬리지느러미의 종횡비를 관측한 결과를 종합하면, 작은 물고기들은 효율 측면에서의 불리함을 감수하고 추력 면에서 이점을 얻기 위하여 작은 종횡비를 선택하였다는 결론을 도출할 수 있다.

곤충 날개 앞전 보텍스의 세기와 날개 주변의 와류 구조에 유도된 운동량에 대한 모델링을 바탕으로 정지비행 시 곤충 날개의 플레핑 운동에서 발생하는 양력을 예측하는 스케일링 법칙을 도출하였다. 스케일링 법칙과 실제 정지비행을 수행하고 있는 33종 곤충에 대한 관측 결과를 비교하여 스케일링 법칙을 검증하였다. 그 결과 본 연구의 스케일링 법칙은 곤충 날개의 양력 형성의 물리적 원리를 성공적으로 반영하고 있다는 것을 확인할 수 있었다. 본 연구의 스일

링 법칙은 곤충 날개의 잔화 방향을 분석하는 생물학자들이나 플래핑 기반 공중 비행체를 설계하는 로봇공학자들에게 단순하면서도 매우 강력한 지침을 제공할 것이라 기대된다.

다음으로 깃발과 평판의 간격, 깃발의 규격 및 재질, 바람의 속도를 변화시켜가면서 평판 주위에서 펄럭이는 깃발의 동적 거동과 유체와 깃발간의 에너지 전달 과정에 대한 유체역학적 분석을 수행하였다. 깃발이 펄럭임을 시작하는 조건은 평판의 유무에 관계없이 큰 차이가 없는 반면, 깃발이 펄럭이기 시작하면 깃발과 평판의 접촉 없이도 평판의 영향으로 인한 깃발 거동의 비대칭성이 관측되었다. 유체로부터 깃발로의 에너지 전달은 깃발의 중심부에서 유체로부터 깃발로의 에너지 전달, 에너지 전달에서 방출로의 전환기, 깃발의 끝부분에서 유체로의 에너지 방출의 과정을 순차적으로 거치는 것으로 나타났다. 깃발과 평판의 접촉 모드는 단일 접촉, 이중 접촉, 접촉 후 전과, 무작위 접촉 모드로 구분될 수 있으며, 각각의 접촉 모드가 발현되는 조건이 깃발과 유체의 질량비와 무차원 속도의로 표현된 2차원 도식 상에 표현되었다. 추가적으로 깃발의 무차원 주파수와 스트로우홀 수에 대한 분석을 진행하였다. 깃발의 무차원 주파수는 단일 깃발의 거동과 유사하게 0.3에서 0.6 사이의 범위 안의 값을 갖는 경향성을 보였다. 반면 스트로우홀 수의 경우 무차원 속도가 증가함에 따라 플래핑 운동에서 최적 효율을 보이는 것으로 알려진 0.3의 값으로 수렴하였다. 이를 통해 평판 주위 깃발의 경우 바람의 세기가 증가함에 따라 자가 최적화되는 경향성이 있다는 것을 확인할 수 있었다.

평판 주위 깃발의 거동 특성에 대한 분석을 바탕으로 펄럭이는 깃

발과 평판의 마찰 대전을 이용한 신개념 에너지 하베스팅 메커니즘을 개발하였다. 본 연구에서는 세로 7.5 cm, 가로 5 cm 규격의 깃발이 풍속 15 m/s의 바람에 놓여져 있을 때, 순간 최대 출력 200 V, 60  $\mu$ A 의 전기 신호를 158 Hz 의 주파수로 생산하는 것을 확인하였다. 또한 100  $\mu$ F의 축전기를 245초의 시간 내에 충전하는 것을 확인하였으며, 이는 0.86 mW의 전력에 해당한다. 본 연구에서 개발한 에너지 하베스팅 시스템은 작은 전자 기기의 무선 충전을 위한 저용량 시스템으로 활용이 가능하다. 또한 병렬 구조를 이용한 대용량 발전 시스템으로의 확장도 가능하여 기존 터빈 기반 풍력 발전의 단점을 극복한 신개념 풍력 발전 시스템으로의 응용이 가능하다.

주요어 : 플라핑, 보텍스 유동, 깃발, 에너지 하베스팅

학 번 : 2009 - 23077